LUDWIG - MAXIMILIANS - UNIVERSITÄT MÜNCHEN

MASTER'S THESIS

Spin-1 bosons in two-dimensional optical lattices

Spin-1 Bosonen in zweidimensionalen optischen Gittern

Author:
Constantin GRIGO

Supervisor:
Prof. Dr. Lode POLLET

March 16, 2015

Abstract

In this thesis, we study bosons in a $F = 1$ hyperfine state trapped in a square optical lattice. Such a system can accurately be described by the spin-1 Bose-Hubbard model. We give a mean-field description of that model for both ferromagnetic and antiferromagnetic interactions at zero and finite temperature. As opposed to the spinless system, we find first order Mott insulator to superfluid transitions in certain parameter regimes.

Furthermore, we perform a Quantum Monte Carlo simulation of what we call the trilayer system, which can be viewed as an approximation to the full spin-1 Bose-Hubbard model, excluding off-diagonal spin flip terms. Our results show first order Mott to superfluid transitions over wide parameter ranges, which always come along with sudden transitions in spin space. Moreover we see that such spin transitions may be shifted to a considerably different quantum critical point compared to the insulator to superfluid transition by regulating the spin interaction strength. Finally, we compute the ground state phase boundaries of the first Mott lobe both for one specific ferromagnetic and antiferromagnetic interaction.

CONTENTS

1 Introduction **7**

2 Theory **9**

2.1 The Bose-Hubbard model 9

2.1.1 Optical lattices 9

2.1.2 The Bose-Hubbard Hamiltonian: Emergence from optical lattice potentials 11

2.1.3 Spin interaction term for spin-1 bosons 13

2.1.4 Phases of the spin-1 Bose-Hubbard model 15

2.2 Phase transitions 18

2.2.1 Classical phase transitions 18

2.2.2 Quantum phase transitions 19

2.2.3 Finite size scaling 23

2.3 Analytical predictions 25

2.3.1 Mott limit 26

2.3.2 Mean-field approach 28

2.4 Monte Carlo simulations 47

2.4.1 Simple sampling 48

2.4.2 Importance sampling 49

2.4.3 Markov chain Monte Carlo 49

2.4.4 Path integral Monte Carlo 54

2.4.5 The worm algorithm 58

2.5 Error estimation and autocorrelation time 74

2.5.1 Uncorrelated data 75

2.5.2 Correlated data 76

2.5.3 Binning analysis 77

3 Results **79**

3.1 The ferromagnetic case 81

3.1.1 Phase transitions 84

3.1.2 Phase diagram 86

3.2 The antiferromagnetic case 88

3.2.1 Phase transitions 91

3.2.2 Phase diagram 95

4 Conclusion and outlook **97**

4.1 Conclusion 97

4.2 Outlook: Worm algorithm with multiple worms 98

CHAPTER 1

INTRODUCTION

About twenty years ago, the experimental realization of Bose-Einstein condensates [1, 2] in ultracold atomic gases opened the door to numerous new quantum many-body experiments. For instance, the creation of optical lattice potentials [3] and its filling with a dilute gas of cold bosonic atoms [4] allowed the investigation of a quantum phase transition [5] from a Mott-insulating to a superfluid state [6] by modification of the inter-particle interaction strength via Feshbach resonances [7]. Such a system can in very good approximation be described by the Bose-Hubbard model [8]. To keep the cloud of atoms together experimentally, magnetic traps are often the method of choice. The Zeeman splitting of atomic energy levels due to the inhomogeneous external magnetic field then leads to an effective potential that is only capable to confine atoms in a single hyperfine state. That means that atoms of total angular momentum $\vec{F} = \vec{I} + \vec{L} + \vec{S}$, where $\vec{I}$ is the nuclear spin and $\vec{L}$ and $\vec{S}$ are the electronic orbital and spin angular momenta, are usually trapped in the so-called 'weak-field seeking' state, which is given by a frozen hyperfine state $|F, m_F\rangle$.

However, the invention of purely optical traps [9] allowed for experiments where the atomic spin state is a further degree of freedom. Without any external magnetic field, each ground state is $2F + 1$-fold degenerate in the magnetic quantum number $m_F = -F, \ldots, F$. Thus, the corresponding bosonic quantum field operator $\hat{\Psi}$ acquires an additional index, $\hat{\Psi}_{m_F}$ and the related mean field order parameter becomes a vector [10] where each entry is associated to a hyperfine state m_F. Furthermore, inter-particle interactions may now depend on the exact hyperfine states of the two scattering particles.

Using the alkaline atoms ^{23}Na and ^{87}Rb, which have a nuclear spin of $I = 3/2$ and

a single electron in an $s-$orbital, one can prepare atoms in a $F = 1$ state. Such atoms are referred to as 'spin-1 bosons' in the following and their behavior in optical lattice potentials is the topic of this work.

We start with a short introduction to optical lattice potentials and motivate the usage of the spin-1 Bose-Hubbard Hamiltonian to describe $F = 1$ bosons in such potentials in the first section. Just after giving an overview of the phases that the spin-1 Bose-Hubbard model exhibits, we show how critical points of second order quantum phase transitions can be obtained via finite-size scaling.

Next, we have a look at our model in the limit of strong interactions, where the Hamiltonian is diagonal and therefore trivially analytically solvable. We then provide a mean-field solution both for the full spin-1 Bose-Hubbard model and the so-called trilayer model, which can be seen as an approximation to the original system.

The next section gives a self-contained introduction to path-integral Monte Carlo simulations and the worm algorithm [11, 12], which is the algorithm we used for a Monte-Carlo study of the trilayer system. We close this section with a description of two new kinds of update schemes which were invented in the course of this thesis. We then present our Monte-Carlo results and terminate this work with a discussion of the obtained data. As an outline, we give a theoretical description of a further Monte Carlo scheme including two open worm configurations, which should solve the challenges we had to struggle with in our simulations and thus allows for an efficient simulation of the full spin-1 Bose-Hubbard model.

CHAPTER 2

THEORY

2.1 The Bose-Hubbard model

In the following section, we first give a short background to optical lattice potentials and then derive a Hamiltonian for bosonic atoms in such potentials, which in very good approximation is given by the Bose-Hubbard model. We then deduce an additional interaction term for spin-1 bosons and close the section with an overview of the phases a spin-1 Bose-Hubbard model exhibits.

2.1.1 Optical lattices

One can think of an optical lattice as an artificial crystal created by the electric field $\vec{E}(\vec{r}, t)$ of two counter-propagating laser beams [13]. Far off resonance, the laser light of frequency ω_L induces an atomic dipole moment $\vec{d}$ like [14]

$$\vec{d} = \alpha(\omega_L)\vec{E}, \tag{2.1}$$

where $\alpha(\omega_L)$ is the atomic polarizability. This leads to the AC-Stark effect, which is covered by the Hamiltonian

$$\hat{H}_{\text{int}} = -\vec{d} \cdot \vec{E}, \tag{2.2}$$

which can be treated perturbatively. A straightforward calculation gives the corresponding shift in energy $\Delta E(\vec{r})$ as

$$\Delta E(\vec{r}) = -\frac{1}{2}\alpha(\omega_L)\langle\vec{E}^2(\vec{r},t)\rangle_t, \tag{2.3}$$

where $\langle . \rangle_t$ indicates a time average over one oscillation of the electric field. Usually, one excited state $E_e = \hbar\omega_e$ is much closer to resonance than all the others. In that case, the atomic polarizability becomes inversely proportional to the laser detuning $\Delta = \omega_L - (\omega_e - \omega_g)$, with ω_g the ground state frequency. The energy shift (2.3) may be seen as an effective potential $V_{\text{opt}}(\vec{r}) = \Delta E(\vec{r})$, due to which atoms feel the force

$$\vec{F}_{\text{dipole}} = -\vec{\nabla}V_{\text{opt}}(\vec{r}). \tag{2.4}$$

Hence, red-detuned lasers with $\Delta < 0$ attract the atoms towards regions of high intensity $I(\vec{r},t) \propto \vec{E}^2(\vec{r},t)$, while blue-detuned lasers with $\Delta > 0$ pull the particles towards regions of low intensity [13].

The simplest case of a one-dimensional optical lattice is given by the superposition of the electric fields of two counterpropagating laser beams of same frequency linearly polarized in z-direction, which leads to the potential

$$V_{\text{opt}}(x) = -\frac{1}{2}\alpha(\omega_L)E_0\cos^2(k_x x), \tag{2.5}$$

where E_0 is the amplitude of the electric laser field and k_x the wave number of the laser beam in x-direction. This can directly be generalized to higher-dimensional cubic lattices.

At sufficiently low temperatures, inter-atomic interactions of spinless bosons are completely determined by s-wave scattering where the scattering length is given by

$$a = \frac{m}{4\pi\hbar^2}\int V(\vec{r})\mathrm{d}^3 r, \tag{2.6}$$

with the atomic mass m and the interaction potential $V(\vec{r})$ of particles separated by the distance $\vec{r}$. This potential can usually be approximated by the contact potential

$$V(\vec{r}) = g\delta^3(\vec{r}), \tag{2.7}$$

so we can write

$$g = \frac{4\pi\hbar^2 a}{m}. \tag{2.8}$$

In practice, the scattering length a and thus the interaction strength can relatively easy be tuned using Feshbach resonances, see e.g. [7, 15].

2.1.2 The Bose-Hubbard Hamiltonian: Emergence from optical lattice potentials

Bosonic atoms trapped by an external potential are described by the Hamiltonian [4]

$$\hat{H} = \int \mathrm{d}^3 r \hat{\Psi}^\dagger(\vec{r}) \left(-\frac{\hbar^2}{2m}\vec{\nabla}^2 + V_{\mathrm{ext}}(\vec{r}) + \frac{g}{2}\hat{\Psi}^\dagger(\vec{r})\hat{\Psi}(\vec{r}) - \mu \right) \hat{\Psi}(\vec{r}), \tag{2.9}$$

where $\hat{\Psi}^\dagger(\vec{r})$ and $\hat{\Psi}(\vec{r})$ are bosonic field creation and annihilation operators at point $\vec{r}$ that fulfill the usual canonical commutation relations

$$\begin{aligned} \left[\Psi(\vec{r}), \Psi^\dagger(\vec{r}')\right] &= \delta^3(\vec{r} - \vec{r}'), \\ [\Psi(\vec{r}), \Psi(\vec{r}')] &= \left[\Psi^\dagger(\vec{r}), \Psi^\dagger(\vec{r}')\right] = 0. \end{aligned} \tag{2.10}$$

Inter-atomic interactions are approximated by the contact potential (2.7), and the external potential $V_{\mathrm{ext}}(\vec{r})$ is given by $V_{\mathrm{ext}}(\vec{r}) = V_{\mathrm{opt}}(\vec{r}) + V_{\mathrm{trap}}(\vec{r})$, where $V_{\mathrm{opt}}(\vec{r})$ is the potential of optical lattice and $V_{\mathrm{trap}}(\vec{r})$ an additional potential used to trap the cloud of cold atoms in a confined region. The parameter μ is the chemical potential that fixes the mean total particle number $\langle \hat{N} \rangle$ in the grand canonical ensemble.

The field operators $\hat{\Psi}(\vec{r}), \hat{\Psi}^\dagger(\vec{r})$ may be expanded in the basis of single particle wave functions $\Phi_k(\vec{r})$ as

$$\begin{aligned} \hat{\Psi}(\vec{r}) &= \sum_k \Phi_k(\vec{r}) \hat{b}_k, \\ \hat{\Psi}^\dagger(\vec{r}) &= \sum_k \Phi_k^*(\vec{r}) \hat{b}_k^\dagger, \end{aligned} \tag{2.11}$$

where the index k runs over the complete set of single particle quantum numbers and the operators $\hat{b}_k^\dagger, \hat{b}_k$ create and annihilate a particle in the corresponding mode, respectively. It is well known that in a periodic potential, the single particle wave functions are Bloch waves $\Phi_{n\vec{q}}(\vec{r})$ with quasi-momentum $\vec{q}$ and band index n. As Bloch waves are only multiplied by a phase factor $e^{i\vec{q}\cdot\vec{R}}$ due to translation by a lattice vector $\vec{R}$, they extend over the whole lattice. This is rather unpractical, since we are looking for a description of particles hopping around discrete lattice sites $\vec{R}$. Hence,

we switch to the basis of Wannier functions, which is given by

$$w_n(\vec{r}) = \frac{1}{\sqrt{N_s}} \sum_{\vec{q}} e^{-i\vec{q}\cdot\vec{r}} \Phi_{n\vec{q}}(\vec{r}), \tag{2.12}$$

with N_s the total number of lattice sites. We now may rewrite the field operators as

$$\hat{\Psi}(\vec{r}) = \sum_{n,i} w_n(\vec{r} - \vec{R}_i)\hat{b}_{n,i}, \qquad \hat{\Psi}^\dagger(\vec{r}) = \sum_{n,i} w_n^*(\vec{r} - \vec{R}_i)\hat{b}_{n,i}^\dagger, \tag{2.13}$$

where the index i labels the lattice sites of the system. The Wannier functions $w_n(\vec{r} - \vec{R}_i)$ are well localized around the lattice site i and vanish quickly for increasing $\left|\vec{r} - \vec{R}_i\right|$.

For low temperatures, particles do not have enough energy to go to higher energy bands. We thus are confined to the lowest Bloch band and may drop the band index n for convenience.

The Hamiltonian (2.9) then becomes [13]

$$\hat{H} = -\sum_{i,j} t_{ij}\hat{b}_i^\dagger\hat{b}_j + \sum_{i,j,k,l} \frac{U_{ijkl}}{2}\hat{b}_i^\dagger\hat{b}_j^\dagger\hat{b}_k\hat{b}_l - \sum_{i,j} \mu_{ij}\hat{b}_i^\dagger\hat{b}_j, \tag{2.14}$$

with

$$t_{ij} = -\int \mathrm{d}^3 r w^*(\vec{r} - \vec{R}_i)\left(-\frac{\hbar^2}{2m}\vec{\nabla}^2 + V_{\mathrm{opt}}(\vec{r})\right) w(\vec{r} - \vec{R}_j), \tag{2.15}$$

$$U_{ijkl} = g\int \mathrm{d}^3 r w^*(\vec{r} - \vec{R}_i)w^*(\vec{r} - \vec{R}_j)w^*(\vec{r} - \vec{R}_k)w^*(\vec{r} - \vec{R}_l), \tag{2.16}$$

and

$$\mu_{ij} = \int \mathrm{d}^3 r w^*(\vec{r} - \vec{R}_i)\mu w(\vec{r} - \vec{R}_j). \tag{2.17}$$

In the kinetic term (2.15), the dominant contributions come from the diagonal elements t_{ii} and nearest neighboring sites $t_{\langle i,j\rangle}$. Next to nearest neighbor hopping is about two orders of magnitude smaller [16] and can be neglected. The diagonal elements t_{ii} lead to a constant shift in energy for each site and can therefore be dropped. Furthermore, we only consider isotropic hopping, where $t_{\langle i,j\rangle} = t$ for all sites. Since the Wannier functions are well localized, the relevant contribution to the on-site repulsion is $U_0 = U_{iiii}$. Nearest neighbor repulsion is one order of magnitude smaller [16] and is neglected, just like for the chemical potential, where we only consider $\mu = \mu_{ii}$.

With all these approximations, the Hamiltonian (2.9) may be rewritten as

$$\hat{H} = -t \sum_{\langle i,j \rangle} \hat{b}_i^\dagger \hat{b}_j + \frac{U_0}{2} \sum_i \hat{n}_i(\hat{n}_i - 1) - \mu \sum_i \hat{n}_i, \tag{2.18}$$

which is the famous Bose-Hubbard Hamiltonian, where $\hat{n}_i = \hat{b}_i^\dagger \hat{b}_i$ is the occupation number operator of particles on site i.

2.1.3 Spin interaction term for spin-1 bosons

As for spinful particles, the scattering length $a = a_S$ generally depends on the total hyperfine spin state S of the pair of interacting particles, we cannot use the interaction potential (2.7) anymore. Instead, the general contact potential of two spin F bosons has the form [10, 17, 18]

$$V(\vec{r}) = \delta^3(\vec{r}) \sum_{S=0,2...}^{2F} g_S \mathcal{P}_S, \tag{2.19}$$

where $g_S = \frac{4\pi\hbar^2 a_S}{m}$ and $\mathcal{P}_S$ is the projection operator on the total hyperfine spin state S. Using the operator identities

$$\sum_S \mathcal{P}_S = 1 \tag{2.20}$$

and

$$\vec{F}_1 \cdot \vec{F}_2 = \sum_S \lambda_S \mathcal{P}_S, \tag{2.21}$$

where $\lambda_S = \frac{1}{2}[S(S+1) - 2F(F+1)]$ and $\vec{F}$ in the case of spin-1 particles is the vector of spin-1 matrices,

$$F_x = \frac{1}{\sqrt{2}} \begin{pmatrix} 0 & 1 & 0 \\ 1 & 0 & 1 \\ 0 & 1 & 0 \end{pmatrix}, \quad F_y = \frac{1}{\sqrt{2}} \begin{pmatrix} 0 & -i & 0 \\ i & 0 & -i \\ 0 & i & 0 \end{pmatrix}, \quad F_z = \begin{pmatrix} 1 & 0 & 0 \\ 0 & 0 & 0 \\ 0 & 0 & -1 \end{pmatrix}, \tag{2.22}$$

we get

$$V(\vec{r}) = \left(c_0 + c_2 \vec{F}_1 \vec{F}_2\right) \delta^3(\vec{r}), \tag{2.23}$$

where $c_0 = (g_0 + 2g_2)/3$ and $c_2 = (g_2 - g_0)/3$. Hence, the inter-particle interaction term $\hat{H}_{\text{int}}$ of the Hamiltonian reads

$$\hat{H}_{\text{int}} = \int \mathrm{d}^3 r \left(\frac{c_0}{2} \hat{\Psi}^\dagger_m(\vec{r}) \hat{\Psi}^\dagger_j(\vec{r}) \hat{\Psi}_j(\vec{r}) \hat{\Psi}_m(\vec{r}) + \frac{c_2}{2} \hat{\Psi}^\dagger_m(\vec{r}) (F_\nu)_{mj} \hat{\Psi}_j(\vec{r}) \hat{\Psi}^\dagger_l(\vec{r}) (F_\nu)_{lk} \hat{\Psi}_k(\vec{r}) \right), \tag{2.24}$$

where summation over repeated indices is implicit and $\hat{\Psi}^\dagger_m(\vec{r}), \hat{\Psi}_m(\vec{r})$ are creation and annihilation operators for a boson in the Zeeman state $|F = 1, m_F = m = -1, 0, 1\rangle$. $(F_\nu)_{mj}$ denotes the $mj-$th component of the $\nu = x, y, z$ spin-1 matrix.

An analogous procedure as for scalar bosons leads to the Bose-Hubbard Hamiltonian for spin-1 particles [19]

$$\begin{aligned} \hat{H} = &- t \sum_{\langle i,j \rangle, \sigma} \left(\hat{b}^\dagger_{i,\sigma} \hat{b}_{j,\sigma} + \hat{b}^\dagger_{j,\sigma} \hat{b}_{i,\sigma} \right) + \frac{U_0}{2} \sum_i \hat{n}_i (\hat{n}_i - 1) \\ &- \mu \sum_i \hat{n}_i + \frac{U_2}{2} \sum_i \left(\vec{\hat{F}}^2_i - 2\hat{n}_i \right), \end{aligned} \tag{2.25}$$

where $\vec{\hat{F}}_i$ is the total spin operator at site i,

$$\vec{\hat{F}}_i = \sum_{\sigma, \sigma'} \hat{b}^\dagger_{i,\sigma} \vec{F}_{\sigma\sigma'} \hat{b}_{i,\sigma'}. \tag{2.26}$$

Making use of the spin-1 matrices given in (2.22), one can expand this as

$$\begin{aligned} \vec{\hat{F}}^2_i = &\hat{n}^2_{i,+} - 2\hat{n}_{i,+}\hat{n}_{i,-} + \hat{n}^2_{i,-} + \hat{n}_{i,+} + \hat{n}_{i,-} + 2\hat{n}_{i,0} + 2\hat{n}_{i,0}\hat{n}_{i,+} + 2\hat{n}_{i,0}\hat{n}_{i,-} \\ &+ 2\hat{b}^\dagger_{i,+}\hat{b}^\dagger_{i,-}\hat{b}_{i,0}\hat{b}_{i,0} + 2\hat{b}^\dagger_{i,0}\hat{b}^\dagger_{i,0}\hat{b}_{i,+}\hat{b}_{i,-}, \end{aligned} \tag{2.27}$$

where $\hat{n}_{i,\sigma} = \hat{b}^\dagger_{i,\sigma}\hat{b}_{i,\sigma}$ denotes the particle number operator of particles of magnetic quantum number $m_F = \sigma$ on site i.

2.1.3.1 The trilayer system

As our Monte-Carlo simulation is based on the so-called worm algorithm [11, 12] with a single mobile worm, it is not possible to simulate off-diagonal terms composed of more than one pair of creation and annihilation operators. In particular, the algorithm we use, see section 2.4.5), is not capable to simulate the spin-flip terms $\hat{b}^\dagger_{i,+}\hat{b}^\dagger_{i,-}\hat{b}_{i,0}\hat{b}_{i,0} + \hat{b}^\dagger_{i,0}\hat{b}^\dagger_{i,0}\hat{b}_{i,+}\hat{b}_{i,-}$ occuring in the $\vec{\hat{F}}^2_i$ term in (2.25). We thus ignored these terms in our QMC code and simulated what we henceforth call the *trilayer system*,

defined by the Hamiltonian

$$\hat{H} = -t \sum_{\langle i,j\rangle,\sigma} \left(\hat{b}^\dagger_{i,\sigma}\hat{b}_{j,\sigma} + \hat{b}^\dagger_{j,\sigma}\hat{b}_{i,\sigma}\right) + \frac{U_0}{2}\sum_i \hat{n}_i(\hat{n}_i - 1) - \mu\sum_i \hat{n}_i + \frac{U_2}{2}\sum_i \left(\underbrace{\hat{n}^2_{i+} - 2\hat{n}_{i+}\hat{n}_{i-} + \hat{n}^2_{i-} - \hat{n}_{i+} - \hat{n}_{i-} + 2\hat{n}_{i0}\hat{n}_{i+} + 2\hat{n}_{i0}\hat{n}_{i-}}_{=\vec{\hat{F}}^2_i - 2\hat{n}_i} \right). \tag{2.28}$$

Similarly, the algorithm is not able to sample several observables of the spin-1 Bose-Hubbard model such as the nematic order traceless tensor [19]

$$Q_{ab} = \langle \hat{F}_a \hat{F}_b \rangle - \frac{\delta_{ab}}{3}\langle \vec{\hat{F}}^2 \rangle, \tag{2.29}$$

the singlet density ρ_{sg} (see section 2.3.2.1), and the local magnetic moment given in (2.27). The reason for that is, in order to estimate the expectation value of terms like $\langle \hat{b}^\dagger_{i,\sigma_1}\hat{b}^\dagger_{i,\sigma_2}\hat{b}_{i,\sigma_3}\hat{b}_{i,\sigma_4}\rangle$ as they appear in these observables, we need to sample the corresponding Green function $G(i\sigma_1, i\sigma_2, i\sigma_3, i\sigma_4)$, which cannot be done by a single worm that propagates in only one spin layer σ (cf. section 2.4.5) at a time. Nevertheless, we give the theoretical framework of an algorithm with two simultaneously propagating worms in the outlook of this work in section 4.2, which is able to simulate the spin-flip terms and to sample the four-point Green's functions we need for the estimation of the observables mentioned above.

However, to keep track of changes in spin configuration, we can define what we call the *approximated local magnetic moment*

$$\vec{\hat{F}}^2_i = \hat{n}^2_{i+} - 2\hat{n}_{i+}\hat{n}_{i-} + \hat{n}^2_{i-} + \hat{n}_{i+} + \hat{n}_{i-} + 2\hat{n}_{i0} + 2\hat{n}_{i0}\hat{n}_{i+} + 2\hat{n}_{i0}\hat{n}_{i-}, \tag{2.30}$$

which is the same as the one given in equation (2.27), except for omission of the nondiagonal spin-flip terms. Confusion may arise because we are using the same symbol $\vec{\hat{F}}^2_i$ both in equations (2.27) and (2.30): the general rule is that in the Monte-Carlo part, we are talking about the quantity defined in the latter equation, whereas in the whole rest of this work (unless otherwise specified), we use the former definition of $\vec{\hat{F}}^2_i$.

2.1.4 Phases of the spin-1 Bose-Hubbard model

Firstly, let us consider the ordinary Bose-Hubbard model without spin-dependent interactions, given by the Hamiltonian (2.18). Depending on the ratio of the hopping parameter t relative to the on-site repulsion U_0, the Bose-Hubbard model exhibits two

distinct phases in the limit of zero temperature.

One of these phases is the *superfluid phase*, which is obtained in the limit of $t/U_0 \to \infty$. In that regime, the particles are fully delocalized and the many-body wave function of N atoms on a lattice of N_L sites is given by the product state [20]

$$|\Psi_{\mathrm{sf}}\rangle \propto \left(\sum_{i=1}^{N_L} \hat{b}_i^\dagger \right)^N |0\rangle \,. \tag{2.31}$$

Such a state has a long-range order phase coherence throughout the whole lattice, which is why it can be considered as superfluid.

The site occupation number n_i is Poisson distributed [15], so $\mathrm{Var}(n_i) = \langle \hat{n}_i \rangle$, which means that there are rather high particle number fluctuations on each lattice site. For increasing interactions U_0, these fluctuations become energetically more and more costly. In the limit strong interactions $t/U_0 \to 0$, the ground state of the system will be composed of localized wave functions with a fixed site occupation number, so that the interaction energy is minimized.

The emerging phase is a *Mott insulator*. The Mott insulator is characterized by a gapped energy spectrum and by a vanishing compressibility $\kappa = \frac{\partial \rho}{\partial \mu} = 0$. In the Mott limit $t/U_0 \to 0$, the ground state is given by the Fock state

$$|\Psi_{\mathrm{Mott}}\rangle \propto \left(\prod_{i=1}^{N_L} \hat{b}_i^\dagger \right)^\rho |0\rangle \,, \tag{2.32}$$

where ρ equals the constant particle density.

As opposed to $|\Psi_{\mathrm{Mott}}\rangle$, the superfluid state $|\Psi_{\mathrm{sf}}\rangle$ shows off-diagonal long-range order, which cannot vanish continuously in the thermodynamic limit [15]. Hence a sharp quantum phase transition has to occur at some critical value $\left(\frac{t}{U_0}\right)_c$ in the thermodynamic limit.

Both superfluid and Mott insulating phases also occur in the spin-1 Bose-Hubbard model. Moreover, the spin degree of freedom further enriches the phase diagram. For the antiferromagnetic case where $U_2 > 0$, it was first shown in [21] that in two and three dimensions the system exhibits *spin singlet* and *nematic* phases, see figure 2.1. A spin singlet phase can occur in Mott lobes with even particle density ρ. It is characterized by the formation of singlet pairs with vanishing total on-site spin $F = 0$. For a site with $n_i = 2$ particles, such a state reads

$$\left|\Psi_{\mathrm{singlet}}\right\rangle = \left|F_i = 0, m_{F,i} = 0, n_i = 2\right\rangle, \tag{2.33}$$

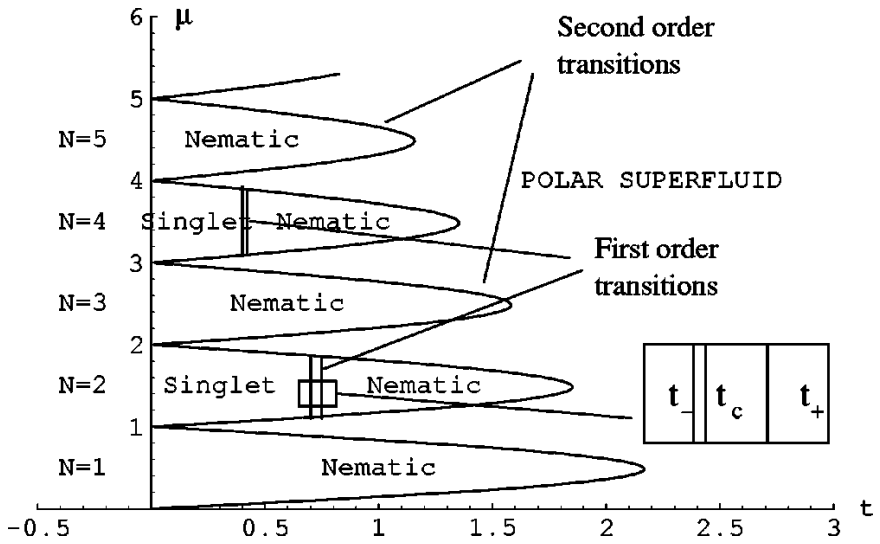

Figure 2.1: Schematic phase diagram for $F = 1$ bosons in two- and three-dimensional optical lattices with antiferromagnetic interaction $U_2 > 0$. In [19], first order transitions of spin singlet to nematic states are predicted for Mott lobes with even filling. In the picture, t_c marks the critical point of the spin transition, whereas t_- and t_+ limit the region of metastability. Picture taken from [19].

which can be written in spin occupation number basis as

$$\left|\Psi_{\text{singlet}}\right\rangle = \frac{1}{\sqrt{6}} \left(2\left|n_{i+}=1, n_{i0}=0, n_{i-}=1\right\rangle - \left|n_{i+}=0, n_{i0}=2, n_{i-}=0\right\rangle\right). \quad (2.34)$$

On the other hand, the nematic state is defined by the broken rotational $O(3)$ spin symmetry. So along with the local magnetic moment $\langle\vec{\hat{F}}^2\rangle$, the nematic order tensor $\mathbf{Q}$ given in equation (2.29) can be used as an order parameter for spin singlet to nematic transitions. In nematic phases, the diagonal elements of the nematic tensor Q_{aa} assume nonzero values, whereas they vanish in the spin singlet phase.

For ferromagnetic interactions $U_2 < 0$, Monte Carlo studies have shown [22] that the particles exhibit ferromagnetic order throughout the whole phase diagram, so that $\langle\vec{\hat{F}}_i^2\rangle = \langle\hat{n}_i(\hat{n}_i + 1)\rangle$.

As expected, also the trilayer system we simulated in this work shows the common Mott and superfluid phases. In the ferromagnetic regime, we also see the maximization of $\langle\vec{\hat{F}}_i^2\rangle$ throughout the whole phase diagram. However, we observe first order phase transitions in both the ferromagnetic and antiferromagnetic cases for various parameter regimes which do not occur in the full spin-1 model. Such transitions always go along with a change of spin configuration, see chapter 3.

2.2 Phase transitions

In this section, we explain the classification of phase transitions into first and second order and reveal the differences between classical, temperature driven phase transitions and quantum phase transitions. After that, we will see how general scaling properties at the quantum critical point can be used to determine phase boundaries in the thermodynamic limit via finite-size scaling.

2.2.1 Classical phase transitions

Generically, phase transitions are characterized by a sudden, discontinuous change in the properties of a physical system. Classical, temperature driven phase transitions can be classified to be either first or second order. This classification originally goes back to Ehrenfest [23] and uses the behavior of the derivatives of free energy $\mathcal{F}$ as the decision-making criterion.

If the first derivatives of $\mathcal{F}$ are discontinuous at the critical temperature T_c, the transition is named first order. First order transitions generally involve latent heat as well as phase coexistence at the transition temperature T_c [24], which incorporates local minima both for vanishing and non-vanishing order parameter in the free energy landscape [25].

For second order phase transitions, discontinuities occur in second or higher order derivatives of free energy $\mathcal{F}$. Usually, there exists an order parameter which is zero in one phase (the disordered phase), whereas it assumes a finite expectation value in the other (the ordered phase). Approaching the critical temperature T_c, the typical length scale, the equal-time correlation length ξ, diverges as

$$\xi \propto \varepsilon^{-\nu}, \tag{2.35}$$

where $\varepsilon = |T - T_c| / T$ is the reduced distance to the transition point T_c and ν is the correlation length critical exponent. Analogous to the correlation length ξ, the correlation time τ_c, which is the characteristic fluctuation decay time scale, diverges as

$$\tau_c \propto \varepsilon^{-\nu z} \propto \xi^z, \tag{2.36}$$

with the *dynamical critical exponent z*. Close to T_c, there are no other characteristic length and time scales as ξ and τ_c [26]. Hence, the physical properties must stay the same if we multiply all lengths in the system by a common factor a and simultaneously adjust all parameters such that the correlation length ξ stays constant. From

this we can infer the homogeneity condition of the singular part f_s of the free energy density close to a classical phase transition,

$$f_s(\varepsilon) = a^{-d} f_s(a^{1/\nu}\varepsilon). \tag{2.37}$$

This homogeneity relation gives rise to a set of simple power laws describing the behavior of physical quantities near criticality, see e.g. [27]. They generally are similar to equation (2.35) and have the form

$$Q \propto \varepsilon^{\zeta}, \tag{2.38}$$

where we call ζ the critical exponent of the quantity Q. Notably, one can classify second order phase transitions in so-called universality classes, in the sense that transitions of the same universality class share exact the same set of critical exponents.

2.2.2 Quantum phase transitions

So far we only considered classical phase transitions driven by thermal fluctuations. Let us see what happens if at low temperatures, the thermal energy $k_B T$ reaches the energy scale $\hbar\omega_c$ of quantum fluctuations near criticality. As we have seen in equation (2.36), the typical time scale τ_c diverges at the transition, hence the typical frequency ω_c and the corresponding energy scale $\hbar\omega_c$ vanish as

$$\hbar\omega_c \propto \varepsilon^{\nu z}. \tag{2.39}$$

Thus we can conclude that for finite temperatures,

$$\hbar\omega_c \ll k_B T_c, \tag{2.40}$$

so that any phase transition with critical temperature $T_c > 0$ can be considered as purely classical [24].

However, if phase transitions happen at zero temperature due to the variation of any control parameter r other than temperature, such as, for example, the chemical potential μ or the on-site repulsion U_0 in the Bose-Hubbard model, they are always driven by quantum fluctuations, hence the name *quantum phase transition* [5].

As will be described in section 2.4.4.1, we can map a d-dimensional quantum system to a $d+1$ dimensional classical one by the introduction of an imaginary time direction $\tau = \beta = 1/k_B T$. The homogeneity relation of the singular part of free

energy equation (2.37) then reads

$$f_s(\varepsilon) = a^{-(d+z)} f_s(a^{1/\nu}\varepsilon), \tag{2.41}$$

where z is again the dynamical critical exponent, describing the relative scaling of space and time dimensions. If we choose the scaling factor a to be $\varepsilon^{-1/\nu}$, we can infer that

$$f_s(\varepsilon) \propto \varepsilon^{\nu(d+z)}. \tag{2.42}$$

2.2.2.1 Critical behavior of the superfluid density ρ_{sf} and the compressibility κ

First of all, let us give a proper definition of the *superfluid density* ρ_{sf}. In a Bose-Einstein condensate (BEC) [28], a large number of particles N_0 are condensed in the ground state of the system. This justifies the application of the Bogoliubov approximation, which is the replacement of the ground state field operator $\hat{\Phi}_0(\vec{r}, t)$ by a complex number $\Phi_0(\vec{r}, t)$ (see e.g. [29]). The condensate particle density is then given by

$$n(\vec{r}, t) = \langle \hat{\Phi}_0^\dagger(\vec{r}, t)\hat{\Phi}_0(\vec{r}, t)\rangle = \left|\Phi_0(\vec{r}, t)\right|^2, \tag{2.43}$$

which has to fulfill the continuity equation

$$\frac{d}{dt} n(\vec{r}, t) = -\vec{\nabla} \cdot \vec{j}(\vec{r}, t) \tag{2.44}$$

with the particle current density

$$\vec{j}(\vec{r}, t) = -\frac{\hbar}{2m}\left(\Phi_0^*(\vec{r}, t)\vec{\nabla}\Phi_0(\vec{r}, t) - \Phi_0(\vec{r}, t)\vec{\nabla}\Phi_0^*(\vec{r}, t)\right). \tag{2.45}$$

Writing down the c-number field Φ_0 in terms of its amplitude and phase,

$$\Phi_0(\vec{r}, t) = \sqrt{n(\vec{r}, t)}e^{i\phi(\vec{r},t)}, \tag{2.46}$$

the particle current density may be rewritten as

$$\vec{j}(\vec{r}, t) = n(\vec{r}, t)\frac{\hbar}{m}\vec{\nabla}\phi(\vec{r}, t). \tag{2.47}$$

This suggests the definition of the *superfluid velocity* $\vec{v}_s$ as

$$\vec{v}_s = \frac{\hbar}{m}\vec{\nabla}\phi(\vec{r}, t), \tag{2.48}$$

whilst the increment Δf in free energy density due to the superfluid is given by the kinetic energy [30]

$$\Delta f = \frac{1}{2}\rho_{sf} v_s^2, \tag{2.49}$$

which is what we use as the defining equation for the superfluid density ρ_{sf}.

In a finite-size system, which is what we are always dealing with in Monte Carlo simulations, superfluidity is induced by picking up a twist $\Delta\phi$ of phase ϕ going one time around the system with linear size L [31], i.e.

$$\Phi_0(\ldots, x_j = 0, \ldots) = e^{i\Delta\phi}\Phi_0(\ldots, x_j = L, \ldots), \tag{2.50}$$

where x_j is the x-coordinate of the j-th particle. Such a twist implies that the average spatial derivative $\partial_x\phi$ assumes the value

$$\frac{\partial\phi}{\partial x} = \frac{\Delta\phi}{L}. \tag{2.51}$$

Using that together with the definition of the superfluid velocity v_s defined in equation (2.48), the shift in free energy density Δf in equation (2.49) becomes

$$\Delta f = \frac{1}{2}\rho_{sf}\left(\frac{\hbar}{m}\frac{\Delta\phi}{L}\right)^2. \tag{2.52}$$

We are now ready to deduce the scaling behavior of the superfluid density ρ_{sf}: from equation (2.42) we know that $f_s(\varepsilon) \propto \varepsilon^{\nu(d+z)}$. On the other hand, equation (2.52) implies that $\Delta f \propto \frac{\rho_{sf}}{L^2}$. As the diverging correlation length ξ is cut off by the linear system size L in a finite system, we can infer that

$$\rho_{sf} \;\propto\; L^2 \cdot \Delta f \;\propto\; \xi^2\varepsilon^{\nu(d+z)} \;\propto\; \varepsilon^{\nu(d+z-2)} \propto \xi^{2-d-z}, \tag{2.53}$$

where we made use of the scaling relation of the correlation length defined in equation (2.35). At the critical region $\varepsilon \to 0$, we can hence write

$$\rho_{sf} = \xi^{2-d-z} Y_{sf}(\xi/L, \xi^z/\beta), \tag{2.54}$$

with an appropriate scaling function Y_{sf}.

Next, we focus on the compressibility κ, defined by

$$\kappa = \frac{\partial \rho}{\partial \mu} = -\frac{\partial^2 f}{\partial \mu^2}, \tag{2.55}$$

with μ the chemical potential. We start with the fact that the action of the trilayer model (2.28) we are considering obeys the symmetry [8]

$$\mu \to \mu' = \mu + i\delta\mu, \tag{2.56a}$$
$$\Phi_0(\vec{r}, \tau) \to \Phi_0'(\vec{r}, \tau) = \Phi_0(\vec{r}, \tau) \exp\left(i\delta\mu/\hbar\right), \tag{2.56b}$$

where τ denotes imaginary time. Due to the periodic boundary conditions in imaginary time direction, we again get a phase twist similar to equation (2.50),

$$\Phi_0(\vec{r}, \tau = 0) = e^{i\Delta\phi}\Phi_0(\vec{r}, \tau = \beta\hbar). \tag{2.57}$$

Using the symmetry given in equations (2.56), this can be transformed to a shift in chemical potential μ,

$$\mu \to \mu' = \mu - i\Delta\phi/\beta. \tag{2.58}$$

With a Taylor expansion in μ, we can read off the corresponding shift in free energy density f,

$$\Delta f = \frac{\partial f}{\partial \mu}\left(-i\Delta\phi/\beta\right) + \frac{1}{2}\frac{\partial^2 f}{\partial \mu^2}\left(-i\Delta\phi/\beta\right)^2 + \dots \quad . \tag{2.59}$$

Hence, if we enforce a twist $\Delta\phi$ in the superfluid order parameter phase, we have to bring up the amount of energy Δf which in the limit $\beta, L \to \infty$ goes as

$$\Delta f \propto \kappa/\beta^2. \tag{2.60}$$

On the other hand, we found in equation (2.42) that $f_s \propto \varepsilon^{\nu(d+z)}$, so we can conclude that

$$\kappa \propto \xi^{2z}\varepsilon^{\nu(d+z)} \propto \varepsilon^{\nu(d-z)} \propto \xi^{z-d}, \tag{2.61}$$

which, with an appropriate scaling function Y_κ and under use of equation (2.35), can be written at criticality as

$$\kappa = \xi^{z-d} Y_\kappa(\xi/L, \xi^z/\beta), \tag{2.62}$$

which gives the proper scaling of κ of the generic Mott to superfluid phase transition in the case of *unfixed* total density ρ.

2.2.3 Finite size scaling

In Monte-Carlo simulations, we are always limited to the investigation of finite-size systems. As we will see later on in section 2.4.4.1, in the path integral formulation of the partition function Z, temperature comes in as a compact, additional imaginary time dimension of size $\beta\hbar$. Since the size of this dimension diverges for $T \to 0$, we are restricted to nonzero temperatures as well. However, as we have seen in the last section, quantum phase transitions only happen at $T = 0$ [26]. We thus need to have a framework that allows to draw conclusions from finite size and finite temperature simulations to phase transitions in the thermodynamic limit at zero temperature. Such a framework is given by *finite-size scaling*.

Since the correlation length ξ is equal to the linear system size L at the phase transition, we can rewrite the scaling equations (2.54) and (2.62) as

$$\rho_{sf} = L^{2-d-z} Y_{sf}(L^z/\beta), \tag{2.63}$$

$$\kappa = L^{z-d} Y_{\kappa}(L^z/\beta), \tag{2.64}$$

where we see here that, if we set $L^z/\beta = const.$ in our simulations, both $L^{d+z-2}\rho_{sf}$ and $L^{d-z}\kappa$ assume universal values at the critical point independent of system size. Hence, plotting these two quantities as a function of the control parameter that drives the quantum phase transition, the curves for different system sizes L should all intersect at the quantum phase transition critical point $\varepsilon = 0$.

In our system, we have to differentiate between two different cases: we can either cross the Mott to superfluid phase boundary varying μ which goes along with fluctuations in particle number, or we can keep the particle number N fixed at some integer filling, working in the canonical ensemble. In the latter case, we cross the phase boundary exactly at the tip of the Mott lobe by variation of the ratio of the particle hopping parameter t and the interaction strength U_0. The reduced distance to the critical point ε is then given by $\varepsilon = \frac{|\mu-\mu_c|}{\mu}$ and $\varepsilon = \frac{|t/U_0-(t/U_0)_c|}{t/U_0}$ for both cases, respectively.

The main difference of these two cases is that they belong to different universality classes, i.e. they generally have different critical exponents. Whilst the transition at integer filling is in the universality class of the $3D-XY$-model [8] with dynamical critical exponent $z = 1$, the generic transition with unfixed particle number has $z = 2$ [8].

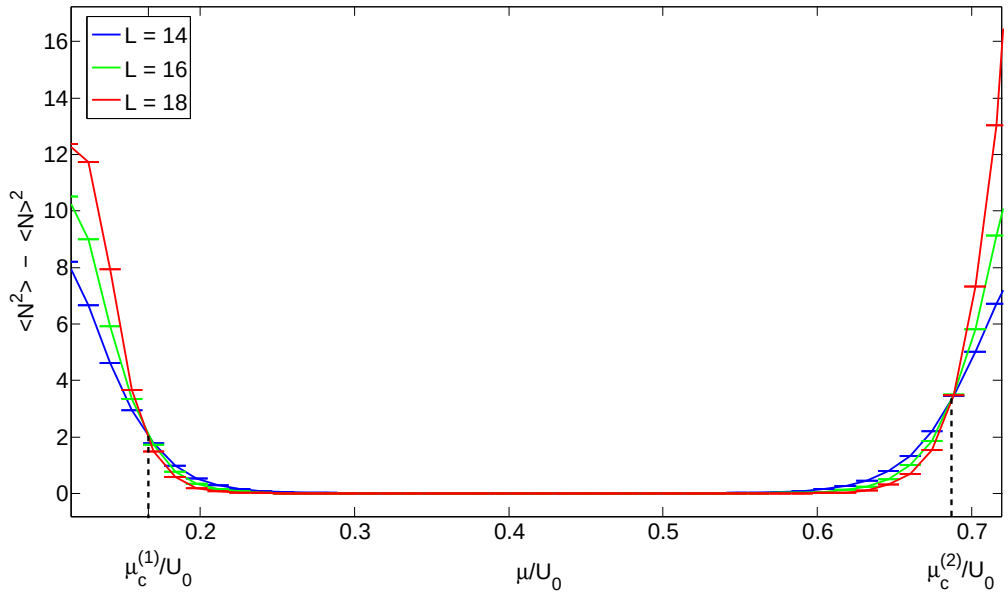

Figure 2.2: Finite-size scaling plot of particle number fluctuations $\langle N^2\rangle - \langle N\rangle^2$ versus chemical potential μ/U_0 for different system sizes. One can observe that all curves intersect in one point, namely at $\mu = \mu_c$. The used parameters were $U_0/t = 21$, $U_2 = 0.1U_0$. One can equivalently plot the expectation value of the winding number squared $\langle w^2\rangle$ and read off the critical point. However, particle number fluctuations have proved to be more precise.

We first consider the case of a generic phase transition in the grand canonical ensemble, varying the chemical potential μ while we fix the hopping parameter t to a constant value. The free energy density f is given by

$$f = -\frac{1}{L^d}\frac{1}{\beta}\log(Z) = -\frac{1}{L^d}\frac{1}{\beta}\log \mathrm{Tr}\left[e^{-\beta\hat{H}}\right]. \tag{2.65}$$

Differentiating two times with respect to μ yields the compressibility κ,

$$\begin{aligned}\kappa = -\frac{\partial^2 f}{\partial\mu^2} &= \frac{1}{L^d\beta}\left(\frac{\mathrm{Tr}\left[\hat{N}^2 e^{-\beta\hat{H}}\right]}{\mathrm{Tr}\left[e^{-\beta\hat{H}}\right]} - \frac{\mathrm{Tr}\left[\hat{N}e^{-\beta\hat{H}}\right]^2}{\mathrm{Tr}\left[e^{-\beta\hat{H}}\right]^2}\right)\\ &= \frac{1}{L^d\beta}\left(\langle\hat{N}^2\rangle - \langle\hat{N}\rangle^2\right),\end{aligned} \tag{2.66}$$

where $\hat{N}$ is the total particle number operator and $\langle . \rangle$ denotes the thermal expectation value in the grand canonical ensemble. As we have seen above, $L^{d-z}\kappa$ takes on a universal value at the critical point independent of system size if we keep $L^z/\beta =$

constant. Hence we can conclude that

$$\langle \hat{N}^2 \rangle - \langle \hat{N} \rangle^2 = const. \qquad \text{for} \quad \mu = \mu_c, \tag{2.67}$$

where with *const*. we mean independence of the linear lattice size L.

To find out the critical chemical potential μ_c of the Mott-to-superfluid quantum phase transition, we simply plot the particle number fluctuation $\langle \hat{N}^2 \rangle_T - \langle \hat{N} \rangle^2$ as a function of the chemical potential μ for different system sizes as shown in figure 2.2. There, we can easily read off μ_c as the common intersection point of all curves. However, system sizes may not be chosen too small: corrections to the scaling behavior increase with decreasing L [32]. Due to the complexity of these corrections, they can not be discussed here.

We can proceed in the same way for the superfluid density ρ_{sf}. From [33] we know that, for finite size systems with periodic boundary conditions, ρ_{sf} is connected to the number of paths w that wind around the system by

$$\rho_{sf} = \frac{\langle w^2 \rangle L^{2-d}}{2td\beta}. \tag{2.68}$$

The quantity w will become clear after we have introduced the path integral representation of the partition function Z in section 2.4.4.1. As shown above, $L^{d+z-2}\rho_{sf}$ does not depend on system size at criticality $\varepsilon = 0$. Hence we can deduce that

$$\langle w^2 \rangle = const. \qquad \text{for} \quad \varepsilon = 0, \tag{2.69}$$

where *const*. again means independence of linear system size L. This equation holds true for both the generic transition with $z = 2$ and $\varepsilon = \frac{|\mu - \mu_c|}{\mu}$ and the canonical transition at integer filling with $z = 1$ and $\varepsilon = \frac{|t/U_0 - (t/U_0)_c|}{t/U_0}$. However, at the generic transition, particle number fluctuations have proven to yield more precise results.

In contrast, for the transition with integer density, we work in the canonical ensemble where the compressibility κ is undefined. In that case, we are forced to use $\langle w^2 \rangle$ for the finite-size scaling analysis, see figure 2.3 for an example.

2.3 Analytical predictions

In the following section, we determine the phase boundaries of both the spin-1 Bose-Hubbard model and the trilayer model in the Mott limit, where the Hamiltonian of both systems is diagonal. Afterwards, we present an extensive mean-field analysis of both models, including the computation of ground state phase diagrams in the

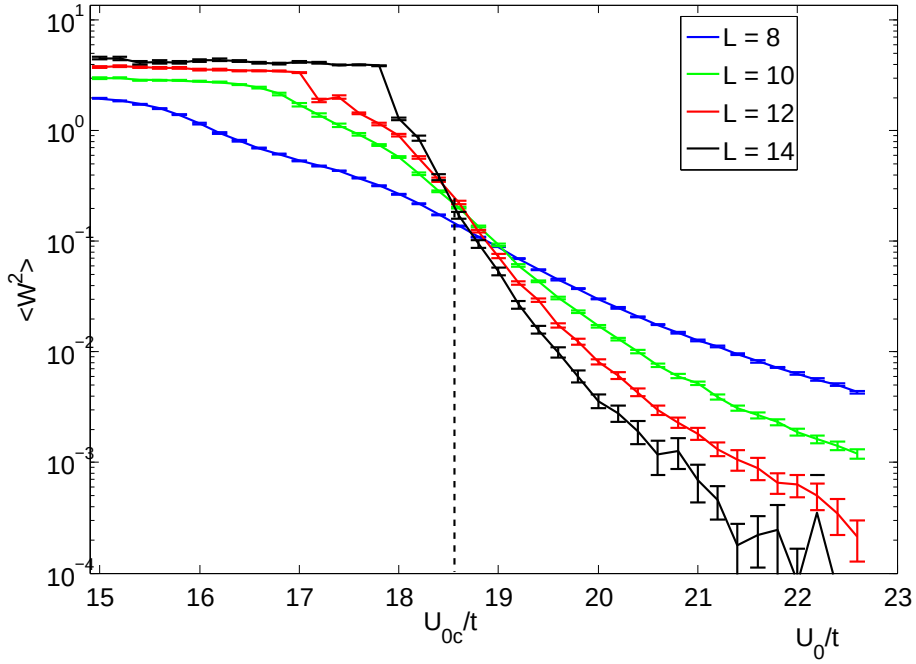

Figure 2.3: Finite size scaling plot of the square of the winding number $\langle w^2 \rangle$ against the on-site repulsion U_0/t for different system sizes for the tip of the second Mott lobe (note the log-scale). Again, all curves intersect in one point, namely at $U_0 = U_{0c}$. The spin interaction U_2 was set to $U_2 = 0.1U_0$ here. For the canonical transition at the tip of each lobe, we are forced to perform the finite size scaling with the winding number squared, $\langle w^2 \rangle$.

ferromagnetic as well as the in the antiferromagnetic regime.

2.3.1 Mott limit

A very easy way to cross-check the results of our Monte-Carlo simulation is to go to the Mott limit, i.e. $t/U_0 \to 0$. The spin-1 Bose-Hubbard Hamiltonian then reduces to

$$\hat{H}_S = \frac{U_0}{2} \sum_i \hat{n}_i(\hat{n}_i - 1) - \mu \sum_i \hat{n}_i + \frac{U_2}{2} \sum_i \left(\vec{\hat{F}}_i^2 - 2\hat{n}_i \right), \tag{2.70}$$

whereas the trilayer Hamiltonian becomes

$$\hat{H}_T = \frac{U_0}{2}\sum_i \hat{n}_i(\hat{n}_i - 1) - \mu\sum_i \hat{n}_i + \frac{U_2}{2}\sum_i \left(\hat{n}_{i+}^2 - 2\hat{n}_{i+}\hat{n}_{i-} + \hat{n}_{i-}^2 - \hat{n}_{i+} - \hat{n}_{i-} + 2\hat{n}_{i0}\hat{n}_{i+} + 2\hat{n}_{i0}\hat{n}_{i-}\right). \tag{2.71}$$

It is now trivial to predict the critical values μ_c of the transitions from the n-th to the $(n+1)$-th Mott lobe. As we can see, both Hamiltonians are diagonal in site occupation number basis and can be written as $\hat{H} = \sum_i \hat{h}_i$. Hence it suffices to find the ground state of the single-site Hamiltonian $\hat{h}_i$ and the corresponding ground state energy.

For the ferromagnetic case, $U_2 < 0$, the spin interaction term in $\hat{H}_S$ is minimized by maximizing the local magnetic moment $\langle\vec{\hat{F}}_i^2\rangle$, that is $\langle\vec{\hat{F}}_i^2\rangle = \langle\hat{n}_i(\hat{n}_i + 1)\rangle$. The single-site ground state energy is then simply given by

$$E_0^S = \frac{U_0 + U_2}{2} n\,(n-1) - \mu n, \tag{2.72}$$

where $n = \langle\hat{n}_i\rangle$ is the number of particles on each site. One can easily read off that the system is in a state with n particles per site if

$$(n-1)\,(U_0 + U_2) < \mu < n\,(U_0 + U_2)\,. \tag{2.73}$$

That means that, since $U_2 < 0$, the bases of the Mott lobes shrink with increasing $|U_2|$, and vanish completely for $|U_2| = U_0$.

The single-site spin energy of the trilayer system is obtained when the spin interaction term reads $\frac{U_2}{2}n(n-1)$, so that we get for the ground state energy again

$$E_0^T = \frac{U_0 + U_2}{2} n\,(n-1) - \mu n, \tag{2.74}$$

which means that for the n-th Mott lobe, the condition

$$(n-1)\,(U_0 + U_2) < \mu < n\,(U_0 + U_2) \tag{2.75}$$

must hold. Hence in the Mott limit, there are no differences between both systems.

In the antiferromagnetic case, $U_2 > 0$, the on-site energy in the full spin-1 system (2.70) is minimized by minimizing $\langle\vec{\hat{F}}_i^2\rangle$. Thus, the system is in a singlet state where $\langle\vec{\hat{F}}^2\rangle = F(F+1) = 0$ for states with even particle density $n = \textit{even}$ and in one of the $\langle\vec{\hat{F}}^2\rangle = F(F+1) = 2$ triplet states for odd particle densities $n = \textit{odd}$. Proceeding in

the same way as in the ferromagnetic case above, it is easy to show that

$$\begin{aligned} U_0\,(n-1) < \mu < U_0 n - 2U_2 \qquad & \text{for} \qquad n = odd, \\ U_0\,(n-1) - 2U_2 < \mu < nU_0 \qquad & \text{for} \qquad n = even, \end{aligned} \tag{2.76}$$

is required to be in a Mott state with n particles per site. Hence, the bases of the even Mott lobes grow at the expense of the odd ones by the amount of $2U_2$. This can be physically explained by the fact that the singlet state at even density is energetically favoured compared to the triplet state at $n = odd$.

For the trilayer system, the minimal spin interaction energy is given by $-\frac{U_2}{2}n$ for even and $\frac{U_2}{2}\,(1-n)$ for odd particle density n. From this, it follows that

$$\begin{aligned} U_0\,(n-1) < \mu < U_0 n - U_2 \qquad & \text{for} \qquad n = odd, \\ U_0\,(n-1) - U_2 < \mu < U_0 n \qquad & \text{for} \qquad n = even. \end{aligned} \tag{2.77}$$

Again, the bases of the even Mott lobes grow at the cost of the odd ones, but this time only by U_2. Thus, in the antiferromagnetic case, we observe differences in both systems already in the atomic limit, $t/U_0 \to 0$.

The Monte Carlo code we use has been checked in the described limit and it delivered the expected results.

2.3.2 Mean-field approach

In this section, we provide a mean-field approximation for both the full spin-1 Hamiltonian (2.25) and the trilayer system (2.28). In both cases, we use the decoupling approximation [34, 35]

$$\begin{aligned} \hat{b}^\dagger_{i\sigma}\hat{b}_{j\sigma} &= \left(\hat{b}^\dagger_{i\sigma} - \langle\hat{b}^\dagger_{i\sigma}\rangle\right)\left(\hat{b}_{j\sigma} - \langle\hat{b}_{j\sigma}\rangle\right) + \langle\hat{b}^\dagger_{i\sigma}\rangle\hat{b}_{j\sigma} + \hat{b}^\dagger_{i\sigma}\langle\hat{b}_{j\sigma}\rangle - \langle\hat{b}^\dagger_{i\sigma}\rangle\langle\hat{b}_{j\sigma}\rangle \\ &\approx \langle\hat{b}^\dagger_{i\sigma}\rangle\hat{b}_{j\sigma} + \hat{b}^\dagger_{i\sigma}\langle\hat{b}_{j\sigma}\rangle - \langle\hat{b}^\dagger_{i\sigma}\rangle\langle\hat{b}_{j\sigma}\rangle, \end{aligned} \tag{2.78}$$

where we neglect the first term because it is quadratic in fluctuations. We assume that the expectation value $\langle\hat{b}_{i,\sigma}\rangle$ is site independent and introduce the order parameter Ψ_σ for Bose-Einstein condensation in the σ component [36]

$$\Psi_\sigma = \langle\hat{b}_{i\sigma}\rangle = \langle\hat{b}^\dagger_{i\sigma}\rangle. \tag{2.79}$$

In equilibrium, one can see by minimization of free energy that the phases of the separate components differ by zero or π, which justifies to take the Ψ_σ's as real numbers

[36, 37].

We minimize the free energy $f(\Psi_\sigma)$ with respect to the order parameters Ψ_σ and call

$$\rho_c = \sum_\sigma \Psi_\sigma^2, \tag{2.80}$$

which is zero (nonzero) in the noncondensed (superfluid) phase.

Using the decoupling approximation (2.78), the full spin-1 Hamiltonian (2.25) as well as the trilayer Hamiltonian (2.28) can be written as the sum over a local mean field Hamiltonian $\hat{h}_i^{MF}$

$$\hat{H} = \sum_i \hat{h}_i^{MF}, \tag{2.81}$$

which allows us to minimize the free energy of each site i separately.

2.3.2.1 Full spin-1 system

The mean-field Hamiltonian $\hat{h}_S^{MF}$ of the full spin-1 system is given by

$$\begin{aligned}\hat{h}_S^{MF} =& \frac{U_0}{2}\hat{n}\left(\hat{n}-1\right) - \mu\hat{n} + \frac{U_2}{2}\left(\vec{\hat{F}}^2 - 2\hat{n}\right) \\ & - zt\sum_\sigma \left(\Psi_\sigma\left(\hat{b}_\sigma^\dagger + \hat{b}_\sigma\right) - \Psi_\sigma^2\right),\end{aligned} \tag{2.82}$$

where $z = 2d$ is the coordination number of the lattice and the site index i has been dropped for convenience. In the following, we work in the single-site Fock basis $\{|n_+, n_0, n_-\rangle\}$, where n_σ denotes the number of particles with spin σ. In order to have a finite-dimensional Hilbert space, a cutoff $n_{\max}$ in total particle number has to be introduced. The Hilbert space dimension then becomes

$$D_H = \frac{1}{12}\left(n_{\max}\left(n_{\max}+1\right)\left(2n_{\max}+1\right) + 9n_{\max}\left(n_{\max}+1\right) + 12\left(n_{\max}+1\right)\right). \tag{2.83}$$

We diagonalize the mean-field Hamiltonian $\hat{h}_S^{MF}$ numerically to get the eigenstates $|\phi_\alpha\rangle$ and their corresponding eigenenergies ε_α,

$$\hat{h}_S^{MF}(\Psi_\sigma)\,|\phi_\alpha(\Psi_\sigma)\rangle = \varepsilon_\alpha(\Psi_\sigma)\,|\phi_\alpha(\Psi_\sigma)\rangle\,, \tag{2.84}$$

where the eigenstates and -energies still depend on the order parameters Ψ_σ. Since we are also interested in finite temperature behavior, we not only confine ourselves to the search of the ground state energy E_0, but rather we minimize the free energy f

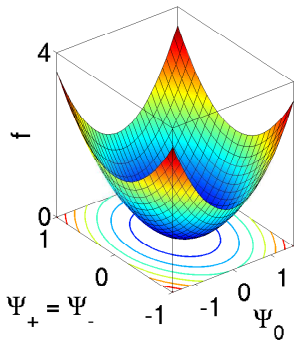

(a) Mott phase

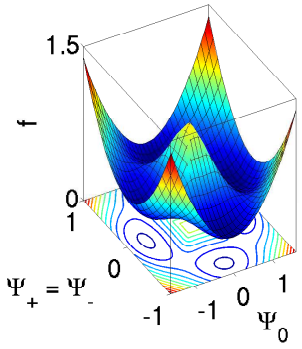

(b) Superfluid phase, $U_2 > 0$

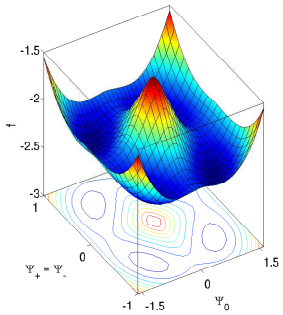

(c) Superfluid phase, $U_2 < 0$. Either Ψ_+ or Ψ_- is zero.

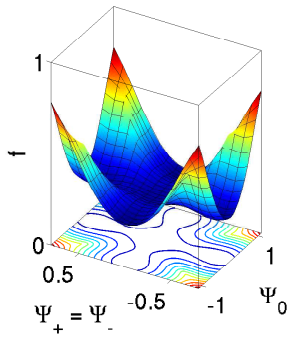

(d) Metastable state, $U_2 > 0$

Figure 2.4: Free energy f in dependence of the superfluid order parameters Ψ_σ. In the Mott phase 2.4a, there is only one minimum at $\Psi_\sigma = 0$. In the superfluid phases 2.4b and 2.4c, there are multiple local minima at $\Psi_\sigma \neq 0$ which are connected by the symmetries described in equations (2.86), (2.87). Figure 2.4d shows a metastable state at a first order boundary, where the minima at $\Psi_\sigma = 0$ and $\Psi_\sigma \neq 0$ are degenerate.

given by

$$f(\Psi_\sigma) = -\frac{1}{\beta} \log Z = -\frac{1}{\beta} \log \sum_\alpha e^{-\beta \varepsilon_\alpha(\Psi_\sigma)} \tag{2.85}$$

with respect to the order parameters Ψ_σ using the built-in Matlab optimization function based on the Nelder-Mead algorithm [38], a derivative-free multidimensional unconstrained minimization method. The minimization of free energy f allows us to compute thermal averages. However, care has to be taken here: the mean-field approximation (2.78) is only valid for small fluctuations, which goes along with a small hopping parameter t and low temperatures $\beta \to \infty$. Therefore, the mean-field approximation will only be valid for sufficiently large β.

For the case that the minimum of the free energy f occurs at nonzero order parameters $\Psi_\sigma \neq 0$, the ground states of the cases $U_2 < 0$ and $U_2 > 0$ possess different

symmetry: the antiferromagnetic case $U_2 > 0$ has the symmetry group $U(1) \times S^2$ [10], so we can write the order parameters as

$$\begin{pmatrix} \Psi_+ \\ \Psi_0 \\ \Psi_- \end{pmatrix} = \sqrt{\rho_c} e^{i\theta} \begin{pmatrix} -\frac{1}{\sqrt{2}} e^{-i\alpha} \sin\beta \\ \cos\beta \\ \frac{1}{\sqrt{2}} e^{i\alpha} \sin\beta \end{pmatrix}. \tag{2.86}$$

Likewise, the ferromagnetic case $U_2 < 0$ has the symmetry group $SO(3)$, so we can write

$$\begin{pmatrix} \Psi_+ \\ \Psi_0 \\ \Psi_- \end{pmatrix} = \sqrt{\rho_c} e^{i(\theta-\tau)} \begin{pmatrix} e^{-i\alpha} \cos^2\frac{\beta}{2} \\ \sqrt{2} \sin^2\frac{\beta}{2} \cos^2\frac{\beta}{2} \\ e^{i\alpha} \sin^2\frac{\beta}{2} \end{pmatrix}. \tag{2.87}$$

This means that the minima of free energy f in the condensed phase are connected by these symmetries. We are allowed to choose the order parameters to be real-valued [36, 37]. In figure 2.4, we see the free energy f plotted against the order parameters Ψ_σ for different phases, where we set $\Psi_+ = \Psi_-$. Figure 2.4d shows degenerate minima of f at $\Psi_\sigma = 0$ and $\Psi_\sigma \neq 0$. This is the case for coexisting Mott and superfluid phases at a first order boundary.

Computation of observables

Having all the mean-field eigenstates $|\phi_\alpha\rangle$ and eigenenergies ε_α at hand, it is not very difficult to compute thermal operator expectation values. The basic formula of an operator expectation value at finite temperature [39]

$$\langle \hat{O} \rangle = \frac{Tr\left[e^{-\beta \hat{h}_S^{MF}} \hat{O}\right]}{Tr\left[e^{-\beta \hat{h}_S^{MF}}\right]} \tag{2.88}$$

reduces in the eigenbasis of $\hat{h}_S^{MF}$ to

$$\langle \hat{O} \rangle = \frac{\sum_\alpha e^{-\beta\varepsilon_\alpha} \langle \phi_\alpha | \hat{O} | \phi_\alpha \rangle}{\sum_\alpha e^{-\beta\varepsilon_\alpha}}. \tag{2.89}$$

This allows us to compute the total density $n = \langle \hat{n} \rangle$, the local magnetic moment $\vec{F}^2 = \langle \vec{\hat{F}}^2 \rangle$ and the singlet density $n_{sg} = \langle \hat{n}_{sg} \rangle$. The total density operator $\hat{n}$ is simply given by

$$\hat{n} = \hat{b}_+^\dagger \hat{b}_+ + \hat{b}_0^\dagger \hat{b}_0 + \hat{b}_-^\dagger \hat{b}_- \tag{2.90}$$

and the operator of the local magnetic moment $\hat{\vec{F}}^2$ is [40]

$$\hat{\vec{F}}^2 = \sum_{\alpha,\beta,\gamma,\delta} \hat{b}^\dagger_\alpha \hat{b}^\dagger_\gamma \vec{F}_{\alpha\beta} \vec{F}_{\gamma\delta} \hat{b}_\delta \hat{b}_\beta, \tag{2.91}$$

where $\vec{F}$ is the vector of standard spin-1 matrices, see equation (2.22). This can be written out as

$$\hat{\vec{F}}^2 = \hat{n}_+^2 - 2\hat{n}_+\hat{n}_- + \hat{n}_-^2 + \hat{n}_+ + \hat{n}_- + 2\hat{n}_0 + 2\hat{n}_0\hat{n}_+ + 2\hat{n}_0\hat{n}_- + 2\hat{b}^\dagger_+\hat{b}^\dagger_-\hat{b}_0\hat{b}_0 + 2\hat{b}^\dagger_0\hat{b}^\dagger_0\hat{b}_+\hat{b}_-. \tag{2.92}$$

However, the singlet density operator $\hat{n}_{sg}$, giving the number of pairs of particles in a singlet state with $\hat{\vec{F}}^2 = 0$, is a bit more difficult to obtain. To derive it, we start with the singlet pair creation operator $\hat{A}^\dagger$ [41],

$$\hat{A}^\dagger = \frac{1}{\sqrt{6}} \left(\hat{b}^\dagger_0 \hat{b}^\dagger_0 - 2\hat{b}^\dagger_+ \hat{b}^\dagger_- \right), \tag{2.93}$$

which creates a singlet state as it is given in (2.34). Since the commutator

$$\left[\hat{A}, \hat{A}^\dagger \right] = \frac{2}{3}\hat{n} + 1, \tag{2.94}$$

does not in general equal 1, we may not simply take $\hat{n}_{sg} = \hat{A}^\dagger \hat{A}$ as the correct singlet density operator.

Instead, we define the states $\left| n_{nsg}, m, i \right\rangle$ by

$$\hat{n} \left| n_{nsg}, m, i \right\rangle = (n_{nsg} + 2m) \left| n_{nsg}, m, i \right\rangle, \tag{2.95}$$

$$\hat{A} \left| n_{nsg}, 0, i \right\rangle = 0, \tag{2.96}$$

$$\left(\hat{A}^\dagger \right)^m \left| n_{nsg}, 0, i \right\rangle = N \left| n_{nsg}, m, i \right\rangle, \tag{2.97}$$

$$\left\langle n'_{nsg}, m', i' \right| \left. n_{nsg}, m, i \right\rangle = \delta_{n'_{nsg}, n_{nsg}} \delta_{m',m} \delta_{i',i}, \tag{2.98}$$

where N is some normalization factor, n_{nsg} is the number of particles in a non-singlet state (i.e. $n_{nsg} = n - 2m$), the newly introduced quantum number m is the number of singlet pairs and i is just an auxiliary index to enumerate the states spanning the subspace $\left| n_{nsg}, m \right\rangle$ which is not generically one-dimensional. We see that the singlet density is given by $n_{sg} = \langle m \rangle$, which is what we are solving for in the following. Using equation (2.94) and

$$\left[\hat{n}, \hat{A}^\dagger \right] = 2\hat{A}^\dagger, \tag{2.99}$$

we find

$$\hat{A}^\dagger \hat{A} \left(\hat{A}^\dagger\right)^m = \left(-\frac{2}{3}m^2 + \frac{1}{3}\left(1 + 2\hat{n}\right)m\right)\left(\hat{A}^\dagger\right)^m + \left(\hat{A}^\dagger\right)^{m+1}\hat{A}. \tag{2.100}$$

Thus, applying $\hat{A}^\dagger\hat{A}$ on the state $\left|n_{nsg}, m, i\right\rangle = \frac{1}{N}\left(\hat{A}^\dagger\right)^m \left|n_{nsg}, 0, i\right\rangle$, we get

$$\begin{aligned}\hat{A}^\dagger\hat{A}\left|n_{nsg}, m, i\right\rangle &= \frac{1}{N}\hat{A}^\dagger\hat{A}\left(\hat{A}^\dagger\right)^m\left|n_{nsg}, 0, i\right\rangle = \\ &= \left(-\frac{2}{3}m^2 + \frac{1}{3}\left(1 + 2\hat{n}\right)m\right)\left|n_{nsg}, m, i\right\rangle\end{aligned} \tag{2.101}$$

and

$$\left\langle n_{nsg}, m, i\right|\hat{A}^\dagger\hat{A}\left|n_{nsg}, m, i\right\rangle = -\frac{2}{3}m^2 + \frac{1}{3}\left(1 + 2n\right)m. \tag{2.102}$$

Obviously, the states $\left|n_{nsg}, m, i\right\rangle$ are common eigenstates of the total number operator $\hat{n}$ and of the operator $\hat{A}^\dagger\hat{A}$. Because the eigenvalues of $\hat{A}^\dagger\hat{A}$ are given by the polynomial on the right hand side of equation (2.102), we solve for the true singlet density $n_{sg} = \langle m\rangle$ computing $\langle\hat{A}^\dagger\hat{A}\rangle$ in common eigenstates of $\hat{n}$ and $\hat{A}^\dagger\hat{A}$, i.e. in the basis given by $\left\{\left|n_{nsg}, m, i\right\rangle\right\}$.

To find these states, we start with the usual Fock basis where each state is written as (up to normalization)

$$|\Psi\rangle = \sum_{n_+, n_0, n_-} c_{n_+, n_0, n_-}\left|n_+, n_0, n_-\right\rangle,$$

where c_{n_+, n_0, n_-} are some complex coefficients. To get the states with vanishing singlet density $\left|n_{nsg}, m = 0, i\right\rangle$, the condition $\hat{A}\left|\Psi\right\rangle = 0$ has to be fulfilled,

$$\begin{aligned}\hat{A}\left|\Psi\right\rangle = \frac{1}{\sqrt{6}}\sum_{n_+, n_0, n_-} c_{n_+, n_0, n_-}\Big(&\sqrt{n_0\left(n_0 - 1\right)}\left|n_+, n_0 - 2, n_-\right\rangle \\ &-2\sqrt{n_+ n_-}\left|n_+ - 1, n_0, n_- - 1\right\rangle\Big) = 0,\end{aligned} \tag{2.103}$$

so the subspace $\left|n_{nsg} = \tilde{n}_{nsg}, m = 0\right\rangle$ is spanned by

$$\begin{aligned}\left|\tilde{n}_{nsg}, 0\right\rangle = \mathrm{span}\Bigg\{ N\sum_{n_+, n_0, n_-} c_{n_+, n_0, n_-}\left|n_+, n_0, n_-\right\rangle \;\Bigg|\; & c_{n_+, n_0, n_-} = K_{n_+, n_0, n_-} c_{n_+ + 1, n_0 - 2, n_- + 1} \\ \bigvee\ & \left(n_+ \vee n_- < 1 \wedge n_0 < 2\right),\ n_+ + n_0 + n_- = \tilde{n}_{nsg}\Bigg\},\end{aligned} \tag{2.104}$$

where N is again a normalization constant and K_{n_+,n_0,n_-} is given by

$$K_{n_+,n_0,n_-} = 2\sqrt{\frac{(n_+ + 1)(n_- + 1)}{n_0(n_0 - 1)}}. \tag{2.105}$$

From $\left|\tilde{n}_{nsg}, 0\right\rangle$ one can go to higher singlet density subspaces $\left|\tilde{n}_{nsg}, m\right\rangle$ simply by applying $\left(\hat{A}^\dagger\right)^m$ and a proper normalization of states. The basis of choice is now the one where the independent c_{n_+,n_0,n_-} are the coordinates.

As a simple example, we construct the basis states of the $n = 2$ subspace. The non-singlet basis states (the subspace $\left|\tilde{n}_{nsg} = 2, m = 0\right\rangle$) are given by (first condition in (2.104))

$$c_{0,2,0} = \sqrt{2}c_{1,0,1}, \tag{2.106}$$

$$N\left(c_{0,2,0}\left|0,2,0\right\rangle + c_{1,0,1}\left|1,0,1\right\rangle\right) = \sqrt{\frac{2}{3}}\left|0,2,0\right\rangle + \sqrt{\frac{1}{3}}\left|1,0,1\right\rangle, \tag{2.107}$$

and (second condition in (2.104))

$$n_+ < 1 \vee n_- < 1, n_0 < 2, n_+ + n_0 + n_- = 2, \tag{2.108}$$

$$\left|0,0,2\right\rangle, \left|0,1,1\right\rangle, \left|2,0,0\right\rangle, \left|1,1,0\right\rangle. \tag{2.109}$$

To get the basis states with a nonzero number of singlet pairs $m \neq 0$, we apply $\hat{A}^\dagger$ m-times on all non-singlet basis states that have a total particle number that is $2m$ below the particle number we are looking for. In the case of $n = 2$, we apply $\hat{A}^\dagger$ one time on the non-singlet state with $n = 0$ (which is trivially $|0,0,0\rangle$) and normalize. We get

$$\hat{A}^\dagger\left|0,0,0\right\rangle = \sqrt{\frac{1}{3}}\left|0,2,0\right\rangle - \sqrt{\frac{2}{3}}\left|1,0,1\right\rangle = \left|n_{nsg} = 0, m = 1\right\rangle. \tag{2.110}$$

In the described basis, the expectation value of the singlet density $n_{sg} = \langle m\rangle$ in a general state $|\Psi\rangle = \sum_{n_{nsg},m,i} c_{n_{nsg},m,i}\left|n_{nsg}, m, i\right\rangle$ is given by

$$n_{sg} = \langle m\rangle = \sum_{n_{nsg},m,i} m\left|c_{n_{nsg},m,i}\right|^2. \tag{2.111}$$

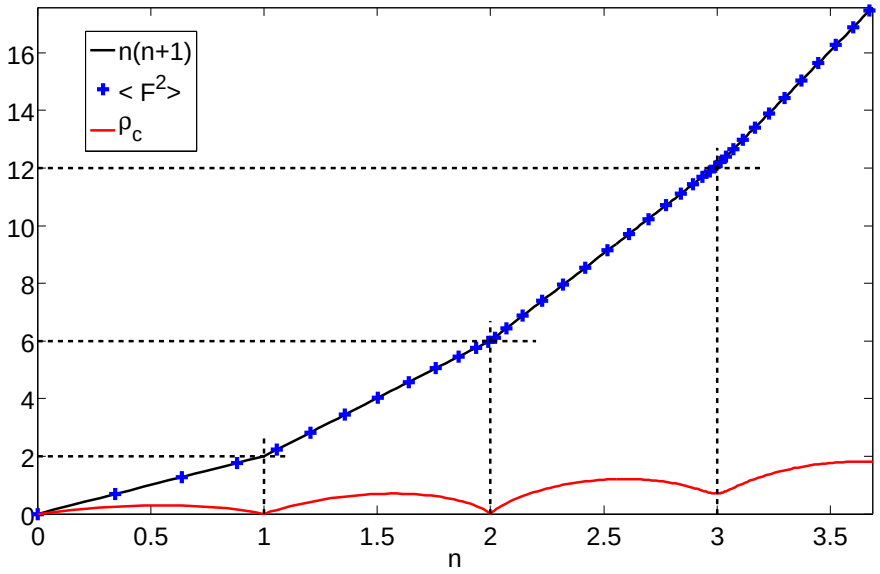

Figure 2.5: Magnetic moment $\langle\hat{\vec{F}}^2\rangle$, maximal value $n(n+1)$ and ρ_c plotted against the total particle density n. As one can see clearly, $\langle\hat{\vec{F}}^2\rangle$ coincides with its maximal possible value of $\langle\hat{\vec{F}}^2\rangle = n(n+1)$. Parameters where $T = 0, U_0/zt = 12.5, U_2 = -0.1U_0$.

The ferromagnetic case

In the ferromagnetic case, $U_2 < 0$, the energy is minimized by maximizing the local magnetic moment $\vec{F}^2$. $\vec{F}^2$ thus takes on its maximal possible value $n(n+1)$, as can be seen in figure 2.5. The system is ferromagnetic throughout the whole phase diagram [42].

The Mott to superfluid phase boundaries can be obtained perturbatively within our mean-field theory [35, 40, 43]. To this end, we split the Hamiltonian $\hat{h}_S^{MF}$ up into an unperturbed part $\hat{h}_S^{MF(0)}$ and a perturbation V as

$$\hat{h}_S^{MF} = \hat{h}_S^{MF(0)} + V, \tag{2.112}$$

with

$$\hat{h}_S^{MF(0)} = \frac{U_0}{2}\hat{n}(\hat{n}-1) - \mu\hat{n} + \frac{U_2}{2}\left(\hat{\vec{F}}^2 - 2\hat{n}\right) + zt\sum_\sigma \Psi_\sigma^2 \tag{2.113}$$

and

$$V = -zt\sum_\sigma \Psi_\sigma\left(\hat{b}_\sigma^\dagger + \hat{b}_\sigma\right). \tag{2.114}$$

As $\vec{\hat{F}}^2$, $\hat{F}_z$ and $\hat{n}$ commute, we work in the basis

$$\begin{aligned}
&\vec{\hat{F}}^2 \left|F, m_F, n\right\rangle = F(F+1) \left|F, m_F, n\right\rangle, \\
&\hat{F}_z \left|F, m_F, n\right\rangle = m_F \left|F, m_F, n\right\rangle, \\
&\hat{n} \left|F, m_F, n\right\rangle = n \left|F, m_F, n\right\rangle.
\end{aligned} \tag{2.115}$$

One can directly see that odd order terms in the perturbation expansion in V vanish. Second order corrections $E_g^{(2)}$ to the ground state energy E_g are given by the eigenvalues of the matrix [42, 44]

$$\begin{aligned}
M_{m_g, m_g'} &= \left\langle F_g = n_g, m_g, n_g \left| V \frac{1}{E_g^{(0)} - \hat{h}_S^{MF(0)}} V \right| F_g = n_g, m_g', n_g \right\rangle \\
&= \sum_l \frac{\left\langle n_g, m_g, n_g \left| V \right| l \right\rangle \left\langle l \left| V \right| n_g, m_g', n_g \right\rangle}{E_g^{(0)} - E_l^{(0)}},
\end{aligned} \tag{2.116}$$

since in the ferromagnetic case, the ground states $|g\rangle$ are $(2n_g + 1)$ - fold degenerate, $|g\rangle = \left|F = n_g, m_g = -F \ldots F, n_g\right\rangle$.

To compute the phase boundary of the first Mott lobe in the ferromagnetic case, we have to act with the perturbation V on the ground states $|1, -1 \ldots 1, 1\rangle$ with their unperturbed eigenenergy $E_g^{(0)} = -\mu + zt \sum_\sigma \Psi_\sigma^2$, which yields

$$\begin{aligned}
&V \left|1, 1, 1\right\rangle = \\
&- zt \left(\Psi_+ \left(\left|0, 0, 0\right\rangle + \sqrt{2} \left|2, 2, 2\right\rangle \right) + \Psi_0 \left|2, 1, 2\right\rangle + \Psi_- \left(\sqrt{\frac{1}{3}} \left|2, 0, 2\right\rangle - \sqrt{\frac{2}{3}} \left|0, 0, 2\right\rangle \right) \right), \\
&V \left|1, 0, 1\right\rangle = \\
&- zt \left(\Psi_+ \left|2, 1, 2\right\rangle + \Psi_0 \left(\left|0, 0, 0\right\rangle + 2 \sqrt{\frac{1}{3}} \left|2, 0, 2\right\rangle + \sqrt{\frac{2}{3}} \left|0, 0, 2\right\rangle \right) + \Psi_- \left|2, -1, 2\right\rangle \right), \\
&V \left|1, -1, 1\right\rangle = \\
&- zt \left(\Psi_- \left(\left|0, 0, 0\right\rangle + \sqrt{2} \left|2, -2, 2\right\rangle \right) + \Psi_0 \left|2, 1, 2\right\rangle + \Psi_+ \left(\sqrt{\frac{1}{3}} \left|2, 0, 2\right\rangle - \sqrt{\frac{2}{3}} \left|0, 0, 2\right\rangle \right) \right).
\end{aligned} \tag{2.117}$$

Thus, the relevant eigenstates $|l\rangle$ and their energies $E_l^{(0)}$ that couple to $|g\rangle$ by the per-

turbation V are

$$\begin{aligned}
&|l\rangle = \left|F_l, m_{F,l}, n_l\right\rangle = && E_l^{(0)} = \\
&|0,0,0\rangle && zt\sum_\sigma \Psi_\sigma^2, \\
&|2,-2,2\rangle, |2,-1,2\rangle, |2,0,2\rangle, \\
&|2,1,2\rangle, |2,2,2\rangle && U_0 - 2\mu + U_2 + zt\sum_\sigma \Psi_\sigma^2, \\
&|0,0,2\rangle && U_0 - 2\mu - 2U_2 + zt\sum_\sigma \Psi_\sigma^2.
\end{aligned} \tag{2.118}$$

Due to the symmetry (2.87), we are free to choose $\Psi_0 = \Psi_- = 0$, $\Psi_+ = \sqrt{\rho_c}$. The matrix $M_{m_g,m_g'}$ (2.116) then assumes the simple form

$$M_{m_g,m_g'} = z^2t^2 \begin{pmatrix} \frac{2\rho_c}{\mu-U_0-U_2} - \frac{\rho_c}{\mu} & & \\ & \frac{\rho_c}{\mu-U_0-U_2} & \\ & & \frac{\frac{1}{3}\rho_c}{\mu-U_0-U_2} + \frac{\frac{2}{3}\rho_c}{\mu-U_0+2U_2} \end{pmatrix}, \tag{2.119}$$

where we can easily read off the eigenvalues. It turns out that the smallest ground state energy up to second order is given by the very first entry of $M_{m_g,m_g'}$. The ground state energy can thus be written as

$$\begin{aligned}
E_g &= E_g^{(0)} + E_g^{(2)} + \ldots = \\
&= -\mu + \left(zt + \frac{2z^2t^2}{\mu - U_0 - U_2} - \frac{z^2t^2}{\mu}\right)\Psi_+^2 + \ldots = -\mu + A\Psi_+^2 + \ldots \quad .
\end{aligned} \tag{2.120}$$

According to Landau's theory of second order phase transitions, the ground state energy E_g is minimized within the order parameters Ψ_σ. For a positive coefficient $A > 0$, this is realized by $\Psi_+ = 0$. On the other hand, if $A < 0$, E_g is minimal for a finite value of Ψ_+. Hence, the Mott to superfluid phase boundary is given by the condition

$$A = zt + \frac{2z^2t^2}{\mu - U_0 - U_2} - \frac{z^2t^2}{\mu} = 0. \tag{2.121}$$

This condition leads to the phase boundary curve

$$\mu = \frac{1}{2}\left(U_0 + U_2 - zt \pm \sqrt{U_0^2 + 2U_0U_2 + U_2^2 - 6U_0zt - 6U_2zt + z^2t^2}\right). \tag{2.122}$$

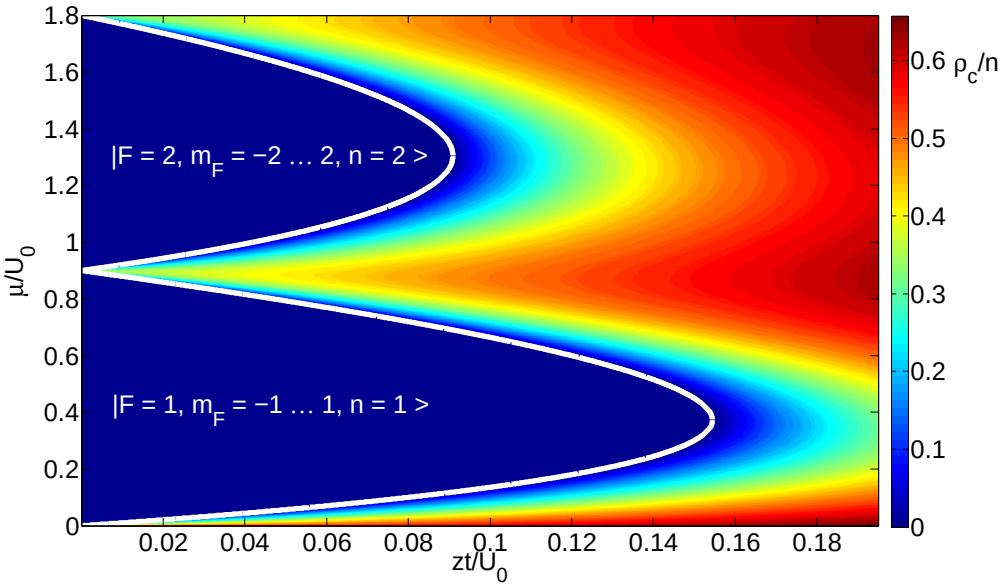

Figure 2.6: ρ_c/n as a function of zt/U_0 and μ/U_0 in the ferromagnetic case, $U_2 < 0$. One can clearly identify the familiar Mott lobes, circumscribed by the white line, which marks the Mott to superfluid phase boundary that is obtained perturbatively. As indicated, the first Mott lobe is in the threefold degenerate triplet state $\left|F = 1, m_f = -1 \ldots 1, n = 1\right\rangle$, whereas in the second Mott lobe, it is in the fivefold degenerate state $|F = 2, m_F = -2 \ldots 2, n = 2\rangle$, where the total magnetic moment F, its projection on the z-axis m_F and n are defined in equation (2.115). In the superfluid regime, the system is in general not an eigenstate of these operators anymore. Parameters where $T = 0$, $U_2 = -0.1U_0$.

An analogous reasoning for the $n = 2$ case leads to the phase boundary condition

$$\mu = \frac{1}{2}\left(3U_0 + 3U_2 - zt \pm \sqrt{(zt - 3(U_0 + U_2))^2 - 4(zt(U_0 + U_2) + 2(U_0 + U_2)^2)}\right). \tag{2.123}$$

However, to get the value of ρ_c as defined in equation (2.80) and the free energy f (2.85), we need to minimize f with respect to Ψ_σ numerically, as described above. Figure 2.6 shows the phase boundaries computed above as well as ρ_c obtained by numerical minimization of f.

Phase transitions

We numerically minimize the free energy f in dependence of the three order parameters Ψ_+, Ψ_0, Ψ_- to find superfluid ($\Psi_\sigma^{\min} \neq 0$) and Mott insulator or normal bose liquid

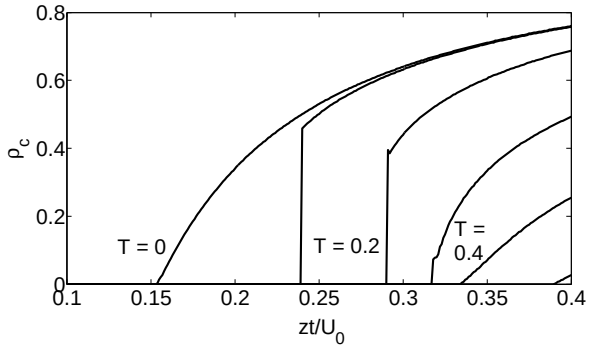

(a) $\langle\hat{n}\rangle = 1$, $T = 0$ (topmost curve) to $T = 0.5$ (lowermost curve) in steps of $\Delta T = 0.1$

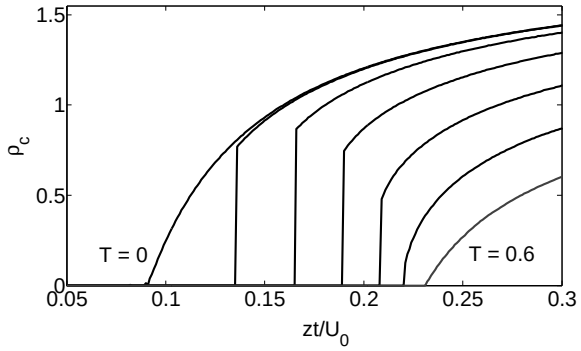

(b) $\langle\hat{n}\rangle = 2$, $T = 0$ (topmost curve) to $T = 0.6$ (lowermost curve) in steps of $\Delta T = 0.1$

Figure 2.7: ρ_c as a function of zt/U_0 for $\langle\hat{n}\rangle = 1$ 2.7a and $\langle\hat{n}\rangle = 2$ 2.7b, crossing the tips of the Mott lobes for $U_2 = -0.1U_0$. One can see that first order transitions happen for $0 < T \lesssim 0.3$ for $\langle\hat{n}\rangle = 1$ and $0 < T \lesssim 0.5$ for $\langle\hat{n}\rangle = 2$.

($\Psi_\sigma^{\min} = 0$) phases.

First, we cross the tips of the Mott lobes varying the on-site repulsion U_0 and tuning μ such that $\langle\hat{n}\rangle = n$. We can see in figure 2.7a, that for temperatures $0 < T \lesssim 0.3$, transitions crossing the tip of the first Mott lobe are of first order within our mean field theory, for the ferromagnetic case of $U_2 = -0.1U_0$. Similarly, crossing the tip of the second Mott lobe, transitions appear first order for $0 < T \lesssim 0.5$, see figure 2.7b.

Also for the generic transitions crossing the phase boundaries by changing μ, we observe first order transitions for finite temperatures, see figure 2.8. As the compressibility κ is always nonzero for $T > 0$, we see that there is, strictly speaking, no Mott insulating phase at finite temperatures. The phase where $\rho_c = 0, \kappa \neq 0$ can be seen as a normal bose liquid [37].

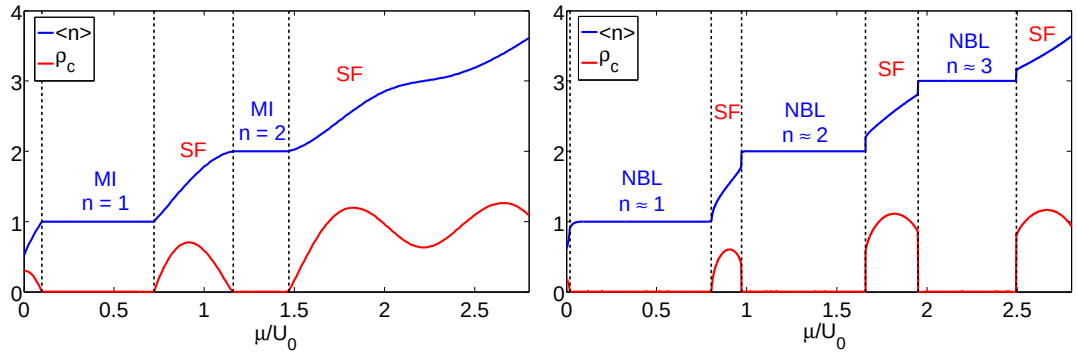

(a) T = 0 (b) T = 0.2

Figure 2.8: ρ_c and n versus the chemical potential μ/U_0 for fixed $zt/U_0 = 0.08$ and $U_2 = -0.1U_0$. At $T = 0$ 2.8a, transitions are continuous, whereas at $T = 0.2$ 2.8b, superfluid to normal bose liquid (NBL) transitions appear first order. We also see how superfluid phases shrink for the benefit of normal bose liquid phases for finite T: there is even a third plateau occuring for $2 \lesssim \frac{\mu}{U_0} \lesssim 2.5$.

The antiferromagnetic case

In the antiferromagnetic case, $U_2 > 0$, the energy is minimized by minimizing the local magnetic moment $\vec{F}^2$. Hence, the system is in a singlet state where $\langle \hat{\vec{F}}^2 \rangle = F(F+1) = 0$ for states with even particle density $\langle \hat{n} \rangle = even$ and in one of the $\langle \hat{\vec{F}}^2 \rangle = F(F+1) = 2$ triplet states for $\langle \hat{n} \rangle = odd$. For states with non-integer density, we find $0 < \langle \hat{\vec{F}}^2 \rangle < 2$.

The mean-field phase boundaries are again obtained perturbatively. Since for even Mott lobes the ground state is a unique singlet state $|g\rangle = \left|F_g = 0, m_{F,g} = 0, n_g = even\right\rangle$, but for odd lobes it is one of the threefold degenerate states $|g\rangle = \left|F_g = 1, m_{F,g} = -1 \ldots 1, n_g = odd\right\rangle$. Hence, both cases have to be treated separately, as was done in [40].

We begin with the easier case $n_g = 2$. Since the ground state $|g\rangle = |0, 0, 2\rangle$ is non-degenerate, we use the familiar formula of non-degenerate second order perturbation theory,

$$E_g^{(2)} = \sum_{|e\rangle \neq |g\rangle} \frac{|\langle g \,|\, V \,|\, e \rangle|^2}{E_g^{(0)} - E_e^{(0)}}. \tag{2.124}$$

Acting with the perturbation V on $|g\rangle$ yields

$$\begin{aligned} &V\,|0,0,2\rangle = \\ &-zt\left(\Psi_+\left(\sqrt{\frac{5}{3}}\,|1,1,3\rangle - \sqrt{\frac{2}{3}}\,|1,-1,1\rangle\right) + \Psi_0\left(\sqrt{\frac{2}{3}}\,|1,0,1\rangle + \sqrt{\frac{5}{3}}\,|1,0,3\rangle\right)\right. \\ &\left.+\Psi_-\left(\sqrt{\frac{5}{3}}\,|1,-1,3\rangle - \sqrt{\frac{2}{3}}\,|1,1,1\rangle\right)\right). \end{aligned} \tag{2.125}$$

The relevant states $|e\rangle$ and their corresponding energies $E_e^{(0)}$ that have nonvanishing matrix elements $\langle g\,|\,V\,|\,e\rangle$ are hence given by

$$\begin{aligned} |e\rangle = \left|F_e, m_{F,e}, n_e\right\rangle = \qquad & E_e^{(0)} = \\ |1,-1,1\rangle, |1,0,1\rangle, |1,1,1\rangle \qquad & -\mu + zt\sum_\sigma \Psi_\sigma^2, \\ |1,-1,3\rangle, |1,0,3\rangle, |1,1,3\rangle \qquad & 3U_0 - 3\mu - 2U_2 + zt\sum_\sigma \Psi_\sigma^2. \end{aligned} \tag{2.126}$$

The second order correction $E_g^{(2)}$ then becomes

$$E_g^{(2)} = z^2t^2\left(\frac{5/3}{\mu - 2U_0} + \frac{2/3}{-\mu + U_0 - 2U_2}\right)\sum_\sigma \Psi_\sigma^2. \tag{2.127}$$

Setting the coefficient of the second order term in the ground state energy E_g to zero

$$\frac{5/3}{\mu - 2U_0} + \frac{2/3}{-\mu + U_0 - 2U_2} + \frac{1}{zt} = 0, \tag{2.128}$$

leads to the phase boundary condition

$$\mu = \frac{3}{2}U_0 - U_2 - \frac{1}{2}zt \pm \frac{1}{6}\sqrt{9U_0^2 + 36U_0U_2 + 36U_2^2 - 42ztU_0 - 84ztU_2 + 9z^2t^2}. \tag{2.129}$$

Since the ground state of odd Mott lobes $|g\rangle = \left|F = 1, m_{F,g} = -1 \ldots 1, n_g\right\rangle$ is threefold degenerate, the perturbative computation of the phase boundaries is very cumbersome, but has been done in [40]. We thus only give the result here, which is given by

$$E_g = E_g^{(0)} + D(n,t,U_0,U_2,\mu)\rho_c + \ldots, \tag{2.130}$$

so the phase boundary condition is

$$D(n,t,U_0,U_2,\mu) = zt\,(1 - zt\,(\alpha + 4\beta + \gamma + 4\delta)) = 0, \tag{2.131}$$

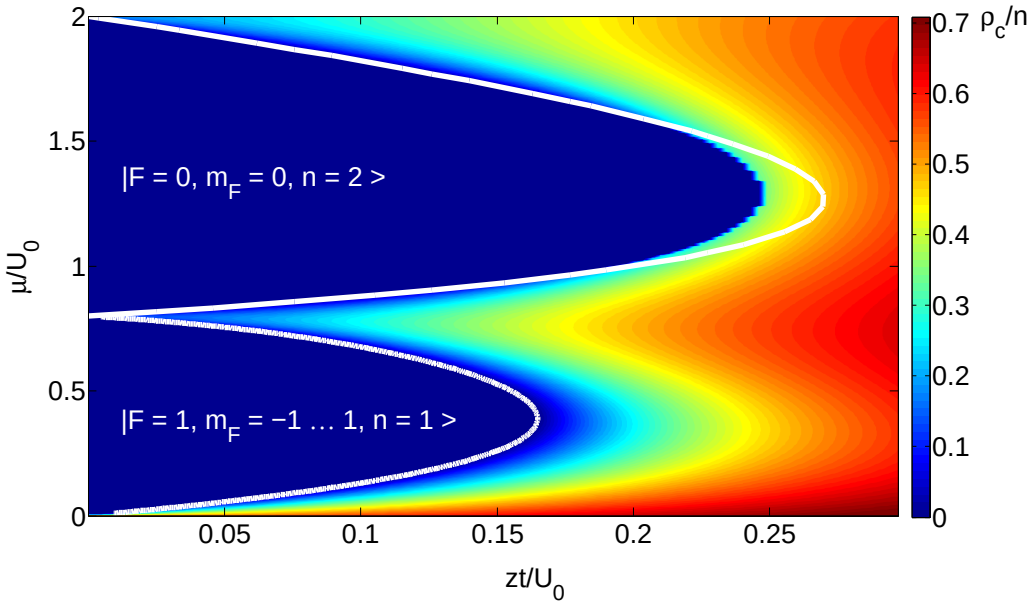

Figure 2.9: ρ_c/n as a function of zt/U_0 and μ/U_0 in the antiferromagnetic case, $U_2 > 0$. One can observe the well-known Mott lobes, bordered by the white lines that mark the Mott to superfluid phase boundary obtained by perturbation theory. We can see that the Landau theory of phase transitions used in the perturbative approach fails at the tip of the second Mott lobe: There, a first order phase transition occurs. As labeled, in the first Mott lobe, the system is in the threefold degenerate triplet state $|F = 1, m_F = -1 \ldots 1, n = 1\rangle$, whereas in the $n = 2$ lobe, it is in the unique $|F = 0, m_F = 0, n = 2\rangle$ singlet state, with F the total magnetic moment and m_F its projection onto the z-axis, see equations (2.115). For superfluid phases, the system is generally not in an eigenstate of $\hat{\vec{F}}^2$, $\hat{F}_z$ and $\hat{n}$ anymore. Parameters where $T = 0$, $U_2 = 0.1U_0$.

where [40]

$$\alpha = \frac{n+2}{3}\frac{1}{E^{(0)}(0,n-1) - E^{(0)}(1,n)} \qquad \beta = \frac{n-1}{15}\frac{1}{E^{(0)}(2,n-1) - E^{(0)}(1,n)}$$
$$\gamma = \frac{n+1}{3}\frac{1}{E^{(0)}(0,n+1) - E^{(0)}(1,n)} \qquad \delta = \frac{n+4}{15}\frac{1}{E^{(0)}(2,n+1) - E^{(0)}(1,n)}, \tag{2.132}$$

and $E^{(0)}(S,l)$ is the unperturbed energy of a state with $F = S$, $n = l$. The mean-field phase boundary for the first Mott lobe is thus given by the solution to the equation

$$1 - zt\left(\frac{1}{\mu} + \frac{2/3}{U_0 - \mu - 2U_2} + \frac{4/3}{U_0 - \mu + U_2}\right) = 0. \tag{2.133}$$

Again, as in the ferromagnetic case, we numerically minimize the free energy f

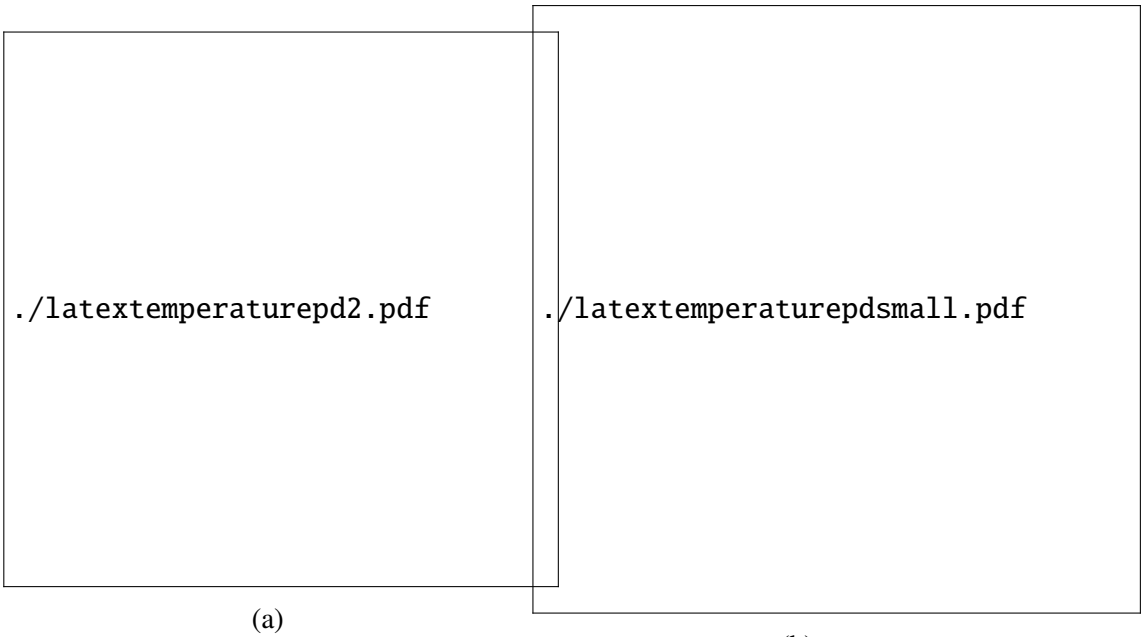

(a) (b)

Figure 2.10: Mean-field phase diagram in the $\mu/U_0 - T$ plane for the antiferromagnetic system at $U_0/zt = 12$, $U_2 = 0.1U_0$. We see how superfluid phases shrink with increasing temperature. The blue curves are lines of constant compressibility κ. Figure 2.10b is an enlarged version of the lower left corner of figure 2.10a. A metastable region, where superfluid and normal bose liquid phases coexist near a first order boundary, is encircled by the black line. A similar plot can be found in [37].

with respect to the order parameters Ψ_σ which allows to compute $\rho_c = \sum_\sigma \Psi_\sigma$. Figure 2.9 shows ρ_c and the phase boundaries of the first and second Mott lobe computed by perturbation theory for a antiferromagnetic system at $T = 0$, $U_2 = 0.1U_1$. One can nicely observe that the even Mott lobes grow at the cost of the odd ones due to the formation of singlet pairs. We can furthermore see that the perturbative solution fails around the tip of the second Mott lobe: in that region, first order phase transitions occur, which cannot be treated with Landau's theory of phase transitions.

Figure 2.10 shows a phase diagram in the μ/U_0 - T plane, where we see that superfluid phases shrink in favor of normal bose liquid phases with increasing temperature. The blue lines shown mark curves of constant compressibility κ. The area encircled with a black line marks a region where the free energy f has two distinct minima at $\Psi_\sigma = 0$ and $\Psi_\sigma \neq 0$. Hence, there occurs phase coexistence and the superfluid to normal bose liquid transition is of first order.

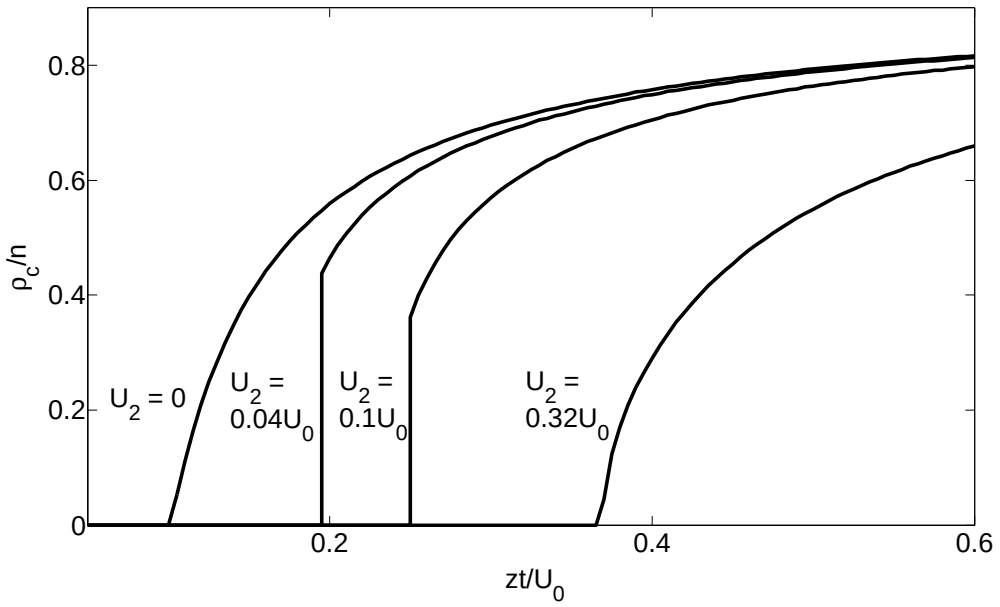

Figure 2.11: ρ_c/n as a function of $zt/U0$ for $n = 2$, i.e. crossing of the tip of the second Mott lobe at $T = 0$. The transition is of second order for $U_2 = 0$, but is of first order for $0 < U_2 \lesssim 0.32U_0$. For $U_2 \gtrsim 0.32U_0$, transitions are continuous again. The reason for the first order transition is the breakup of the singlet pair; the mean field ground state discontinuously changes to a state where $\langle \vec{\hat{F}}^2 \rangle \neq 0$.

Phase transitions

In the antiferromagnetic case, we again observe first order transitions at finite temperature, similar to the ones shown in figures 2.7 and 2.8b.

More interesting is the fact that at the tip of the second Mott lobe, first order phase transitions occur even at zero temperature, dependent on the strength of the spin interaction U_2. In figure 2.11, we see that at $T = 0$, crossing the Mott to superfluid phase boundary at $\langle \hat{n} \rangle = 2$ by the variation of the on site repulsion U_0 (i.e. crossing the tip of the second lobe), the transition is of second order for $U_2 = 0$, but is of first order for $0 < U_2 \lesssim 0.32U_0$, with a maximal jump in ρ_c at $U_2 \approx 0.04U_0$. For $U_2 \gtrsim 0.32U_0$, the transition is continuous again, which is in good accordance with the results obtained by a variational Gutzwiller mean-field approach in [45].

As already mentioned, in the antiferromagnetic case, the spin interaction energy is minimized by minimization of the local magnetic moment $\vec{F}^2$, given in equation (2.92). From this it follows that for Mott phases with even density n, all particles are paired in singlets, so $\langle \vec{\hat{F}}^2 \rangle = 0$ and the singlet pair density n_{sg} equals half the total

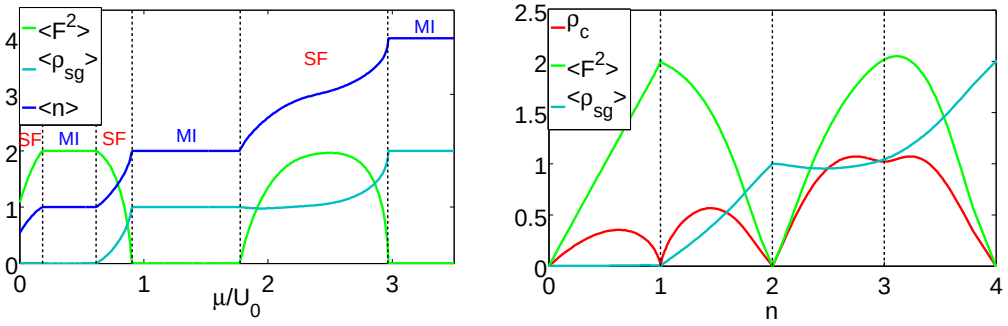

(a) (b)

Figure 2.12: Local magnetic moment $\langle\vec{\hat{F}}^2\rangle$ and the singlet density ρ_{sg} plotted against μ/U_0 (2.12a) and $\langle n\rangle$ (2.12b). We can see that the singlet density ρ_{sg} equals half of the total density n in even Mott lobes (note that there is no third Mott phase for the chosen U_0). The local magnetic moment $\vec{\hat{F}}^2$ vanishes in Mott phases with even density, whereas it is 2 in the odd ones.

density n, $n_{\mathrm{sg}} = n/2$, see figure 2.12a. However, in Mott phases with odd density, particles also form singlet pairs, but there is always one unpaired particle remaining, which leads to a $\langle\vec{\hat{F}}^2\rangle = F(F+1) = 2$ triplet state and the singlet density is $n_{\mathrm{sg}} = \frac{n-1}{2}$, see figure 2.12.

2.3.2.2 The trilayer system

For the trilayer system, the mean-field Hamiltonian $\hat{h}_T^{MF}$ reads

$$\begin{aligned}\hat{h}_T^{MF} =& \frac{U_0}{2}\hat{n}(\hat{n}-1) - \mu\hat{n} + \frac{U_2}{2}(\hat{n}_+^2 - 2\hat{n}_+\hat{n}_- + \hat{n}_-^2 - \hat{n}_+ - \hat{n}_- + 2\hat{n}_0\hat{n}_+ + 2\hat{n}_0\hat{n}_- \\ & - zt\sum_\sigma \left(\Psi_\sigma\left(\hat{b}_\sigma^\dagger + \hat{b}_\sigma\right) - \Psi_\sigma^2\right).\end{aligned} \tag{2.134}$$

As we only need the mean-field solution to the trilayer system to compare it with our Monte Carlo results in chapter 3, we focus on the production of the corresponding phase diagram here.

Unfortunately, in the ferromagnetic regime $U_2 < 0$, the unperturbed ground states are degenerate again, so the second order energy corrections are given by the eigenvalues of the appropriate Matrix M analogous to equation (2.116). Since we did not manage to bring these eigenvalues in a suitable form which is compact enough to be presented here, we are not able to give the corresponding phase boundary in an analytical way. Nevertheless, we can still minimize the free energy f with respect to the order parameters Ψ_σ as above, which allows us to determine the phase boundaries

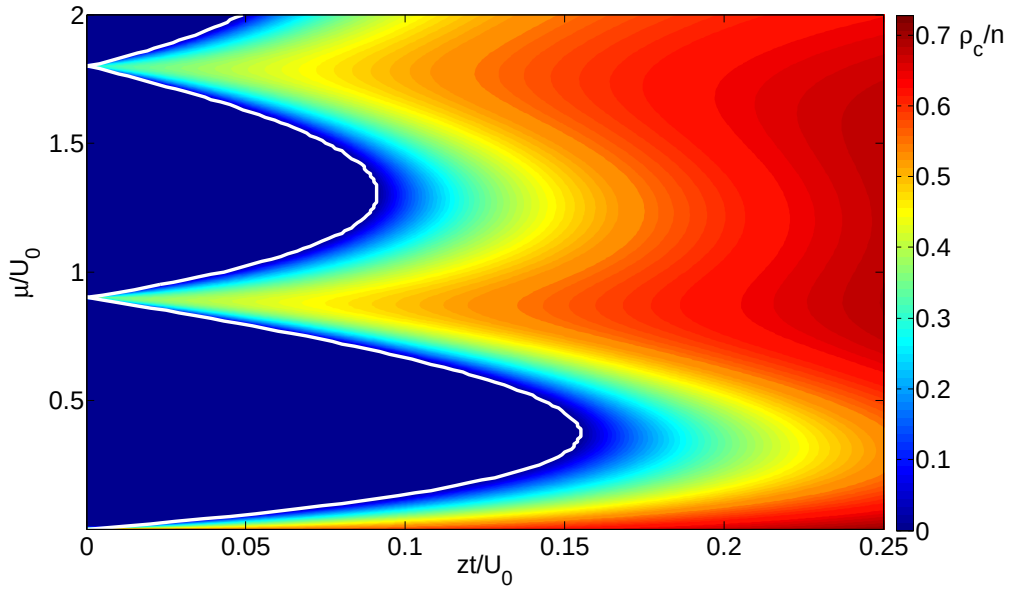

Figure 2.13: ρ_c/n as a function of zt/U_0 and μ/U_0 in the ferromagnetic case, $U_2 = -0.1U_0 < 0$ for the trilayer mean-field system defined by the hamiltonian (2.134) at $T = 0$. We again observe the common Mott lobes. The white lines indicate the Mott to superfluid phase boundary, obtained by numerical minimization of the ground state energy.

with (arbitrary) numerical accuracy. The associated phase diagram is shown in figure 2.13, where the white lines indicate the curve where the order parameters Ψ_σ are just not zero anymore, i.e. the numerical estimation of the mean-field phase boundary.

However, in the antiferromagnetic case $U_2 > 0$ of the trilayer system, the ground state of the $n = 2$ Mott phase is the unique Fock state $|n_+ = 1, n_0 = 0, n_- = 1\rangle$. The uniqueness of this state allows for an easy nondegenerate perturbative treatment via equation (2.124). In the same way as above, we obtain the phase boundary condition for the second Mott lobe which can compactly be written down as

$$\frac{1}{zt} + \frac{2}{\mu - 2U_0} - \frac{1}{\mu - U_0 + U_2} = 0. \tag{2.135}$$

But, around the tip of the lobe, we again observe first order Mott to superfluid transitions, which is why Landau's theory of phase transitions we used within the perturbative approach fails. We can see that in figure 2.14, where the bold white lines mark the phase border obtained by numerical minimization of f, whereas the fine white line at the tip of the second lobe corresponds to the solution set of equation (2.135). Around the area where thin and bold lines differ, first order transitions occur.

Regrettably, the ground states of the first Mott lobe are spanned by the three-fold

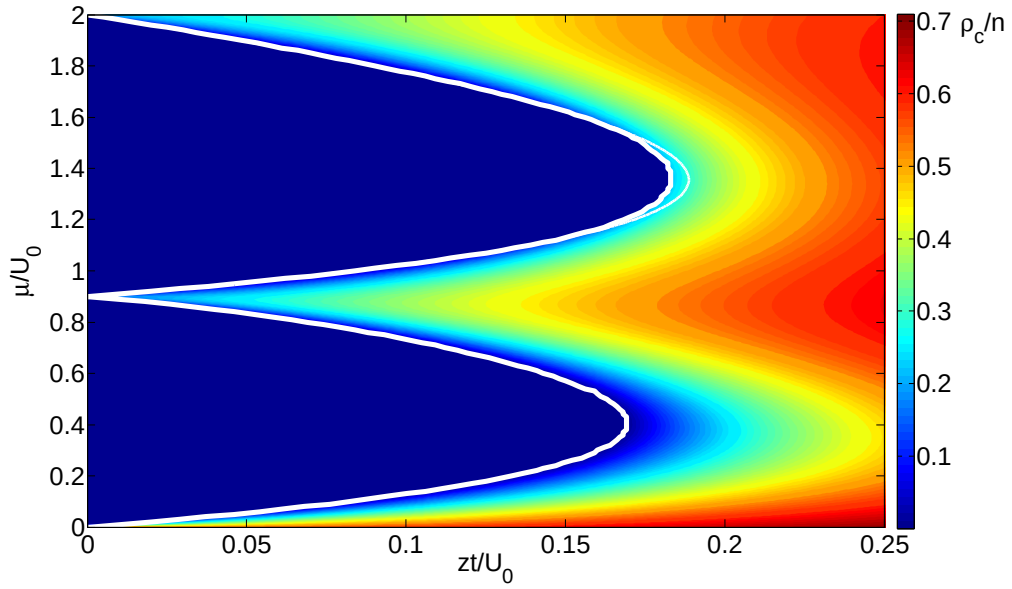

Figure 2.14: ρ_c/n as a function of zt/U_0 and μ/U_0 in the antiferromagnetic case, $U_2 = 0.1U_0 > 0$ for the trilayer mean-field system defined by the Hamiltonian (2.134) at $T = 0$. The white lines show the Mott to superfluid phase boundary. The boundary of the second Mott lobe is obtained perturbatively (thin white line), but disagrees around the tip of the second lobe with the result we get by minimization of f. This is because transitions are of first order in that area.

degenerate Fock states $|n_+, n_0, n_-\rangle = |1,0,0\rangle, |0,1,0\rangle, |0,0,1\rangle$. Thus, perturbation theory becomes again too involved to be covered here.

2.4 Monte Carlo simulations

Monte Carlo methods have a vast scope of application spanning over almost all areas in physics. The basic concept is to sample generic, analytically intractable integrals by random numbers which always comes at the cost of a statistical error. In this work, we focus on Monte Carlo methods as they are used in the field of ultracold gases.

The whole section is self-contained and may be a useful summary for readers new to the field. We start with simple sampling and importance sampling techniques before we have a look on the basic principles on Markov chain Monte Carlo and the Metropolis updating scheme. We are then ready to address Path Integral Monte Carlo and the worm algorithm. The section is closed with a description of two new kinds of updates invented to preserve ergodicity in the trilayer model.

2.4.1 Simple sampling

Let us start with a simple example [46]: suppose we have a function $f(x)$,

$$f(x) = x^n \tag{2.136}$$

and we want to estimate the value of the integral I,

$$I = \int_0^1 f(x)\,\mathrm{d}x. \tag{2.137}$$

The simplest way to get a Monte Carlo estimation for the integral I is to draw M uniformly distributed random numbers x_i, $i = 1 \ldots M$, of the interval $x_i \in [0, 1]$ and evaluate the sample mean $\overline{f}$ of $f(x)$,

$$I \approx \overline{f} = \frac{1}{M} \sum_{i=1}^{M} f(x_i), \tag{2.138}$$

which can be taken as an approximation to the integral I we are interested in. This method is called the *simple sampling method*. To get the error of our estimate, we need to know the sample variance $\overline{\delta f^2}$,

$$\overline{\delta f^2} = \frac{1}{M} \sum_{i=1}^{M} \left(f(x_i) - \overline{f} \right)^2. \tag{2.139}$$

Since we are using uncorrelated random numbers x_i in our estimation, we can use the usual formula [32], for the statistical error δI,

$$\delta I = \sqrt{\overline{\delta f^2}/(M-1)}. \tag{2.140}$$

Looking at equation (2.140), we see that the estimation error δI depends on the variance $\sigma^2 \approx \overline{\delta f^2}$ of the function f in the integration interval. Thus, if the function $f(x)$ we are integrating variates strongly in the integration interval, i.e. if $n \lesssim -1$ or $n \gg 1$ in our example of $f(x) = x^n$, the variance σ^2 of f is high and the estimation for I becomes bad relative to the number of samples M.

2.4.2 Importance sampling

In the case of a large variance σ^2, a more efficient way to evaluate the integral I is given by the *importance sampling method*. We can rewrite equation (2.137) as

$$I = \int_0^1 \frac{f(x)}{p(x)} p(x)\,\mathrm{d}x, \tag{2.141}$$

where we are considering I to be a weighted mean of the function $g(x) = f(x)/p(x)$. Using random numbers y_i that are distributed according to p, I can be estimated via

$$I \approx \frac{1}{M} \sum_{i=1}^{M} g(y_i). \tag{2.142}$$

The advantage of this method compared to simple sampling is that the error of the estimation of I now goes with the sample variance $\overline{\delta g^2}$ of $g(x)$, which can considerably be smoothed out using a random number distribution $p(x)$ that is close to the original function $f(x)$. Importance sampling thus requires some prior knowledge on the function f we want to integrate.

2.4.3 Markov chain Monte Carlo

In both examples above, we were able to use uncorrelated sampling points x_i, y_i. However, in almost all physical problems, it is either highly inefficient or even impossible to generate uncorrelated sampling points or states of a configuration space. To understand this, we take a look at the Ising model (see e.g. [47] for a Monte-Carlo simulation) with the Hamiltonian

$$\hat{H} = -J \sum_{\langle i,j \rangle} \hat{S}_i^z \hat{S}_j^z, \tag{2.143}$$

where the spin operators $\hat{S}_i, \hat{S}_j$ with the eigenvalues $S_i, S_j \pm 1$ are located on a hypercubic lattice and $\langle i, j \rangle$ indicates summation over nearest neighbor sites. Since analytical solutions of the Ising model exist in one and two dimensions [48], it has proven its worth to be a top toy model to study phase transitions. In the ferromagnetic case, $J > 0$, the Ising model on an infinite square lattice undergoes a phase transition at $T_c = \frac{2J/k_b}{log(1+\sqrt{2})}$ with the order parameter magnetization, which is given by

$$\hat{m} = \frac{1}{N} \sum_{i=1}^{N} \hat{S}_i^z, \tag{2.144}$$

where the index i runs over all N sites in the square lattice. The thermal average $\langle \hat{m} \rangle$ in the canonical ensemble is [39]

$$\langle \hat{m} \rangle = \frac{Tr\left[e^{-\beta \hat{H}} \hat{m}\right]}{Tr\left[e^{-\beta \hat{H}}\right]} = \frac{\sum_s \langle \Psi_s | \, e^{-\beta \hat{H}} \hat{m} \, | \Psi_s \rangle}{\sum_s \langle \Psi_s | \, e^{-\beta \hat{H}} \, | \Psi_s \rangle} = \frac{\sum_s m_s e^{-\beta E_s}}{\sum_s e^{-\beta E_s}}, \tag{2.145}$$

where the $|\Psi_s\rangle$ are the eigenstates of the Hamiltonian H labeled by s, and m_s and E_s are the corresponding magnetizations and eigenenergies, respectively. It is easily seen that the eigenstates $|\Psi_s\rangle$ are product states that can be written as

$$|\Psi_s\rangle = \left| S_1^z, S_2^z, \ldots, S_N^z \right\rangle, \tag{2.146}$$

with the spin operator eigenvalues S_i^z in the i-th entry.

What *Markov chain Monte Carlo* does in contrast to direct sampling techniques is *not* to generate mutually independent states $|\Psi_s\rangle$ to probe the configuration space, but states that are constructed out of their directly preceding states. A simple example of such a process would be the flip of a single spin $S_i^z \rightarrow -S_i^z$. This would apparently lead to high correlations within a squence of consecutive states which have to be taken into account with regard to convergence and error estimation.

If we would perform a random walk through the configuration space by flipping one spin at a time, we would sample equation (2.145) in a uniform manner. As we have seen in the previous section, there is a much smarter way. We can rewrite equation (2.145) as

$$\langle \hat{m} \rangle = \frac{\sum_s \langle \Psi_s | \left(e^{-\beta E_s} m_s / P(s) \right) P(s) \, | \Psi_s \rangle}{\sum_s \langle \Psi_s | \left(e^{-\beta E_s} / P(s) \right) P(s) \, | \Psi_s \rangle}, \tag{2.147}$$

which corresponds to the method of importance sampling, where we select the states $|\Psi_s\rangle$ according to the distribution $P(s)$. If we can manage to set $P(s)$ equal to the Boltzmann distribution $e^{-\beta E_s}$, equation (2.147) simplifies to

$$\langle m \rangle = \frac{1}{M} \sum_{i=1}^{M} m_i. \tag{2.148}$$

An algorithm which is capable to sample the states $|\Psi_s\rangle$ according to the Boltzmann distribution is the *Metropolis algorithm* [49].

2.4.3.1 Metropolis algorithm

As stated above, we want to generate a Markov chain of states $\left|\Psi_{s_1}\right\rangle \rightarrow \left|\Psi_{s_2}\right\rangle \rightarrow \ldots \rightarrow \left|\Psi_{s_M}\right\rangle$, where the states are Boltzmann distributed according to their eigenenergies E_{s_i}. This can only be achieved by an appropriate design of the transition probabilities $T_{i\rightarrow j}$ to go from a state $\left|\Psi_{s_i}\right\rangle$ to the state $\left|\Psi_{s_j}\right\rangle$. To this end, we take a look at the master equation for the probability $W_i(s)$ to observe the state $|\Psi_s\rangle$ in the $i-th$ Monte Carlo step,

$$W_i(s) = W_{i-1}(s) + \sum_{s'} \left[T_{s'\rightarrow s} W_{i-1}(s') - T_{s\rightarrow s'} W_{i-1}(s)\right], \tag{2.149}$$

which is nothing more than a continuity equation on the probability $W_i(s)$. In equilibrium, $W_i(s)$ must not depend on the Monte Carlo step i, i.e. $W_i(s) = W(s)$. Hence the master equation reads

$$0 = \sum_{s'} \left[T_{s'\rightarrow s} W(s') - T_{s\rightarrow s'} W(s)\right]. \tag{2.150}$$

A sufficient condition to fulfill equation (2.150) is to claim that each term in the sum over the states s' vanishes separately, i.e.

$$T_{s'\rightarrow s} W(s') = T_{s\rightarrow s'} W(s). \tag{2.151}$$

This is the famous *detailed balance condition*. Although it is not a necessary condition [50] for (2.150) to hold, it is used in most Markov chain Monte Carlo algorithms since it is relatively easy to handle.

In the Metropolis algorithm, the condition of detailed balance is fulfilled by setting the transition probabilities $T_{s\rightarrow s'}$ to

$$T_{s\rightarrow s'} = min\left(1, \frac{W(s')}{W(s)}\right). \tag{2.152}$$

As we want W to be the Boltzmann distribution $W(s) = Z^{-1} e^{-\beta E_s}$, this becomes

$$T_{s\rightarrow s'} = min\left(1, e^{-\beta\left(E_{s'} - E_s\right)}\right), \tag{2.153}$$

i.e. we take the proposed step $s \rightarrow s'$ with acceptance probability $q = 1$ if $E_{s'} \leq E_s$ and with probability $q = e^{-\beta\left(E_{s'} - E_s\right)}$ if $E_{s'} > E_s$.

We can summarize the Metropolis algorithm for the simple Ising model with a short recipe [32]:

Single spin flip Metropolis algorithm for the simple Ising model

(1) Choose an initial state $|\Psi_1\rangle = |S_1, S_2, \ldots, S_N\rangle$.

(2) Choose a random site i to flip the spin, $S_i \to -S_i$.

(3) Calculate the difference in energy $\Delta E = E_{\text{after}} - E_{\text{before}}$ of energies before and after the update.

(4) Draw a uniformly distributed random number $x \in [0, 1]$.

(5) If $x < e^{-\beta \Delta E}$, flip the spin. Otherwise do nothing.

(6) Compute the magnetization expectation value $\langle m \rangle$ in the generated state and account for it in the thermal average given by equation (2.148).

(7) Go back to (2).

The Metropolis algorithm was further developed by Hastings in 1970 [51], who first introduced the concept of *a priori probabilities*.

2.4.3.2 A priori probabilities

Imagine we are in step (2) of the single spin flip Metropolis algorithm described in the box above. For an Ising model with N sites, there are $N + 1$ possibilities for the next state of the Markov chain, namely to flip one of the N spins or to stay in the state we already are, not changing any spin. Whilst staying in the state we are is implied via Metropolis rejection, we are not forced to draw one of the other N possible states with a uniform probability distribution. We are rather free to choose the flipping site i with any other *a priori probability distribution* we believe to be meaningful (the single spin flip algorithm may not be a good example here - we do not gain anything if we go off the uniform distribution in that case).

The only thing we have to pay attention to is to fulfill the detailed balance condition, equation (2.151). The transition probability $T_{s \to s'}$ to go from state s to s' is then split up in two parts,

$$T_{s \to s'} = A_{s \to s'} p_{s \to s'}, \tag{2.154}$$

where $A_{s \to s'}$ is the probability to propose to go to state s' being in state s, and $p_{s \to s'}$ is the still necessary acceptance probability. The detailed balance condition is now

given by

$$A_{s'\to s} p_{s'\to s} W(s') = A_{s\to s'} p_{s\to s'} W(s), \tag{2.155}$$

which is fulfilled if the acceptance probability reads

$$p_{s\to s'} = min\left(1, \frac{W(s')}{A_{s\to s'}} \frac{A_{s'\to s}}{W(s)}\right), \tag{2.156}$$

which reduces to (2.152) for symmetric proposal functions $A_{s\to s'} = A_{s'\to s}$.

To get representative samples of our observables, it is important to quickly go around in configuration space. This means we have to keep rejection probabilities small, which can be done using appropriate proposal functions $A_{s\to s'}$.

2.4.3.3 Ergodicity

It is indispensable for every Monte Carlo simulation to fulfill the principle of *ergodicity*. Ergodicity means that every configuration of the system should be attainable according to its Boltzmann weight in a reasonable amount of simulation time, no matter which initial state we have chosen. Let us, for instance, consider the Ising model deep in the ferromagnetic phase: in this phase, all spins are either pointing up ($\langle\hat{m}\rangle = 1$) or pointing down ($\langle\hat{m}\rangle = -1$), both cases occuring with the same Boltzmann weight $Z^{-1} exp\left(-\beta E_{\langle\hat{m}\rangle=\pm1}\right) \approx 0.5$. In that regime, the single spin flip algorithm described above is not ergodic anymore: to go from the state where $\langle\hat{m}\rangle = 1$ to the state where $\langle\hat{m}\rangle = -1$, we have to pass all the states with any other magnetization in between. These states are very unlikely to be hit in the ferromagnetic limit, and going through all of them practically never happens. A simple solution to that problem would be the integration of an update that is capable to flip more than one spin at once, as for example in the Cluster algorithm by Swendsen, Wang [52] and Wolff [53].

In our Monte-Carlo simulation of the trilayer system 2.28, we were faced with a very similar problem, which we were able to circumvent by introduction of the Monte-Carlo update schemes described in section 2.4.5.3.

2.4.4 Path integral Monte Carlo

2.4.4.1 Path integral decomposition of the grand canonical partition function

In this section, we derive a representation of the grand canonical partition function using the Feynman path integral formulation, which is the basis of a whole class of Monte Carlo algorithms for quantum many body systems. We closely follow [29] here.

The dynamics of a quantum system is thoroughly described by the Schrödinger equation,

$$i\frac{\partial}{\partial t}\left|\Psi_S(t)\right\rangle = \hat{H}\left|\Psi_S(t)\right\rangle, \tag{2.157}$$

where we assume that the Hamiltonian $\hat{H}$ does not depend explicitly on time. States at different times are connected by the unitary time evolution operator [44] $\hat{U}_S(t,t_0)$ as

$$\left|\Psi_S(t)\right\rangle = \hat{U}_S(t,t_0)\left|\Psi_S(t_0)\right\rangle = e^{-i(t-t_0)\hat{H}}\left|\Psi_S(t_0)\right\rangle. \tag{2.158}$$

Given the solution to the Schrödinger equation at t_0, it is thus easy to generate solutions at generic times t. Equation (2.157) is the equation of motion of the so-called *Schrödinger picture*, where it is assumed that the states $\left|\Psi_S(t)\right\rangle$ are generally time dependent, whereas operators can at most depend explicitly on time.

In the case of a time independent Hamiltonian $\hat{H}$ that can be written as

$$\hat{H} = \hat{H}_0 + \hat{H}_1, \tag{2.159}$$

we can define the *interaction picture* by the interaction state vector

$$\left|\Psi_I(t)\right\rangle := e^{i\hat{H}_0 t}\left|\Psi_S(t)\right\rangle. \tag{2.160}$$

The equation of motion of this wave function can be obtained using the Schrödinger equation (2.157) and reads

$$i\frac{\partial}{\partial t}\left|\Psi_I(t)\right\rangle = \hat{H}_1(t)\left|\Psi_I(t)\right\rangle \qquad \hat{H}_1 = e^{i\hat{H}_0 t}\hat{H}_1 e^{-i\hat{H}_0 t}. \tag{2.161}$$

By making use of equations (2.157) and (2.158), we get the time evolution operator

for the state $|\Psi_I(t)\rangle$,

$$|\Psi_I(t)\rangle = \hat{U}_I(t, t_0)\,|\Psi_I(t_0)\rangle = e^{i\hat{H}_0 t} e^{-i\hat{H}(t-t_0)} e^{-i\hat{H}_0 t_0}\,|\Psi_I(t_0)\rangle\,. \tag{2.162}$$

So far we do not see any connection to the grand canonical partition function that we want to express in a path integral decomposition. To this end, we have to introduce the concept of *imaginary time*. We call $\tau = it$ and rewrite the time evolution operator of the interaction picture as

$$\hat{U}_I(\tau, \tau_0) = e^{\hat{H}_0 \tau} e^{-\hat{H}(\tau-\tau_0)} e^{-\hat{H}_0 \tau_0}, \tag{2.163}$$

explicitly allowing τ to assume real values (we can go back and forth from real to imaginary time by means of analytic continuation; see e.g. [29] for a thorough discussion). Note that $\hat{U}_I$ is now in general not unitary anymore.

From (2.163), we can deduce the equation

$$e^{-\hat{H}\tau} = e^{-\hat{H}_0 \tau} \hat{U}_I(\tau, 0)\,. \tag{2.164}$$

Setting $\tau = \beta$ and taking the trace, we recover the partition function

$$Z = Tr\left[e^{-\beta\hat{H}}\right] = Tr\left[e^{-\beta\hat{H}_0}\hat{U}_I(\beta, 0)\right] = \sum_i \langle i|\, e^{-\beta\hat{H}_0}\hat{U}_I(\beta, 0)\,|i\rangle\,. \tag{2.165}$$

The crucial point is that we can perturbatively expand the operator $\hat{U}(\tau, \tau_0)$. For that purpose, we derive $\hat{U}_I(\tau, \tau_0)$ with respect to τ,

$$\frac{\partial}{\partial\tau}\hat{U}_I(\tau, \tau_0) = -\hat{H}_1(\tau)\hat{U}_I(\tau, \tau_0)\,. \tag{2.166}$$

Integrating on both sides from τ_0 to τ yields

$$\hat{U}_I(\tau, \tau_0) = 1 - \int_{\tau_0}^{\tau} \mathrm{d}\tau_1 \hat{H}_1(\tau_1)\hat{U}_I(\tau_1, \tau_0)\,. \tag{2.167}$$

Without proof of convergence, we iteratively solve this integral equation and obtain

$$\begin{aligned}\hat{U}_I(\tau, \tau_0) &= 1 - \int_{\tau_0}^{\tau} \mathrm{d}\tau_1 \hat{H}_1(\tau_1) + \int_{\tau_0}^{\tau} \mathrm{d}\tau_2 \int_{\tau_0}^{\tau_2} \mathrm{d}\tau_1 \hat{H}_1(\tau_2)\hat{H}_1(\tau_1) + \dots \\ &= 1 - \int_{\tau_0}^{\tau} \mathrm{d}\tau_1 \hat{H}_1(\tau_1) + \sum_{n=2}^{\infty}(-1)^n \int_{\tau_0}^{\tau} \mathrm{d}\tau_n \dots \int_{\tau_0}^{\tau_2} \mathrm{d}\tau_1 \hat{H}_1(\tau_n) \dots \hat{H}_1(\tau_1).\end{aligned} \tag{2.168}$$

We insert this into equation (2.165) and make use of the completeness relation by

inserting $n-1$ identity operators $1 = \sum_i |i\rangle\langle i|$ between the products of n $\hat{H}_1$ operators to evaluate the trace to get

$$\begin{aligned} Z = \sum_{i=0}^{\infty} e^{-\beta E_i} + \sum_{n=1}^{\infty} \sum_{|i_1\rangle,\ldots,|i_n\rangle} (-1)^n \int_0^{\beta} \mathrm{d}\tau_n \ldots \int_0^{\tau_2} \mathrm{d}\tau_1 \langle i_1| \hat{H}_1 |i_n\rangle \cdot \\ e^{-(\tau_n-\tau_{n-1})E_{i_n}} \cdot \langle i_n| \hat{H}_1 |i_{n-1}\rangle \cdot e^{-(\tau_{n-1}-\tau_{n-2})E_{i_{n-1}}} \cdot \ldots \cdot \\ \langle i_3| \hat{H}_1 |i_2\rangle \cdot e^{-(\tau_2-\tau_1)E_{i_2}} \langle i_2| \hat{H}_1 |i_1\rangle e^{-(\beta-\tau_n+\tau_1)E_{i_1}}, \end{aligned} \tag{2.169}$$

where we have chosen the inserted basis sets $\left|i_j\right\rangle$ to be the eigenbasis of $\hat{H}_0$ with the eigenenergies $\hat{H}_0 \left|i_j\right\rangle = E_{i_j} \left|i_j\right\rangle$.

The configuration space can now be seen as the set of all possible combinations of the expansion order n, the imaginary times of the matrix elements of $\hat{H}_1$, $\tau_1 \ldots \tau_n$, and the inserted basis sets $|i_1\rangle \ldots |i_n\rangle$.

At this point, the partition function Z of the d-dimensional quantum system corresponds to that of a $d+1$-dimensional classical system with the additional dimension of imaginary time τ. As the trace of equation (2.165) implies that the first Bra and the last Ket in (2.169) are identical, we see that τ is periodic with periodicity β.

2.4.4.2 Path integral Monte Carlo for the trilayer Hamiltonian

In this work, we primarly study the Hamiltonian introduced in equation (2.28),

$$\begin{aligned} \hat{H} = -t \sum_{\langle i,j\rangle,\sigma} \left(\hat{b}^{\dagger}_{i,\sigma}\hat{b}_{j,\sigma} + \hat{b}^{\dagger}_{j,\sigma}\hat{b}_{i,\sigma}\right) + \frac{U_0}{2} \sum_i \hat{n}_i(\hat{n}_i - 1) - \mu \sum_i \hat{n}_i \\ + \frac{U_2}{2} \sum_i (\hat{n}^2_{i+} - 2\hat{n}_{i+}\hat{n}_{i-} + \hat{n}^2_{i-} - \hat{n}_{i+} - \hat{n}_{i-} + 2\hat{n}_{i0}\hat{n}_{i+} + 2\hat{n}_{i0}\hat{n}_{i-}). \end{aligned}$$

In our Monte Carlo simulation, we work in the site and spin occupation number basis. As an algorithmic trick, we compute a $3d$ system that measures only three sites in z-direction. We then get three stacked layers, each occupied only by one specific spin species so that we use the z-coordinate as a spin index, see figure 2.15. The most convenient choice is to collect all diagonal terms in $\hat{H}_0$, whereas the one-body tunneling operators of the kinetic term are treated as perturbations $\hat{H}_1$. With this choice, the negative sign of the kinetic term cancels with the $(-1)^n$ of the path integral expansion and we can be sure not to run into any sign problem. A single state out of the configuration space of this system can nicely be visualized diagrammatically, see figure 2.16.

The matrix elements $\langle i_k| \hat{H}_1 |i_{k+1}\rangle$ are only nonzero if the states differ just by the hopping of a particle to one of its nearest neighbor sites, i.e. if $|i_k\rangle \propto \hat{b}^{\dagger}_j \hat{b}_l |i_{k+1}\rangle$,

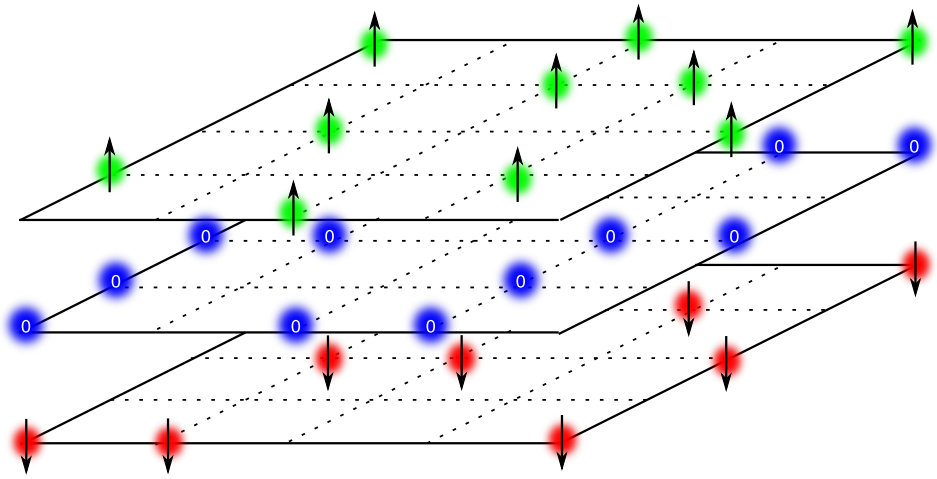

Figure 2.15: Schematic representation of a Fock state in the trilayer setup. We use the already existing code for the 3d Bose-Hubbard model and use the site index in z-direction as spin index σ. The worm can only propagate in a single layer, interlayer hopping t_z is set to zero.

where j and l are adjacent sites. In the following, we refer to these matrix elements as *hoppings*, *interactions* or *kinks*.

We see that a state out of the partition function corresponds to a configuration of closed loops, called worldlines, in the site - imaginary time space, where a single loop depicts a particle starting at some site $i\sigma$ at $\tau = 0$, then hopping to other sites at later times τ, finally closing on itself again on site $i\sigma$ at $\tau = 0$ (keep in mind the β-periodicity of τ). The job of our path integral Monte Carlo algorithm is to sample all these closed loop configurations according to their respective weights given by

$$\begin{aligned} W = &\langle i_1| \hat{H}_1 |i_n\rangle \cdot e^{-(\tau_n - \tau_{n-1})E_{i_n}} \cdot \langle i_n| \hat{H}_1 |i_{n-1}\rangle \cdot e^{-(\tau_{n-1} - \tau_{n-2})E_{i_{n-1}}} \cdot \ldots \cdot \\ &\cdot \langle i_3| \hat{H}_1 |i_2\rangle \cdot e^{-(\tau_2 - \tau_1)E_{i_2}} \langle i_2| \hat{H}_1 |i_1\rangle e^{-(\beta - \tau_n + \tau_1)E_{i_1}}. \end{aligned} \tag{2.170}$$

For example, this may be done using local updates [54], where a pair of hopping elements is inserted that causes a particle to hop to one of its neighboring sites and back at some later time.

Since the number of particles in the system is given by the number of loops winding around imaginary time direction, an algorithm based only on such local updates can not sample the grand canonical partition function Z, because it is not able to insert or remove closed loops and therefore particles.

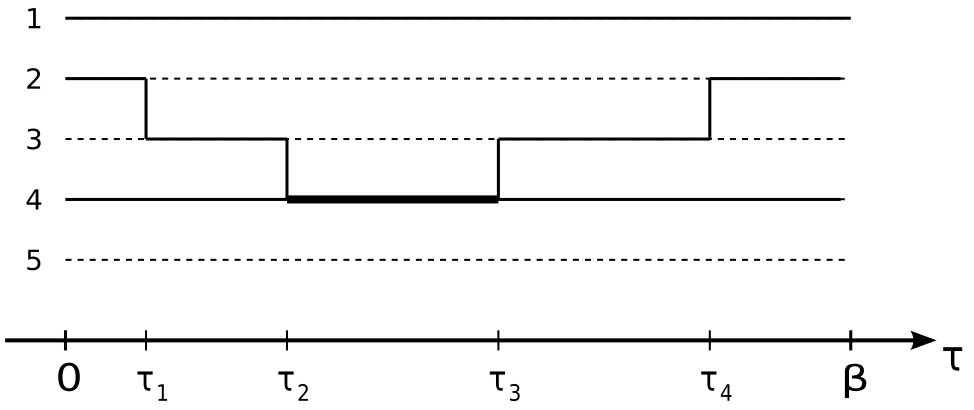

Figure 2.16: Diagrammatic visualization of a typical configuration of the partition function (2.169) for the trilayer Bose-Hubbard model. There are five sites shown, imaginary time τ runs from left to right. Dashed lines indicate that the site is unoccupied, fine solid lines denotes single and bold lines double occupation. At the times τ_j, particles hop from one side to another, corresponding to the matrix elements $\left\langle i_j \right| \hat{H}_1 \left| i_{j-1} \right\rangle$. Between two instants τ_j and τ_{j-1}, the system is in the Fock state $\left| i_j \right\rangle$ with diagonal energy E_{i_j}.

Furthermore, using periodic boundary conditions, the superfluid density ρ_{sf} is directly related to the winding number w of loops winding around the spatial directions [33] by

$$\rho_{sf} = \frac{\left\langle w^2 \right\rangle L^{2-d}}{2td\beta}.$$

Also, w cannot be changed using merely local updates.

2.4.5 The worm algorithm

A particularly efficient updating scheme is given by the *worm algorithm* [11, 12], which does not suffer from the ergodicity problems concerning particle and winding numbers mentioned above. It is capable to sample the grand canonical partition function with the aid of a further disconnected worldline, the so-called *worm*, see figure 2.17. Along the way, it samples the Matsubara Green function

$$G\left(i\sigma, j\sigma, \tau, \tau_0\right) = \left\langle \hat{\mathcal{T}}_\tau \hat{b}_{i\sigma}\left(\tau_0\right) \hat{b}^\dagger_{j\sigma}\left(\tau\right) \right\rangle = \mathrm{Tr}\left[\hat{\mathcal{T}}_\tau \hat{b}_{i\sigma}\left(\tau_0\right) \hat{b}^\dagger_{j\sigma}\left(\tau\right) e^{-\beta \hat{H}} \right], \qquad (2.171)$$

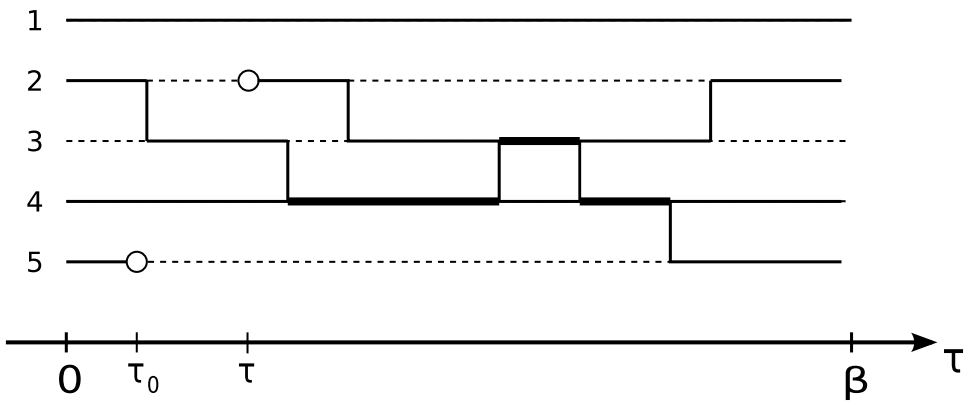

Figure 2.17: Similar diagram as 2.16, but this time with an additional open-ended worldline called worm. Worm head an tail are indicated by circles. This configuration does not belong to the partition function Z anymore, it is rather part of the so-called extended partition function Z_e, equation (2.172).

with $\hat{\mathcal{T}}_\tau$ the time ordering operator. The sum over all possible Green functions defines the *extended partition function*

$$Z_e = \sum_{n=0}^{\infty} \sum_{|i_1\rangle,\ldots,|i_n\rangle} \sum_{i\sigma,j\sigma} \int_0^\beta \mathrm{d}\tau_n \ldots \int_0^{\tau_2} \mathrm{d}\tau_1 W, \tag{2.172}$$

where W is given by

$$\begin{aligned} W = \langle i_1 | \hat{H}_1 | i_2 \rangle \cdot e^{-(\tau_2-\tau_1)E_{i_2}} \cdot \langle i_2 | \hat{H}_1 | i_3 \rangle \cdot e^{-(\tau_3-\tau_2)E_{i_3}} \cdot \ldots \cdot e^{-(\tau_k-\tau_{k-1})E_{i_k}} \langle i_k | \hat{b}^\dagger_{i\sigma} | i_{k+1} \rangle \cdot \\ \ldots \cdot e^{-(\tau_l-\tau_{l-1})E_{i_l}} \langle i_l | \hat{b}_{j\sigma} | i_{l+1} \rangle \cdot \ldots \cdot e^{-(\tau_n-\tau_{n-1})E_n} \langle i_n | \hat{H}_1 | i_1 \rangle e^{-(\beta-\tau_n+\tau_1)E_{i_1}}. \end{aligned} \tag{2.173}$$

It is important to keep in mind the time ordering also for the worm operators $\hat{b}^\dagger_{i\sigma}(\tau) = \hat{b}^\dagger_{i\sigma}(\tau_k)$, $\hat{b}_{j\sigma}(\tau_0) = \hat{b}_{j\sigma}(\tau_l)$.

The extended configuration space is composed of all possible combinations of the expansion order n, inserted basis sets $|i_1\rangle \ldots |i_n\rangle$, hopping times $\tau_1 \ldots \tau_n$ and the sites $i\sigma$, $j\sigma$ and times τ_0, τ of the two worm ends. The worm algorithm samples these configurations according to their weights given in (2.173) as it moves one of the worm ends, called the *worm head*, through the configuration space. When the worm head encounters the other end of the worm, called the *worm tail*, the worm closes and the

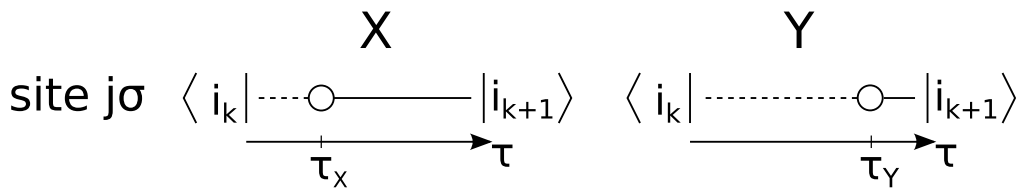

Figure 2.18: Graphical representation of the *move update*. The worm head $\hat{b}_{j\sigma}$ resides at site $j\sigma$ at τ_X in configuration X. The *move update* proposes to go to another point in time τ_Y leaving the system in configuration Y. The system is in the Fock state $|i_k\rangle$ before the worm head and in $|i_{k+1}\rangle$ afterwards. The corresponding diagonal energies are denoted by E_{i_k} and $E_{i_{k+1}}$.

configuration is part of the partition function Z, except for the worm matrix element $\langle i_k| \hat{b}_{i\sigma}(\tau_0)\hat{b}^\dagger_{i\sigma}(\tau_0) |i_k\rangle$. This matrix element defines a relative weight between the extended and the original partition function and can be chosen freely, but is usually set to 1.

Clearly, we are free to choose either $\hat{b}^\dagger_{i\sigma}$ or $\hat{b}_{i\sigma}$ as the mobile end of the worm, just as we are free to move up- or downwards in imaginary time τ. For convenience, we always take $\hat{b}_{i\sigma}$ to be the worm head moving in positive imaginary time direction in the following description of worm updates.

2.4.5.1 Worm type updates

To ensure that all configurations are sampled in accordance with their weights (2.173), we have to respect the detailed balance condition (2.155), which led us to the acceptance probability

$$p_{X\to Y} = min\left(1, \frac{W(Y)}{A_{X\to Y}}\frac{A_{Y\to X}}{W(X)}\right)$$

for a step from configuration X to Y. We see that only relative weights matter, so all common factors of $W(X)$, $W(Y)$ cancel out directly.

In the following, we give an overview over all worm type updates in the algorithm we use [55].

Move in imaginary time

The first type of update we are considering is a step of the worm head in imaginary time, see figure 2.18. In a given configuration X, the worm head $\hat{b}_{j\sigma}$ resides at site $j\sigma$ at a time τ_X. The *move update* proposes to move the worm head to some later or

earlier time τ_Y, staying on the same site $j\sigma$. The non-canceling factors of the weights $W(X)$, $W(Y)$ read

$$\begin{aligned} W(X) &= e^{-\tau_X\left(E_{i_k}-E_{i_{k+1}}\right)}, \\ W(Y) &= e^{-\tau_Y\left(E_{i_k}-E_{i_{k+1}}\right)}, \end{aligned} \tag{2.174}$$

so the acceptance ratio for the move update becomes

$$p_{X\to Y} = min\left(1, \frac{e^{-\Delta\tau E_{i_k}}}{e^{-\Delta\tau E_{i_{k+1}}}} \frac{A_{Y\to X}}{A_{X\to Y}}\right). \tag{2.175}$$

where $\Delta\tau = \tau_Y - \tau_X$. We want to choose the proposal functions $A_{X\to Y}$, $A_{Y\to X}$ such that rejections are minimal, that means that nominator and denominator in equation (2.175) should always be of the same order of magnitude. It would therefore be a good choice if they contain the exponentials,

$$\begin{aligned} A_{X\to Y} &\propto e^{-\Delta\tau E_{i_k}}, \\ A_{Y\to X} &\propto e^{-\Delta\tau E_{i_{k+1}}}. \end{aligned} \tag{2.176}$$

In order that the proposal functions are valid probability distributions, we have to ensure that the exponents are always negative. This means that, under the assumption that we are moving in positive time direction $\Delta\tau > 0$, the diagonal energies E_{i_k}, $E_{i_{k+1}}$ have to be positive. Since only energy differences physically matter, we are free to shift the energies like

$$\mathcal{E}_{i_k,i_{k+1}} = E_{i_k,i_{k+1}} - min\left(E_{i_k}, E_{i_{k+1}}\right) + E_{\text{off}}, \tag{2.177}$$

where the inclusion of the offset energy E_{off} will become clear shortly. Properly normalized, the proposal functions look like

$$\begin{aligned} A_{X\to Y} &= \mathcal{E}_{i_k} e^{-\Delta\tau\mathcal{E}_{i_k}}, \\ A_{Y\to X} &= \mathcal{E}_{i_{k+1}} e^{-\Delta\tau\mathcal{E}_{i_{k+1}}}. \end{aligned} \tag{2.178}$$

The acceptance probability then becomes

$$p_{X\to Y} = min\left(1, \frac{\mathcal{E}_{i_{k+1}}}{\mathcal{E}_{i_k}}\right) = min\left(1, \frac{E_{i_{k+1}} - min\left(E_{i_k}, E_{i_{k+1}}\right) + E_{\text{off}}}{E_{i_k,} - min\left(E_{i_k}, E_{i_{k+1}}\right) + E_{\text{off}}}\right). \tag{2.179}$$

It is now clear that the offset energy is needed to ensure that we have a non-zero denominator. Though a vanishing denominator would theoretically be no problem,

difficulties with anomalously long worms and ergodicity are described in [55].

Up to now, we did not specify what happens if the worm encounters an interaction during its time step. Both the diagonal energies and matrix elements might change. We first focus on the Matrix elements. Suppose we have a worm head $\hat{b}_{i\sigma}$ residing on site $i\sigma$ at time τ_X just before the hopping matrix element $\langle i_{k+1}| \hat{H}_1 |i_{k+2}\rangle = \langle i_{k+1}| \hat{b}^\dagger_{j\sigma'} \hat{b}_{l\sigma'} |i_{k+2}\rangle$. The relevant factors in the partition function are

$$\sum_{|i_{k+1}\rangle} \ldots \langle i_k| \hat{b}_{i\sigma} |i_{k+1}\rangle \langle i_{k+1}| \hat{b}^\dagger_{j\sigma'} \hat{b}_{l\sigma'} |i_{k+2}\rangle \ldots = \ldots \langle i_k| \hat{b}_{i\sigma} \hat{b}^\dagger_{j\sigma'} \hat{b}_{l\sigma'} |i_{k+2}\rangle \ldots . \quad (2.180)$$

If $i\sigma \neq j\sigma'$, all operators commute and we can pass the hopping operators to get

$$\begin{aligned} &\ldots \langle i_k| \hat{b}_{i\sigma} \hat{b}^\dagger_{j\sigma'} \hat{b}_{l\sigma'} |i_{k+2}\rangle \ldots = \ldots \langle i_k| \hat{b}^\dagger_{j\sigma'} \hat{b}_{l\sigma'} \hat{b}_{i\sigma} |i_{k+2}\rangle \ldots \\ &= \sum_{|\tilde{i}_{k+1}\rangle} \ldots \langle i_k| \hat{b}^\dagger_{j\sigma'} \hat{b}_{l\sigma'} \left|\tilde{i}_{k+1}\right\rangle \left\langle \tilde{i}_{k+1}\right| \hat{b}_{i\sigma} |i_{k+2}\rangle \ldots . \end{aligned} \quad (2.181)$$

However, in the case where the worm head does not commute with the hopping matrix element, we are not allowed to simply pass. This happens if the worm head $\hat{b}_{i\sigma}$ tries to pass an interaction from $i\sigma$ to $l\sigma$, $\hat{b}^\dagger_{i\sigma} \hat{b}_l$. We then stop at the interaction and propose a new Monte Carlo step. This means that, if such an interaction happens at $\Delta\tau_{\text{int}}$ after the worm head, our proposal function becomes

$$A_{X\to Y} = \begin{cases} \mathcal{E}_{i_k} e^{-\Delta\tau \mathcal{E}_{i_k}} & \text{if} \Delta\tau < \Delta\tau_{\text{int}}, \\ \int_{\Delta\tau_{\text{int}}}^{\infty} \mathcal{E}_{i_k} e^{-\Delta\tau \mathcal{E}_{i_k}} \mathrm{d}\Delta\tau & \text{if} \Delta\tau = \Delta\tau_{\text{int}}, \\ 0, & \text{otherwise.} \end{cases} \quad (2.182)$$

Also, by passing an interaction, the diagonal energies E before and after the worm head as well as before and after the passed interaction may possibly change. Suppose again that the worm head is on site $i\sigma$ at time τ_X, and it is proposed to go to the time τ_Y by passing an interaction from $j\sigma'$ to $l\sigma'$ at time τ_{int}. The relevant factors are then

$$\begin{aligned} W(X) = &\ldots \langle i_k| \hat{b}_{i\sigma} |i_{k+1}\rangle \langle i_{k+1}| \hat{b}^\dagger_{j\sigma'} \hat{b}_{l\sigma'} |i_{k+2}\rangle \cdot \\ &\cdot \exp\left(-\tau_X \left(E_{i_k} - E_{i_{k+1}}\right) - \tau_{\text{int}} \left(E_{i_{k+1}} - E_{i_{k+2}}\right)\right) \ldots , \\ W(Y) = &\ldots \langle i_k| \hat{b}^\dagger_{j\sigma'} \hat{b}_{l\sigma'} |\tilde{i}_{k+1}\rangle \langle \tilde{i}_{k+1}| \hat{b}_{i\sigma} |i_{k+2}\rangle \cdot \\ &\cdot \exp\left(-\tau_{\text{int}} \left(E_{i_k} - E_{\tilde{i}_{k+1}}\right) - \tau_Y \left(E_{\tilde{i}_{k+1}} - E_{i_{k+2}}\right)\right) \ldots . \end{aligned} \quad (2.183)$$

We are only allowed to pass the interaction if the relative weight $W(Y)/W(X)$ remains the same as if there was no interaction in between the step we want to take. That

means that it is a necessary condition that

$$\begin{aligned}\frac{W(Y)}{W(X)} &= \exp\left(-\tau_{\text{int}}\left(E_{i_k} - E_{\tilde{i}_{k+1}} + E_{i_{k+2}} - E_{i_{k+1}}\right) - \tau_Y\left(E_{\tilde{i}_{k+1}} - E_{i_{k+2}}\right) + \tau_X\left(E_{i_k} - E_{i_{k+1}}\right)\right) \\ &\stackrel{!}{=} \exp\left(-\Delta\tau\left(E_{i_k} - E_{i_{k+2}}\right)\right). \end{aligned} \tag{2.184}$$

Let us check that condition first for an interaction that does not involve the worm head site, i.e. $i \neq j, i \neq k$, but the spins σ, σ' may be the same.In equation (2.184), we are only faced with diagonal energy differences, and we surely know that the energies E can only differ in terms involving the occupation numbers $n_{i\sigma}, n_{j\sigma'}, n_{k\sigma'}$. Furthermore, looking at the Hamiltonian given in equation (2.28), we see that there are no diagonal terms that mix different sites. We thus write the diagonal energies as sums of the on-site energies E which depend on the occupation numbers $n_{i\sigma}(|i\rangle), n_{j\sigma'}(|i\rangle), n_{k\sigma'}(|i\rangle)$. Calling these occupation numbers in state $|i_k\rangle$ $n_{i\sigma}, n_{j\sigma'}$ and $n_{k\sigma'}$, we can write

$$\begin{aligned} E_{i_k} &= E\left(n_{i\sigma}\right) + E(n_{j\sigma'}) + E\left(n_{k\sigma'}\right), \\ E_{i_{k+1}} &= E(n_{i\sigma} + 1) + E(n_{j\sigma'}) + E(n_{k\sigma'}), \\ E_{i_{k+2}} &= E(n_{i\sigma} + 1) + E(n_{j\sigma'} - 1) + E(n_{k\sigma'} + 1), \\ E_{\tilde{i}_{k+1}} &= E(n_{i\sigma}) + E(n_{j\sigma'} - 1) + E(n_{k\sigma'} + 1). \end{aligned}$$

Inserting that into equation (2.184), we end up with

$$\begin{aligned}\frac{W(Y)}{W(X)} &= \exp\left(-\tau_Y\left(E(n_{i\sigma}) - E(n_{i\sigma} + 1)\right) + \tau_X\left(E(n_{i\sigma}) - E(n_{i\sigma} + 1)\right)\right) \\ &= \exp\left(-\Delta\tau\left(E_{i_k} - E_{i_{k+2}}\right)\right), \end{aligned} \tag{2.185}$$

which is exactly the condition that allows the worm head to pass interactions that do not happen on the worm head site.

Next, we consider the case where the worm head $\hat{b}_{i\sigma}$ passes an interaction that happens on the same site $\hat{b}^\dagger_{i\sigma'}\hat{b}_{j\sigma'}$, but in a different spin layer $\sigma' \neq \sigma$ (the case where $\sigma' = \sigma$ was already treated above). The relevant occupation numbers are now $n_{i\sigma}(|i\rangle), n_{i\sigma'}(|i\rangle), n_{j\sigma'}(|i\rangle)$, and we call $n_{i\sigma}, n_{i\sigma'}, n_{j\sigma'}$ the occupation numbers in the state $|i_k\rangle$. Since the hamiltonian (2.28) contains mixed terms of particles with different spin

on the same site, we are only allowed to split the energies as

$$\begin{aligned} E_{i_k} &= E(n_{i\sigma}, n_{i\sigma'}) + E(n_{j\sigma'}), \\ E_{i_{k+1}} &= E(n_{i\sigma} + 1, n_{i\sigma'}) + E(n_{j\sigma'}), \\ E_{i_{k+2}} &= E(n_{i\sigma} + 1, n_{i\sigma'} - 1) + E(n_{j\sigma'} + 1), \\ E_{\tilde{i}_{k+1}} &= E(n_{i\sigma}, n_{i\sigma'} - 1) + E(n_{k\sigma'} + 1). \end{aligned}$$

Plugging that in to equation (2.184), we immediately see that the necessary condition to pass the interaction cannot be fulfilled generically. We thus have to stop the worm head each time it encounters an interaction that happens on the same physical site i, but in a different spin layer $\sigma' \neq \sigma$. We then proceed again by proposing a new Monte Carlo step.

Let us give a short summary of the move update here [55]:

The move update in the trilayer Bose-Hubbard worm algorithm

(1) Draw a random time step $\Delta\tau$ that is distributed according to the proposal distribution equation (2.178). Practically, this is implemented by drawing a uniformly distributed random number $u \in [0, 1)$, and then computing the exponentially distributed time shift window by $\Delta\tau = -\log(u)/E$, where E is the diagonal energy of the Fock state before (after) the worm head for moves in positive (negative) imaginary time direction.

(2) If no interaction happens on the worm head site i between τ_X and τ_Y, change the worm head time from τ_X to τ_Y.

(3) If an interaction happens that does not commute with the worm head at time $\tau_X < \tau_{\text{int}} < \tau_Y$, only update the worm time to τ_{int}.

(4) If an interaction happens at $\tau_X < \tau_{\text{int}} < \tau_Y$ on the same site i as the worm head, but in another spin layer $\sigma' \neq \sigma$, we also have to stop the worm there, updating its time from τ_X to τ_{int}.

Inserting an interaction

To ergodically map the configuration space using the worm algorithm, we clearly need an update scheme that generates hoppings to nearest neighboring sites, i.e. matrix elements of the kinetic term $\langle i_k | \hat{H}_1 | i_{k+1} \rangle$. This is done by proposing to the worm

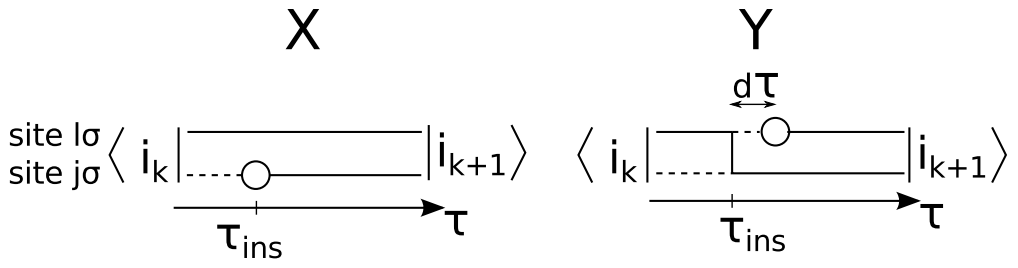

Figure 2.19: Schematic representation of the *insert kink update*. The worm head, residing on site $j\sigma$ in configuration X, hops to its neighboring site $l\sigma$ in configuration Y. Note that this update is only possible if the worm is not forced to stop at an interaction. The sign of the infinitesimal time step $d\tau$ determines the time direction in which the worm will move after the hopping has happened - it therefore defines the order of the operators in the weights of equation (2.186).

head to hop to one of its adjacent sites, see figure 2.19. This kind of update is only possible if the worm head is not forced to stop at an interaction, as described in step **(2)** of the box above.

The relevant weights of a worm head $\hat{b}_{j\sigma}$ jumping from site $j\sigma$ to site $l\sigma$ as depicted in figure 2.19 are given by

$$\begin{aligned} W(X) &= e^{-\tau_{\text{ins}} E_{i_k}} \left\langle i_k \left| \hat{b}_{j\sigma} \right| i_{k+1} \right\rangle e^{\tau_{\text{ins}} E_{i_{k+1}}}, \\ W(Y) &= e^{-\tau_{\text{ins}} E_{i_k}} \left\langle i_k \left| \hat{b}^\dagger_{l\sigma} \hat{b}_{j\sigma} \right| \tilde{i}_k \right\rangle e^{\tau_{\text{ins}} E_{\tilde{i}_k} - (\tau_{\text{ins}} + d\tau) E_{\tilde{i}_k}} \left\langle \tilde{i}_k \left| \hat{b}_{l\sigma} \right| i_{k+1} \right\rangle e^{(\tau_{\text{ins}} + d\tau) E_{i_{k+1}}}. \end{aligned} \tag{2.186}$$

As we only included the infinitesimal time step $d\tau$ to fix the time ordering of operators in the weights above, we can set it to zero and see that in the relative weight, all exponentials cancel out so that the acceptance probability is given by

$$p_{X\to Y} = min\left(1, \frac{W(Y)}{W(X)} \frac{A_{Y\to X}}{A_{X\to Y}}\right) = min\left(1, \frac{\left\langle i_k \left| \hat{b}^\dagger_{l\sigma} \hat{b}_{j\sigma} \right| \tilde{i}_k \right\rangle \left\langle \tilde{i}_k \left| \hat{b}_{l\sigma} \right| i_{k+1} \right\rangle}{\left\langle i_k \left| \hat{b}_{j\sigma} \right| i_{k+1} \right\rangle} \frac{A_{Y\to X}}{A_{X\to Y}}\right). \tag{2.187}$$

Calling $n_{l\sigma}$ the occupation number on site $l\sigma$ in the state $|i_k\rangle$, this simplifies to

$$p_{X\to Y} = min\left(1, n_{l\sigma} \frac{A_{Y\to X}}{A_{X\to Y}}\right), \tag{2.188}$$

where we still have to specify the proposal probability functions A. Suppose that in a given state X, we propose with probability p_{insk} to insert an interaction. We then

uniformly draw one of the neighboring sites, of which there are, in a hypercubic lattice, $z_{\text{coord}} = 2d$ in total. Furthermore, we have to specify in which time direction we want to go after the kink was inserted. Putting all this together, we get for the proposal probability $A_{X\to Y}$

$$A_{X\to Y} = \frac{p_{\text{insk}}}{2z_{\text{coord}}}. \tag{2.189}$$

The inverse step $Y \to X$ corresponds to a worm head that stops at an interaction that happens on the same site and layer, see step **(3)** in the summary of the move update in the previous section. It is then proposed with probability p_{del} to actually follow the interaction and thereby deleting it. So we simply have

$$A_{Y\to X} = p_{\text{del}}. \tag{2.190}$$

Hence the acceptance probability of inserting a kink finally becomes

$$p_{X\to Y} = min\left(1, 2n_{l\sigma}z_{\text{coord}}\frac{p_{\text{del}}}{p_{\text{insk}}}\right). \tag{2.191}$$

In [55], two other consistent schemes are described to update between the state of no interaction on site j at τ_{int} and the states where an interaction happens on j at τ_{int}, but each time to a different adjacent site.

Deletion of an interaction

In order for our algorithm to be balanced, we need to include the inverse process of the insertion of an interaction, namely its deletion. This corresponds to exactly the inverse process shown in figure 2.19: the worm head $\hat{b}_{l\sigma}$ halts at an interaction $\hat{b}^{\dagger}_{l\sigma}\hat{b}_{j\sigma}$ and can either stay on site $l\sigma$ and proceed in imaginary time or it can follow the interaction and hop to site $j\sigma$, effectively deleting the corresponding kink. The weights and proposal functions can be obtained by simply interchanging X and Y from the insertion update. The acceptance ratio is thus just the inverse of equation (2.191),

$$p_{X\to Y} = min\left(1, \frac{1}{2n_{l\sigma}z_{\text{coord}}}\frac{p_{\text{insk}}}{p_{\text{del}}}\right). \tag{2.192}$$

Insertion and removal of an open worm

We still have to discuss how to go from closed worldline configurations out of the partition function Z to open configurations from the Green function sector Z_e and

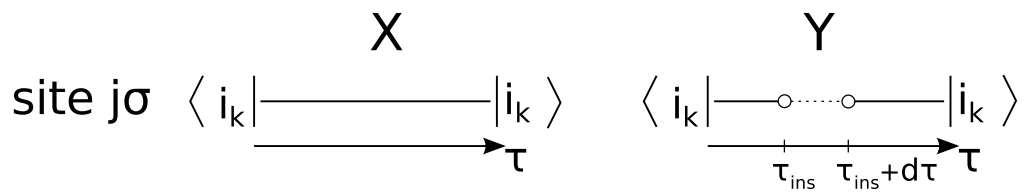

Figure 2.20: Pictorial representation of a worm insertion/removal. For insertion $X \to Y$, a random site $j\sigma$ and a random time τ_{ins} are drawn and a worm pair is inserted. A removal $Y \to X$ is only possible if the worm head hits the worm tail. We again consider the case of a worm head (right circle) $\hat{b}_{j\sigma}$ moving in positive imaginary time direction.

back. This is achieved by the insertion and removal of a worm pair, see figure 2.20.

As in the previous examples, we consider the case of a worm head $\hat{b}_{j\sigma}$ moving in positive imaginary time direction. Since we have the freedom to choose the value of the worm matrix element [55], we are allowed to set the weight ratio to some constant number C,

$$\frac{W(Y)}{W(X)} = C. \tag{2.193}$$

For insertion, we uniformly draw one of the $N_{\text{sites}} = 3L^2$ sites (keep in mind that the z-coordinate corresponds to the spin index σ) and an insertion time τ_{ins} between 0 and β. Furthermore, we choose with probability $1/2$ to go in positive or negative imaginary time direction. At last, we have to specify if we insert a creation or an annihilation worm, i.e. if the particle number between the worm ends is increased or decreased by 1, respectively. This choice is also made with probability $1/2$ for both cases. Putting all this together, we get for the proposal probability to insert an annihilation (creation) worm on $i\sigma$ at τ_{ins} that moves in a specific time direction

$$A_{X\to Y} = \frac{1}{2}\frac{1}{2}\frac{1}{\beta N_{\text{sites}}} p_{\text{insw}}, \tag{2.194}$$

where p_{insw} is the probability to acctually propose the insertion of a worm pair.

If, inversely, we are in an open worm configuration, we can freely determine a probability p_{glue} to propose the agglutination of both worm ends. Thus we write

$$A_{Y\to X} = p_{\text{glue}}. \tag{2.195}$$

The acceptance ratio for inserting a worm pair is then given by

$$p_{X\to Y} = min\left(1, \frac{W(Y)}{W(X)}\frac{A_{Y\to X}}{A_{X\to Y}}\right) = min\left(1, C\cdot 4\beta N_{\text{sites}}\frac{p_{\text{glue}}}{p_{\text{insw}}}\right), \tag{2.196}$$

whereas the acceptance ratio to glue the worm ends is again just the inverse,

$$p_{Y\to X} = min\left(1, \frac{W(X)}{W(Y)}\frac{A_{X\to Y}}{A_{Y\to X}}\right) = min\left(1, \frac{1}{C\cdot 4\beta N_{\text{sites}}}\frac{p_{\text{insw}}}{p_{\text{glue}}}\right). \tag{2.197}$$

One could, for example, choose $C = p_{\text{insw}}/\left(4\beta N_{\text{sites}} p_{\text{glue}}\right)$. This way, one would accept every insertion and removal update. However, if the insertion of a worm pair is rejected, the algorithm simply draws a new site and time and tries anew to insert a worm pair. Since this is far from being performance critical, we do not loose much if the acceptance probability for worm insertion is less than 1. In contrast, we should always ensure that the acceptance probability of glueing the ends of a worm is always equal to 1.

2.4.5.2 The trilayer system and ergodicity

In this section, we describe problems that occured concerning ergodicity using the worm algorithm with a single worm and the updating procedures described above to simulate the trilayer system given by the Hamiltonian in equation (2.28).

Pursuant to section 2.4.3.3, each spin distribution should be sampled according to its Boltzmann weight in a reasonable amount of computation time. However, using the worm algorithm with a single worm for the trilayer Hamiltonian (2.28) with the updates described above, we observed anomalously large autocorrelation times $\tau_{\vec{F}^2}$ of the (approximated) on-site magnetic moment $\vec{F}^2$ given in equation (2.30), so that the system was essentially frozen in a more or less random spin state, highly dependent on the initial state and the used sequence of random numbers. The configuration space was therefore obviously not sampled in an ergodic way. The reason for this is the absence of a direct Monte Carlo update which is capable to change the the on-site spin distribution.

To get a precise understanding of the problem, let us consider a concrete example: we go into the Mott limit, $\frac{t}{U_0} \to 0$, and tune μ such that we measure the density $n_i = \langle \hat{n}_i \rangle = 2$ on each site. We choose $U_2 > 0, U_2 \ll U_0$, i.e. we are in the antiferro-

$\lvert n_{i+}\ n_{i0}\ n_{i-}\rangle$	$\vec{F}^2$
$\lvert 200\rangle, \lvert 002\rangle, \lvert 110\rangle, \lvert 011\rangle$	6
$\lvert 020\rangle$	4
$\lvert 101\rangle$	2

Table 2.1: 'Trilayer' local magnetic moment $\vec{F}^2$ as defined in equation (2.30) for every possible two-particle Fock state.

magnetic regime, where we expect that the spin interaction term

$$\frac{U_2}{2}\sum_{i=1}^{N_{\text{sites}}}\left(\hat{\vec{F}}_i^2 - 2\hat{n}_i\right) = \\ = \frac{U_2}{2}\sum_{i=1}^{N_{\text{sites}}}\left(\hat{n}_{i+}^2 - 2\hat{n}_{i+}\hat{n}_{i-} + \hat{n}_{i-}^2 - \hat{n}_{i+} - \hat{n}_{i-} + 2\hat{n}_{i0}\hat{n}_{i+} + 2\hat{n}_{i0}\hat{n}_{i-}\right), \tag{2.198}$$

is minimized, which is realized by minimizing each local magnetic moment $\vec{F}_i^2 = \left\langle \hat{\vec{F}}_i^2 \right\rangle$ separately under the condition that $n_i = 2$ on each site. Only a few Fock states are possible, see table 2.1.

Now let us see what the worm algorithm does in the considered example. We usually start from the empty lattice state where all $n_{i\sigma} = 0$ and wait for thermalization. In the very first step, a creation worm is inserted at a random site $i\sigma$. In the no-hopping limit, we can be sure that it will never hop to any other site, thus it is only propagating in imaginary time. The worm performs one (or more) time steps, wraps around imaginary time dimension and finally bites in its own tail, which results in the creation of a particle on site $i\sigma$. Then the next insertion site is drawn and the same procedure happens again until there are two particles inserted on each (physical) site $i = \cup_\sigma i\sigma$, where the spin layers σ mainly depend on the sequence of random numbers. Inserting a third particle on a single (physical) site i is energetically very costly (as well as removing one to have only one particle on site i) in the considered regime of large U_0 and is therefore very unlikely to happen, especially for low temperatures. Hence we end up at a state where $n_i = \sum_\sigma n_{i\sigma} = 2$ on all (physical) sites i, but with a random on-site spin distribution. Moreover, this spin distribution is now frozen: the only way to change it is to remove a particle on site i with spin σ and to reinsert one with a different spin $\sigma' \neq \sigma$ on the same site i. Such a process is very improbable to happen. We either have to pass an intermediate state with $n_i = 1$ or $n_i = 3$, which are

both exponentially suppressed due to their relative weight

$$\frac{W(n_i = 3, 1)}{W(n_i = 2)} \approx \exp\left(-\beta \frac{U_0}{2}\right) \approx 0, \tag{2.199}$$

where we only considered the dominant on-site repulsion term in U_0 in the no-hopping limit. Even worse, if we want to go from the state with the second lowest local magnetic moment $|n_{i+}, n_{i0}, n_{i-}\rangle = |020\rangle$ to the one with the lowest, $|101\rangle$, we have to pass at least three such intermediate states (for example by going through the states $|020\rangle \to |010\rangle \to |011\rangle \to |001\rangle \to |101\rangle$).

This problem was not only observed in the Mott limit $\frac{t}{U_0} \to 0$. It even extended to the superfluid phase far from the Mott-to-superfluid phase boundary, where site occupation number fluctuations are high.

2.4.5.3 Solution to the ergodicity problem

The only possibility to avoid the described problem in a single worm algorithm is to introduce one or more Monte Carlo updates that are able to change the on-site spin distribution without detour to states with different total on-site particle number n_i. We engineered two new kinds of updates, both working exclusively in the partition function sector, where only closed worldlines are present.

The cutandpaste update

The *cutandpaste update* cuts, as the name suggests, closed worldlines out of the current, closed worldline configuration and reinserts them in a random fashion to the different spin layers, see figure 2.21.

The goal of the update is to propose a new on-site spin configuration without the need of intermediate steps with different particle number n_i as described above. To this end, we draw a random site i where we want to change the distribution of spin species (n_{i+}, n_{i0}, n_{i-}) at imaginary time $\tau = 0$. All the particle worldlines we cut are crossing the spacetime point $i, \tau = 0$, see figure 2.21. Unfortunately, since particles can hop to their neighboring sites, the cutandpaste update is not capable to change the spin distribution on site i alone. In order to maximize the Metropolis acceptance ratio (2.152) of the proposed step, we yet have to try to find worldlines that 'lie on top of each other' as much as possible, meaning the more the particles are on the same site at the same time, the higher will be the acceptance ratio of the proposed step.

We have to keep in mind the fact that the worldlines we cut are not uniquely defined only by choosing the single point $i, \tau = 0$ they have to cross. See for example the spin 0 layer on the left side of figure 2.21: we can either take the first or the second

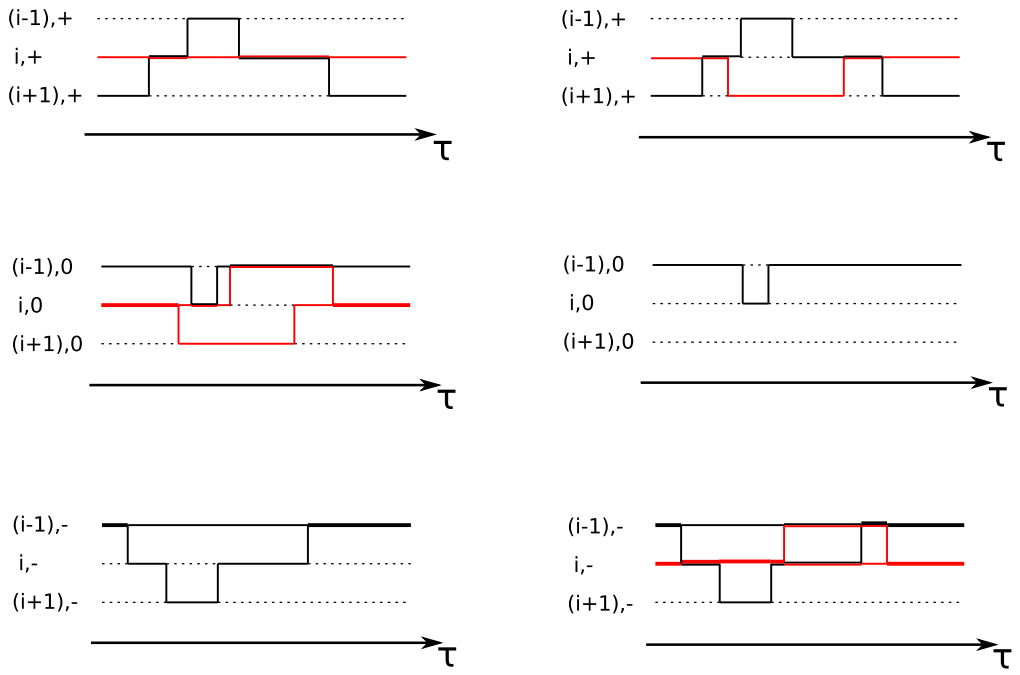

Figure 2.21: Spin configurations on sites $i-1, i, i+1$ before (left) and after the cutandpaste update. Cut-and-pasted worldlines are colored red. We start at $\tau = 0$ on site i and cut out worldlines in all layers that cross that spacetime point. The choice of worldlines is not yet unique: at some interactions, we can make the choice either to stay on the current site or to follow the interaction. We decide that with the following rule: Follow the interaction if **(1)** the distance to the start site i is shortened or **(2)** if the particle number on the current site drops to zero after the interaction.

interaction from site $i, 0$ to site $(i-1), 0$. As we preferably want to change the spin configuration on site i, we choose the worldlines we cut using the following rules:

Cutting rules in the cutandpaste update:

(1) We always cut only one closed loop (worldline) with minimal particle number at a time. It may be possible that a worldline winds more than one time around imaginary dimension before it comes back again to the point $i, \tau = 0$. Such a worldline has a particle number > 1, but can not be further split up and has to be cutted as a whole.

(2) Go on in imaginary time on the current site till the next interaction is reached that leaves the site.

(3) Only follow an interaction if the distance to the starting site i is reduced. This makes sure that we only cut worldlines on site i and its neighborhood. As we are on a $2d$-lattice, the distance h of two sites i and j is given by the 1-norm, $h = |i_x - j_x| + \left|i_y - j_y\right|$. If h does not decrease, stay on the current site and proceed in imaginary time.

(4) If the particle number after an encountered interaction drops to zero, we are forced to follow the interaction.

(5) If we hit the starting point $i, \tau = 0$ again, we have found a closed worldline.

Next, we paste all cutted closed loops such that they again intersect the point $i, \tau = 0$, but this time randomly distributed among the different spin layers. Care has to be taken to set all particle numbers right.

In contrast to the worm updates described above, the cutandpaste update is nonlocal. The computation of the Metropolis update ratio is thus more costly. The dulliest way to compute it would be to calculate both the weight $W(X)$ before and $W(Y)$ after the update completely. To do so, we would have to compute all interaction matrix elements and all diagonal energies at all times in the system. Since the number of interactions scales with βL^2, this would be highly inefficient, especially for large system sizes. But again, most of the factors cancel when we compute the weight ratio $W(Y)/W(X)$, namely those that do not change under the cutandpaste process.

We thus only keep track of the sites where the spin configuration changes during the update. Only there, we compute the diagonal energies E_{i_k} and the matrix elements $\langle i_k|\hat{H}_1|i_{k+1}\rangle$ in both the original and proposed configurations X and Y.

The weight ratio can formally be written as

$$\frac{W(Y)}{W(X)} = \prod_j \prod_{k_j} \frac{\langle i^Y_{k_{j-1}}|\hat{H}_1|i^Y_{k_j}\rangle}{\langle i^X_{k_{j-1}}|\hat{H}_1|i^X_{k_j}\rangle} \exp\left(-\Delta\tau_{k_j}\Delta E_{k_j}\right), \tag{2.200}$$

where $\Delta\tau_{k_j} = \tau_{k_j} - \tau_{k_j-1}$ is the period of time where the difference in diagonal energies on site j is $\Delta E_{k_j} = E^Y_{k_j} - E^X_{k_j}$. The index j runs over all sites involved in the cutandpaste process and k_j labels the interactions happening on site j.

As we do not use a priori probabilities for simplicity, the Metropolis acceptance probability for the proposed step is

$$p_{X\to Y} = min\left(1, \frac{W(Y)}{W(X)}\right). \tag{2.201}$$

As one can imagine, the efficiency (i.e. the average acceptance ratio) of the cutandpaste update is highly dependent on how closely the cutted worldlines lie on top of each other, i.e. the corresponding particles have to share the same site as long as possible. As for small t/U_0, hoppings of particles are rare and many worldlines only reside on a single site, see e.g. the red worldline in the spin up layer in the left column of figure 2.21. If all cutted worldlines are of that kind, they perfectly lie on top of each other. Hence, the cutandpaste update is fairly efficient in the regime $U_0 \gg t$. In contrast, for large t/U_0 and high inverse temperature β, it becomes unprobable to find worldlines that mainly stay on only a single site. Cutting out worldlines on a whole cluster of neighboring sites simultaneously increases the acceptance ratio a little bit. However, in the superfluid phase where t/U_0 is of order 1, the update becomes badly inefficient: we observe acceptance ratios of only about 10^{-4}. Fortunately, changes in spin state by the ordinary worm type updates occur much more often there because the difference in energy for different site occupation numbers n_i becomes smaller, cf. section 2.4.5.2.

Furthermore, we implemented a second kind of closed configuration update called layerswap which shows decent acceptance ratios in both regimes.

The layerswap update

As the name *layerswap* indicates, this update proposes a new distribution of the present spin layers, see figure 2.22. We thus are able to potentially change the spin of all particles at once. This kind of update shows quite high Metropolis acceptance but, however, there is a drawback: with this update, we cannot perform transitions like $|n_{i+}, n_{i0}, n_{i-}\rangle = |n, 0, n\rangle \to |0, 2n, 0\rangle$, which unfortunately happen to be the two energetically lowest spin states for even densities in the antiferromagnetic regime. It mainly lifts the sign symmetry of spins since the exchange of spin up with spin down is always accepted with probability 1.

Concerning the weight ratio $W(Y)/W(X)$, we can be sure that all hopping matrix elements $\langle i_k|\hat{H}_1|i_{k+1}\rangle$ cancel out exactly. We thus only have to worry about the diagonal energies, where again only the spin interaction term can be different. Hence we can write the weight ratio as

$$\frac{W(Y)}{W(X)} = \prod_j \prod_{k_j} \exp\left(-\Delta\tau_{k_j}\Delta E_{k_j}\right), \tag{2.202}$$

where $\Delta\tau_{k_j} = \tau_{k_j} - \tau_{k_j-1}$ is the period of time where the difference in diagonal energies on site j is $\Delta E_{k_j} = E^Y_{k_j} - E^X_{k_j}$. The index j runs over all (physical) sites of the system and k_j labels the time intervals with different diagonal energies on site j.

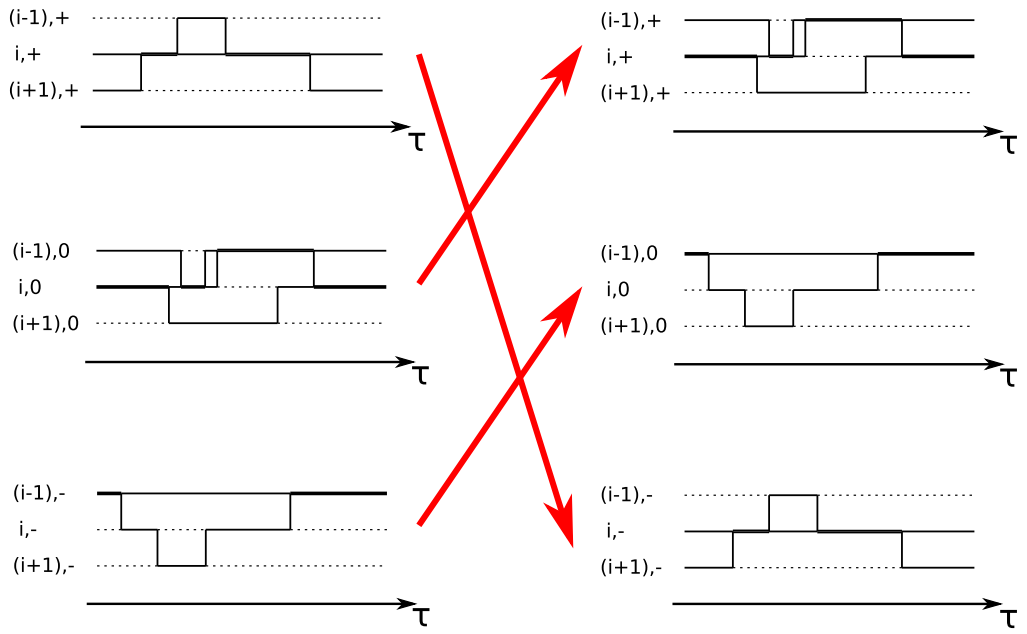

Figure 2.22: Configurations on the sites $i-1, i, i+1$ before (left) and after the layer-swap update. We exchange the layers as a whole: in the shown process, each spin up particle turns into spin down, spin zero into spin up and spin down into spin zero.

We do not use a priori probabilities on the redistribution of layers, so we once again get the acceptance probability

$$p_{X\to Y} = min\left(1, \frac{W(Y)}{W(X)}\right). \tag{2.203}$$

Again, we emphasize that the worm updates plus the layerswap update alone do not lead to ergodicity: the layerswap process rather helps in avoiding problems occuring due to the $\mathbb{Z}_2$-symmetry of spin states.

2.5 Error estimation and autocorrelation time

A major aspect of any Monte-Carlo method is the proper estimation of statistical errors. We first consider the case of uncorrelated data and derive the central limit theorem. Then, we have a look at correlated data and explain the concept of a binning analysis to obtain reliable errorbars for correlated data sets.

2.5.1 Uncorrelated data

Suppose that in our Monte-Carlo simulation, we have M uncorrelated measurements of an observable A and we want to estimate how well the sample mean

$$\bar{A} = \frac{1}{M} \sum_{i=1}^{M} A_i$$

fits to the true expectation value $\langle A \rangle$. The statistical error Δ_A^2 is given by the root-mean-square deviation of the sample mean $\bar{A}$ from the true expectation value $\langle A \rangle$ [56],

$$\Delta_A^2 = \left\langle \left(\bar{A}^2 - \langle A \rangle \right)^2 \right\rangle = \left\langle \bar{A}^2 \right\rangle - \langle A \rangle^2 . \tag{2.204}$$

We can rewrite $\left\langle \bar{A}^2 \right\rangle$ as

$$\begin{aligned} \left\langle \bar{A}^2 \right\rangle &= \left\langle \left(\frac{1}{M} \sum_{i=1}^{M} A_i \right)^2 \right\rangle \\ &= \frac{1}{M^2} \sum_{i,j=1}^{M} \left\langle A_i A_j \right\rangle \\ &= \frac{1}{M^2} \sum_{i=1}^{M} \left\langle A_i^2 \right\rangle + \frac{M-1}{M} \langle A \rangle^2 \\ &= \frac{1}{M} \left\langle A^2 \right\rangle + \frac{M-1}{M} \langle A \rangle^2 , \end{aligned} \tag{2.205}$$

where we used the fact that for independent samples i, j, the expectation value factorizes as

$$\left\langle A_i A_j \right\rangle = \langle A_i \rangle \left\langle A_j \right\rangle = \langle A \rangle^2 . \tag{2.206}$$

We replace $\left\langle \bar{A}^2 \right\rangle$ in equation (2.204) to get

$$\Delta_A^2 = \frac{1}{M} \left(\left\langle A^2 \right\rangle - \langle A \rangle^2 \right) = \frac{\sigma_A^2}{M}. \tag{2.207}$$

We see that the error Δ_A for uncorrelated data goes with $1/\sqrt{M}$, which is the heart of the central limit theorem.

Usually, we do not know the underlying true variance σ_A^2 of the observable A.

However, calling

$$\overline{A^2} = \frac{1}{M}\sum_{i=1}^{M} A_i^2, \tag{2.208}$$

we can connect the sample variance $\overline{A^2} - \overline{A}^2$ to the true variance σ_A^2 via

$$\left\langle \overline{A^2} - \overline{A}^2 \right\rangle = \frac{M-1}{M}\sigma_A^2, \tag{2.209}$$

where we have made use of equation (2.205). The statistical error Δ_A can thus be rewritten as

$$\Delta_A \approx \sqrt{\frac{\overline{A^2} - \overline{A}^2}{M-1}}, \tag{2.210}$$

where the '≈' symbol accomodates for the fact that the sample variance we measure does not in general equal its expectation value.

2.5.2 Correlated data

For correlated data, the independence condition in equation (2.206) does no longer hold. The statistical error estimate is therefore

$$\begin{aligned}
\Delta_A^2 &= \frac{1}{M^2}\sum_{i,j=1}^{M}\left\langle A_i A_j\right\rangle - \langle A\rangle^2 = \frac{\mathrm{Var}(A)}{M} + \frac{1}{M^2}\sum_{i\neq j=1}^{M}\left(\left\langle A_i A_j\right\rangle - \langle A\rangle^2\right) \\
&= \frac{\mathrm{Var}(A)}{M} + \frac{2}{M^2}\sum_{i>j=1}^{M}\left(\left\langle A_i A_j\right\rangle - \langle A\rangle^2\right) \\
&= \frac{\mathrm{Var}(A)}{M} + \frac{2}{M^2}\sum_{t=1}^{M-1}(M-t)\left(\langle A_1 A_{1+t}\rangle - \langle A\rangle^2\right) \\
&= \frac{\mathrm{Var}(A)}{M}\left(1 + 2\sum_{t=1}^{M-1}\left(1 - \frac{t}{M}\right)\phi_A^t\right),
\end{aligned} \tag{2.211}$$

where we introduced the autocorrelation function ϕ_A^t [57]

$$\phi_A^t = \frac{\langle A_1 A_{1+t}\rangle - \langle A\rangle^2}{\mathrm{Var}(A)}. \tag{2.212}$$

For large M, the error Δ_A^2 may be rewritten as

$$\Delta_A^2 = \frac{\mathrm{Var}(A)}{M}\left(1 + 2\sum_{t=1}^{M-1}\phi_A^t\right) = \frac{\mathrm{Var}(A)}{M}\left(1 + 2\tau_A\right), \tag{2.213}$$

where we defined the autocorrelation time

$$\tau_A = \sum_{t=1}^{\infty}\phi_A^t. \tag{2.214}$$

The autocorrelation time τ_A plays an important role in the production of uncorrelated data points out of a correlated data set: If we pick out n data points from our set of size M that are $2\tau_A$ apart, they can be considered to be uncorrelated [58].

However, estimating the autocorrelation time τ_A via the autocorrelation function ϕ_A^t can be very costly. In the next section, we describe a fast and comfortable way to estimate the error Δ_A and the corresponding autocorrelation time τ_A.

2.5.3 Binning analysis

The binning analysis [56] is a simple method to estimate both the error Δ_A and the autocorrelation time τ_A of a set of correlated Monte-Carlo data.

It goes as follows: Of the original data $A_i^{(0)} = A_i$, we repetitively create a new, shorter data set by taking the mean of two successive data points,

$$A_i^{(l)} = \frac{1}{2}\left(A_{2i-1}^{(l-1)} + A_{2i}^{(l)}\right). \tag{2.215}$$

Whilst the total mean value $\overline{A^{(l)}} = \overline{A}$ stays unchanged in each step l, the data points become less and less correlated. At each iteration, we pretend that we already have uncorrelated data and compute the error using equation (2.210)

$$\Delta_A^{(l)} = \sqrt{\frac{1}{M(M-1)}\sum_{i=1}^{M_l}\left(A^{(l)i} - \overline{A}\right)^2}, \tag{2.216}$$

being well aware of the fact that we systematically underestimate the error in each step due to the correlation of data points. However, as the data points get more and more uncorrelated in each step, we should reach a limit for $l \to \infty$

$$\Delta_A = \lim_{l\to\infty}\Delta_A^{(l)}, \tag{2.217}$$

which is exactly the error if our data points would be completely uncorrelated. An

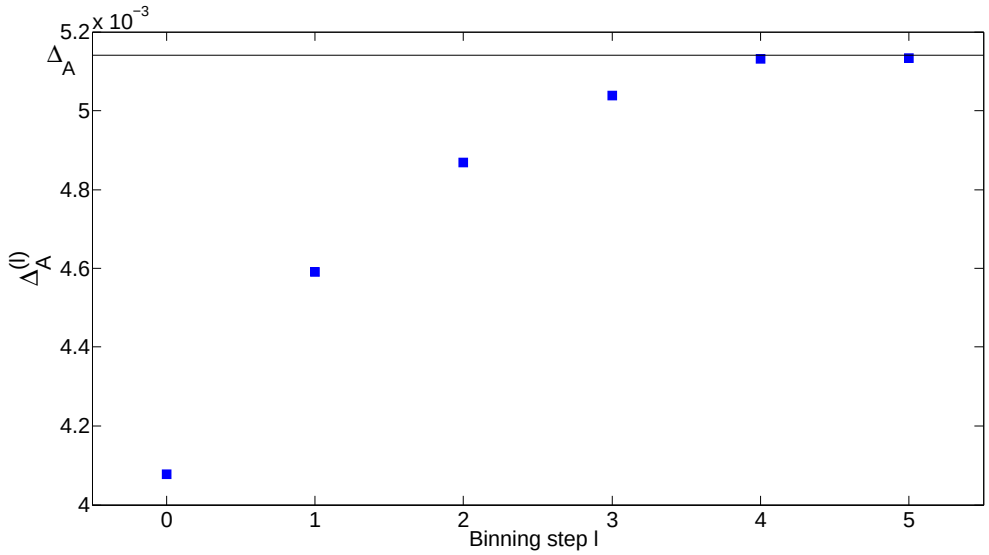

Figure 2.23: Example of a binning analysis of some correlated data. We see the uncorrelated error estimate $\Delta_A^{(l)}$ from equation (2.216) plotted versus the binning step l. It can be nicely observed how the limit Δ_A is attained.

example of how this limit is reached is plotted in figure 2.23. One should stop the binning analysis if the size M_l of the current data set is around 50. For smaller data sets, the error estimations $\Delta_A^{(l)}$ become unprecise. From equation (2.213), we can extract the autocorrelation time τ_A as

$$\tau_A = \frac{1}{2}\left(\frac{M\Delta_A^2}{\mathrm{Var}(A)} - 1\right), \tag{2.218}$$

where $\mathrm{Var}(A) = \overline{A^2} - \overline{A}^2$ is the usual sample variance of the data A_i.

There exist some more sophisticated methods of error estimation in correlated data sets such as the jackknife procedure [59] and the bootstrap method [60], which are not discussed here.

CHAPTER 3

RESULTS

In this chapter, we present the results we obtained for the trilayer system using the worm algorithm Quantum Monte Carlo simulation. We discuss the cases of ferromagnetic and antiferromagnetic interactions in two separate sections.

As we have seen in section 2.4.5, the worm algorithm not only correctly samples the partition function Z, but also the Green's function G given in equation (2.171). Regrettably, as our simulation only uses a single worm, we are merely able to sample the single-particle Green's function $G_\sigma(i, j, \tau, \tau_0)$. However, important spin quantities, starting with the spin projections onto the x- and y-axis, F_x and F_y, contain terms like $\hat{b}_{i_A\sigma_A}\hat{b}^\dagger_{j_A\sigma'_A}\hat{b}_{i_B\sigma_B}\hat{b}^\dagger_{j_B\sigma'_B}$, which can only be estimated by a sampling of the corresponding four-point Green's function. Hence, the computation of crucial observables such as the equal time spin-spin correlation function

$$F_{\alpha\alpha}(\vec{R}) = \frac{1}{L^2}\sum_{\vec{r}}\langle\hat{F}_{\alpha,\vec{r}}\hat{F}_{\alpha,\vec{r}+\vec{R}}\rangle \qquad \alpha = x, y, z, \tag{3.1}$$

the global magnetization [22]

$$F^2_{\text{tot}} = L^2\sum_{\alpha,\vec{R}} F_{\alpha\alpha}(\vec{R}) \tag{3.2}$$

and the magnetic structure factor

$$S(\vec{k}) = \frac{1}{L^2}\sum_{\alpha,\vec{R}} e^{i\vec{k}\cdot\vec{R}}F_{\alpha\alpha}(\vec{R}) \tag{3.3}$$

are out of range of our simulation. As stated earlier, for the total magnetic moment

$\langle\vec{\hat{F}}^2\rangle = \frac{1}{L^2}\sum_i\langle\vec{\hat{F}}_i^2\rangle$, we can only give the approximate value given in (2.30). This theoretically allows us to determine the associated approximate value of the zz-component of the nematic order tensor given in equation (2.29),

$$Q_{zz} = \langle\hat{F}_z^2 - \frac{1}{3}\vec{\hat{F}}^2\rangle. \tag{3.4}$$

To find magnetic transitions, we consider $\langle\hat{F}_z^2\rangle$ and $\langle\vec{\hat{F}}^2\rangle$ as order parameters, where the operators $\hat{F}_z^2$ and $\vec{\hat{F}}^2$ are both diagonal in spin occupation number basis $|n_{i+}, n_{i0}, n_{i-}\rangle$.

On the other hand, order parameters for the Mott to superfluid phase transition are fluctuations in total particle number $\sim \langle N^2\rangle - \langle N\rangle^2$ and the winding number squared $\langle w^2\rangle$, to which we have access without any restriction.

Also, the diagonal energies E_{pot} and E_{spin} can simply be estimated by their sample means of the simulated diagonal configurations at imaginary time $\tau = 0$,

$$\langle\hat{E}_{\text{pot}}\rangle = \frac{1}{M}\sum_{k=1}^{M}\hat{E}_{\text{pot}}^k, \qquad \langle\hat{E}_{\text{spin}}\rangle = \frac{1}{M}\sum_{k=1}^{M}\hat{E}_{\text{spin}}^k, \tag{3.5}$$

where $\hat{E}_{\text{pot}}^k, \hat{E}_{\text{spin}}^k$ are given by

$$\hat{E}_{\text{pot}}^k = \frac{U_0}{2}\sum_{i=1}^{N_s}\hat{n}_i^k(\hat{n}_i^k - 1), \qquad \hat{E}_{\text{spin}} = \frac{U_2}{2}\sum_{i=1}^{N_s}\left(\vec{\hat{F}}_i^k\right)^2 - 2\hat{n}_i^k \tag{3.6}$$

with the index k labeling the simulated diagonal configuration, N_s the number of lattice sites and $\vec{\hat{F}}_i^2$ the approximated local magnetic moment on site i.

The kinetic energy

$$\langle\hat{E}_{\text{kin}}\rangle = -t\sum_{\langle i,j\rangle,\sigma}\langle\hat{b}_{i,\sigma}^\dagger\hat{b}_{j,\sigma} + \hat{b}_{j,\sigma}^\dagger\hat{b}_{i,\sigma}\rangle \tag{3.7}$$

is a bit more subtle to obtain. We can estimate it either using the sampling of the one-body Green's function G given in equation (2.171), or we can make use of the fact that it is given by

$$\langle\hat{E}_{\text{kin}}\rangle = \frac{\text{Tr}\left[e^{-\beta\hat{H}}\hat{E}_{\text{kin}}\right]}{\text{Tr}\left[e^{-\beta\hat{H}}\right]} = \frac{-\frac{t}{\beta}\partial_t\text{Tr}\left[e^{-\beta\hat{H}}\right]}{\text{Tr}\left[e^{-\beta\hat{H}}\right]} = -\frac{t}{\beta}\frac{1}{M}\sum_{k=1}^{M}n_k, \tag{3.8}$$

where n_k is the expansion order of the simulated diagonal configuration, i.e. the number of particle hoppings, see equation (2.169).

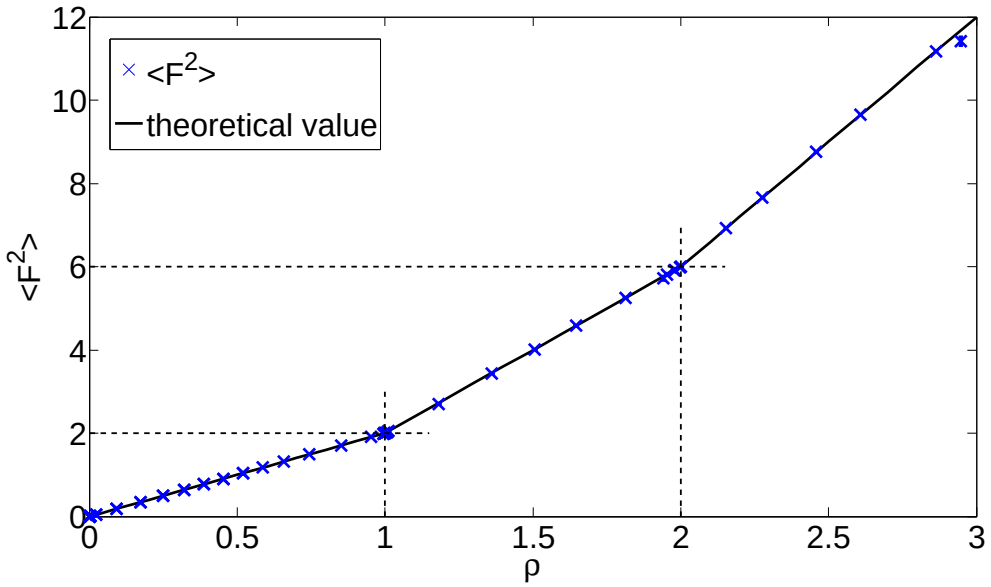

Figure 3.1: The average approximated local magnetic moment $\langle \vec{\hat{F}}^2 \rangle$ plotted versus the average density ρ for $L = 8, \beta = 8, U_0 = 100, U_2 = -0.1U_0$. As one can see, $\langle \vec{\hat{F}}^2 \rangle$ is equal to its maximal possible value indicated by the black line.

3.1 The ferromagnetic case

We start the presentation of our Monte Carlo results with the case of ferromagnetic interactions, $U_2 < 0$. The mean field analysis of section 2.3.2 as well as previous work [42, 22, 61] on the full spin-1 model suggests that the system shows saturated ferromagnetism in the whole μ/U_0 - t/U_0-plane. This is exactly what we obtain in our simulation, as can be seen in figure 3.1, where the average local magnetic moment $\langle \vec{\hat{F}}^2 \rangle = \sum_{i=1}^{N_s} \langle \vec{\hat{F}}_i^2 \rangle$ is plotted versus the total average density $\langle \rho \rangle = \sum_\sigma \langle \rho_\sigma \rangle$. For strong interactions, $\langle \vec{\hat{F}}^2 \rangle$ always equals its maximal possible value, which is given by linear segments: if interactions are high, the energy of the system is minimized if we have a fraction of $(\rho - \lfloor \rho \rfloor)$ sites with $\lfloor \rho \rfloor + 1$ and a fraction of $1 - (\rho - \lfloor \rho \rfloor)$ sites with $\lfloor \rho \rfloor$ particles on it. These sites then contribute with $(\lfloor \rho \rfloor + 1)(\lfloor \rho \rfloor + 2)$ respectively $\lfloor \rho \rfloor (\lfloor \rho \rfloor + 1)$ to the average magnetic moment, so we get

$$\langle \vec{\hat{F}}^2 \rangle = (2\rho - \lfloor \rho \rfloor)(1 + \lfloor \rho \rfloor), \tag{3.9}$$

which is exactly the linear dependence we observe.

Figure 3.2 shows the equal-time two-point Green's functions $G_\sigma(R)$ in the canonical ensemble for $\rho = 1$ and $\rho = 2$, where R is the lattice (1-norm) distance. We

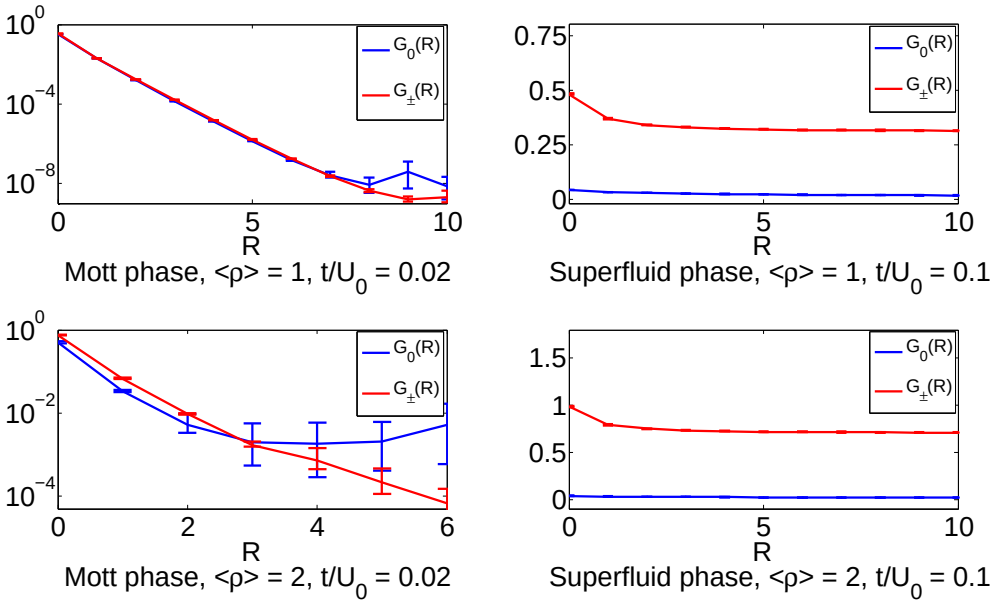

Figure 3.2: Equal time one-particle Green's functions $G_\sigma(R)$ in the ferromagnetic case for different phases in the canonical ensemble, where R is the one-norm distance between sites i and j, $R = |i_x - j_x| + |i_y - j_y|$. We see that the Green's functions are exponentially decaying in the insulating phase (notice the log-scale). In the superfluid phase, the Green's functions assume a finite asymptotical value, which clearly shows long range order.

can clearly observe an exponential decay in the $\rho = 1$ and $\rho = 2$ Mott phases as expected, note the log-scale. In the superfluid phase, however, one can see long-range order, which implies a strong movement of particles. Moreover, it can be seen that we almost exclusively have spin ± 1 particles in the superfluid phase, because $G_\sigma(0)$ is nothing else than the particle density of the spin species σ.

In figure 3.3, the particle density distributions $P(\rho_0), P(\rho_\pm)$ of the different spin particles are shown for distinct Mott and superfluid phases in the canonical ensemble. In the Mott $\rho = 1$ phase 3.3a, the single-site Fock states $|n_{i+}, n_{i0}, n_{i-}\rangle = |1,0,0\rangle$, $|0,1,0\rangle$, $|0,0,1\rangle$ have the same spin interaction energies, hence the distributions $P(\rho_0)$ and $P(\rho_\pm)$ appear quite similar. Since on rare occasions, double occupancies may occur where the on-site Fock states $|2,0,0\rangle$,$|0,0,2\rangle$, $|1,1,0\rangle$, $|0,1,1\rangle$ have the lowest spin interaction energy, we observe a few more $\sigma = \pm 1$ than $\sigma = 0$ particles.

In the $\rho = 1$ superfluid phase 3.3b, double or even higher occupancies are frequent. Moreover, the kinetic energy E_{kin} is high. Since each hopping of a particle contributes to the thermodynamic weight approximately as $\sim \rho_\sigma$ (see equation (2.169)), states with only one single spin species are preferred. Among those, the states $|n_{i+}, 0, 0\rangle$,$|0,0,n_{i-}\rangle$ are energetically cheapest for now very often occuring double or higher occupancies. Hence we almost exclusively observe $\sigma = \pm 1$ particles.

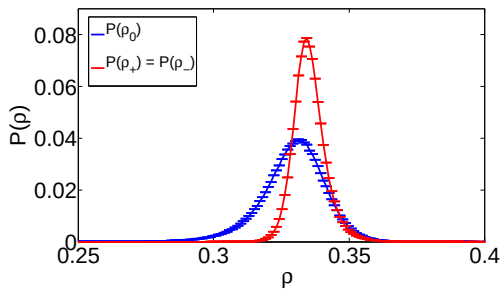

(a) Mott phase, $\rho = 1$, $t/U_0 = 0.02$

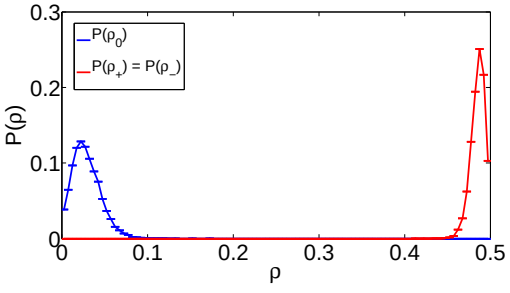

(b) Superfluid phase, $\rho = 1$, $t/U_0 = 0.1$

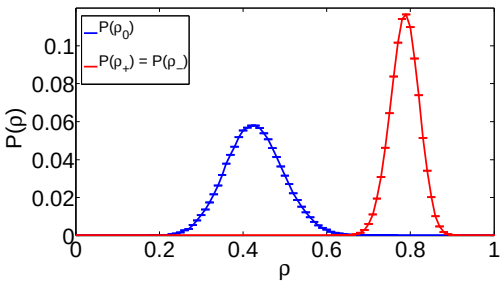

(c) Mott phase, $\rho = 2$, $t/U_0 = 0.02$

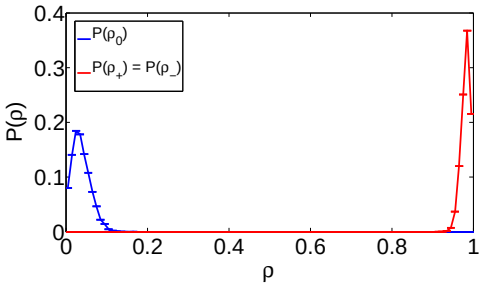

(d) Superfluid phase, $\rho = 2$, $t/U_0 = 0.1$

Figure 3.3: Density distributions for Mott and superfluid phases in the ferromagnetic case $U_2 = -0.1U_0$ with $\beta = 5, L = 10$ in the canonical ensemble for all diagrams. See text for explanations.

In the $\rho = 2$ Mott phase 3.3c, the on-site states $|2,0,0\rangle$,$|0,0,2\rangle$,$|1,1,0\rangle$,$|0,1,1\rangle$ are the states with lowest spin interaction energy. Hence we would expect that $P(\rho_+) = P(\rho_-) \approx 3/4$, $P(\rho_0) \approx 1/2$ at sufficiently low temperatures. However, again due to kinetic energy and higher occupancies, the distribution is shifted towards more $\sigma = \pm 1$ particles.

In the $\rho = 2$ superfluid phase 3.3d, we again observe almost exclusively spin up and down particles. This happens for complete analogous reasons as in the $\rho = 1$ superfluid case. Since on-site spin interaction energies go like $\sim n_i(n_i + 1)$, triple or higher occupancies are consequently more favoured than in the $\rho = 1$ case and the separation of $P(\rho_0)$ and $P(\rho_\pm)$ distributions gets even more pronounced.

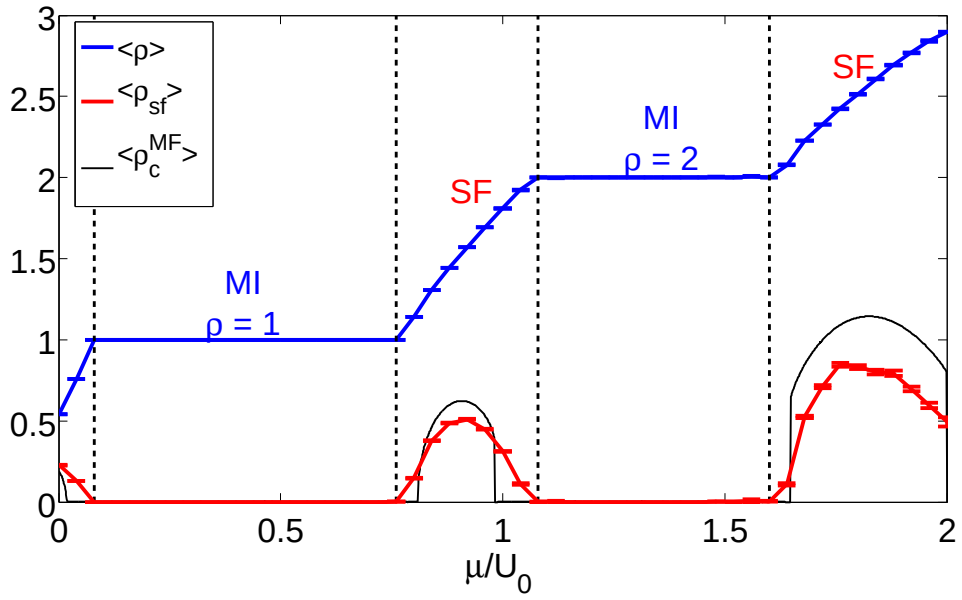

Figure 3.4: Total particle density $\langle\rho\rangle$ and superfluid density $\langle\rho_{sf}\rangle$ as a function of the chemical potential μ/U_0 for $t/U_0 = 0.02$, $L = 10$, $\beta = 5$ in the ferromagnetic case $U_2 = -0.1U_0$. One can clearly observe the first two Mott plateaux, where the total particle density $\langle\rho\rangle$ assumes an integer value and both the compressibility $\kappa = \frac{\partial\langle\rho\rangle}{\partial\mu}$ and the superfluid density ρ_{sf} vanish. All phase transitions are of second order. The solid black line shows the mean-field condensate density $\langle\rho_c^{MF}\rangle$ as a check for the location of phase transitions. However, the mean-field analysis predicts first-order transitions between superfluid phases and the second Mott phase for $\beta = 5$.

3.1.1 Phase transitions

Let us first consider generic phase transitions in the grand canonical ensemble, where we vary the chemical potential μ/U_0 and therefore the total particle number $\langle N\rangle$ of the system. In figure 3.4, we see the total particle density $\langle\rho\rangle = \sum_\sigma\langle\rho_\sigma\rangle$ and the superfluid density $\langle\rho_{sf}\rangle$ as a function of the reduced chemical potential μ/U_0. We observe the common Mott plateaux, where the superfluid density ρ_{sf} as well as the compressibility $\kappa = \frac{\partial\langle\rho\rangle}{\partial\mu}$ vanish and the total density ρ takes on integer values. Although the mean-field solution suggests first order transitions between the superfluid and the second Mott phase at $\beta = 5$ and the given interactions, they appear continuous in the Monte Carlo simulation. However, in the proximity of the tips of the Mott lobes, first order transitions happen.

Figure 3.5 shows the z-component of the local magnetic moment squared, $\langle\hat{F}_z^2\rangle = \frac{1}{L^2}\sum_i\langle(n_{i+} - n_{i-})^2\rangle$ and the winding number squared $\langle w^2\rangle$ which is an order parameter

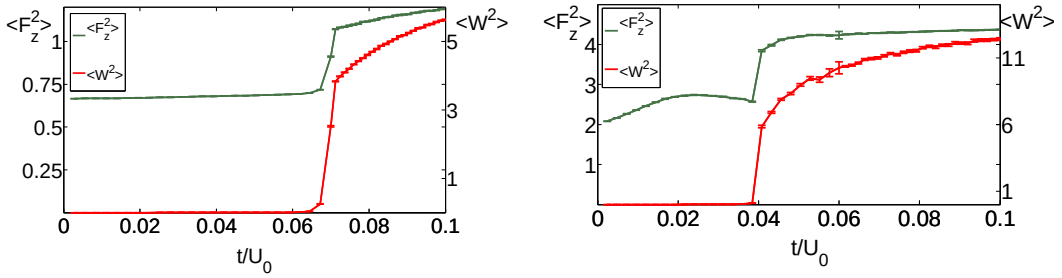

(a) $\rho = 1$ (b) $\rho = 2$

Figure 3.5: Phase transitions crossing the tip of the first 3.5a and second 3.5b Mott lobe for ferromagnetic interactions at fixed densities $\rho = 1$ and $\rho = 2$, respectively. Plotted are $\langle \hat{F}_z^2 \rangle = \frac{1}{L^2} \sum_i \langle (n_{i+} - n_{i-})^2 \rangle$ and the winding number squared $\langle w^2 \rangle$ as an order parameter for the insulating to superfluid transition as a function of t/U_0 for $L = 8, \beta = 4$, $U_2 = -0.1U_0$. For both lobes, the MI-SF transition appears first order.

for the insulator to superfluid transition, as a function of t/U_0 in the canonical ensemble, crossing the tip of the $\rho = 1$ 3.5a and $\rho = 2$ lobe 3.5b. Both Mott to superfluid transitions give the appearance of being first order and seem to happen at the same critical value $(t/U_0)_c$ as the transition in spin configuration measured by $\langle \hat{F}_z^2 \rangle$.

In the Mott limit of the $\rho = 1$ case, the single-site Fock states $|n_{i+}, n_{i0}, n_{i-}\rangle = |1,0,0\rangle, |0,1,0\rangle, |0,0,1\rangle$ are degenerate, hence $\langle \hat{F}_z^2 \rangle = 2/3$. As hoppings of a spin σ particle contribute to the thermodynamic weight with a factor $\sim \langle \rho_\sigma \rangle$, see equation (2.169), the system prefers to be in a state with particles of only one kind of spin σ. Thus, in the ferromagnetic case in the limit of $t/U_0 \to \infty$, the whole system contains either $\sigma = +1$ or $\sigma = -1$ particles. This lift of degeneracy from $|1,0,0\rangle$, $|0,1,0\rangle$,$|0,0,1\rangle$ states in the no-hopping limit to either $|1,0,0\rangle$ or $|0,0,1\rangle$ states on every site of the system is the transition we observe in $\langle \hat{F}_z^2 \rangle$. Since $\langle \hat{F}_{z,i}^2 \rangle = 1$ for a site i occupied with a particle of spin $\sigma = \pm 1$, we measure $\langle \hat{F}_z^2 \rangle \geq 1$, where 1 is only a lower bound because possible of higher occupanices.

For $\rho = 2$, the on-site two-particle states $|n_{i+}, n_{i0}, n_{i-}\rangle = |2,0,0\rangle, |0,0,2\rangle, |1,1,0\rangle$ and $|0,1,1\rangle$ share the same, minimal spin interaction energy in the ferromagnetic case. In the no-hopping limit, we thus get $\langle \hat{F}_z^2 \rangle \approx 2.5$. As in the superfluid limit it is again favoured to have only particles of a single spin species, it is clear that the system will be filled with either only $2L^2$ spin up or spin down particles, hence $\langle \hat{F}_z^2 \rangle \geq 4$, where the equal sign applies if there are exactly 2 particles on each lattice site. Since higher occpancies may occur, this is just a lower boundary.

The magnetic moment $\langle \vec{\hat{F}}^2 \rangle$ always assumes its maximal possible value of $\rho(\rho + 1)$

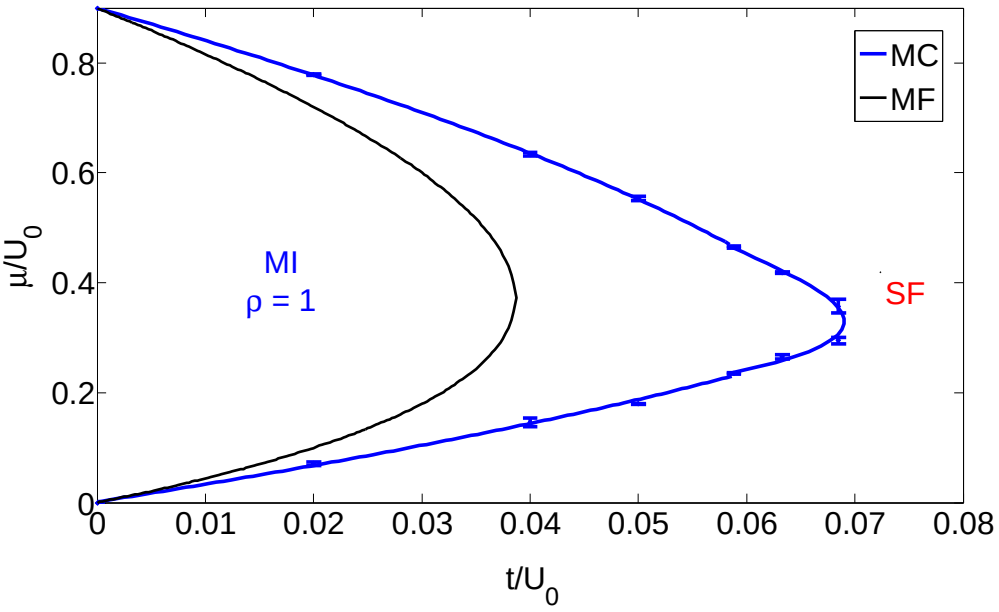

Figure 3.6: Ground state phase boundaries of the first Mott lobe of the trilayer system for the ferromagnetic interaction strength $U_2 = -0.1U_0$. The blue line represents the Monte-Carlo result obtained via finite-size scaling, the black line shows the corresponding mean-field solution we obtained in section 2.3.2.2. As expected, the two lines meet in the no-hopping limit $t/U_0 = 0$, whereas there is a quite big disagreement for the tips of both lobes.

(cf. equation (3.9)) in the Mott phases. For weak interactions, it is slightly larger due higher occupancies. However, there is no sharp phase transition.

3.1.2 Phase diagram

We compute the ground state phase diagram in the thermodynamic limit by a finite-size scaling analysis as described in section 2.2.3. As this is computationally expensive, we content outselves with the computation of only the first Mott lobe, which can be seen in figure 3.6. The blue line shows the Mott to superfluid phase boundary, which is fitted to the data points that are shown with errorbars. The fine black line is the corresponding mean-field result we obtained in section 2.3.2.2. As expected, both results match in the limit of zero hopping $t/U_0 \to 0$. However, the tips of both lobes differ quite much, which was also observed for the full spin-1 system in [22]. Around the tip of the lobe, transitions appear first order for low enough temperatures due to a change in spin configuration, as we have seen in figure 3.5. However, the first

order transitions are blurred out at higher temperatures and finite-size scaling stays possible.

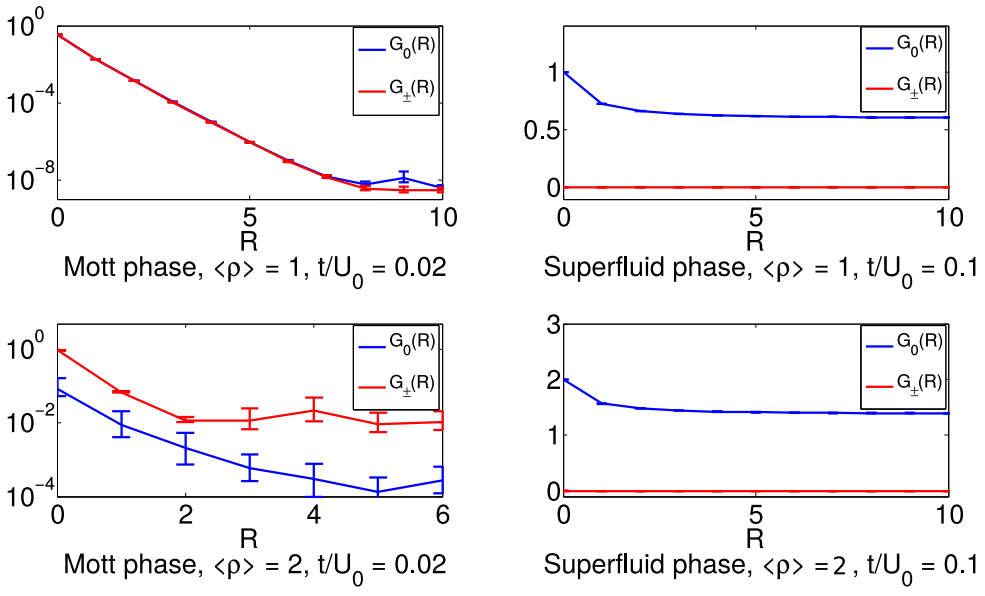

Figure 3.7: Equal time two-point Green's functions $G_\sigma(R)$ for different phases in the antiferromagnetic case, with R again the 1-norm distance. We again observe exponential decay in the Mott phases, whereas there is clear long-range order in the superfluid phase.

3.2 The antiferromagnetic case

In the antiferromagnetic case $U_2 > 0$, the spin interaction energy is minimized by minimizing the approximate local magnetic moment $\vec{F}_i^2$ for each lattice site i. For $n_i = 1$, the three single-site Fock states $|n_{i+}, n_{i0}, n_{i-}\rangle = |1,0,0\rangle$, $|0,1,0\rangle$, $|0,0,1\rangle$ have the same spin interaction energy because they all share the same magnetic moment $\vec{F}_i^2 = 2$. Since the states $|1,0,0\rangle$,$|0,0,1\rangle$ have $F_{z,i}^2 = (n_{i+} - n_{i-})^2 = 1$, whereas the state $|0,1,0\rangle$ has $F_{z,i}^2 = 0$, the thermodynamic average of this quantity in the Mott limit is $\langle F_z^2 \rangle = 2/3$.

In figure 3.7, the equal-time Green's functions $G_0(R)$,$G_\pm(R)$ in the canonical ensemble for $\rho = 1$ and $\rho = 2$ are shown for the antiferromagnetic case of $U_2 = 0.1U_0 > 0$, where R is the 1-norm distance. As in the ferromagnetic case, we see exponential decay in the Mott insulating phases and long-range order in the superfluid. However, the superfluid almost exclusively consists of $\sigma = 0$ particles, in contrast to the ferromagnetic case, where we observe almost only $\sigma = \pm 1$ particles.

Figure 3.8 shows the particle density distributions $P(\rho_0)$, $P(\rho_\pm)$ in the the antiferromagnetic case $U_2 = 0.1U_0$ for different phases in the canonical ensemble with $\rho = 1$ and $\rho = 2$. For $\rho = 1$, the on-site Fock states $|n_{i+}, n_{i0}, n_{i-}\rangle = |1,0,0\rangle$, $|0,1,0\rangle$,$|0,0,1\rangle$ have the same spin interaction energy. Hence the spin $\sigma = \pm 1$ and $\sigma = 0$ distributions are similar in the $\rho = 1$ Mott phase 3.8a, similar to the ferromagnetic case in figure

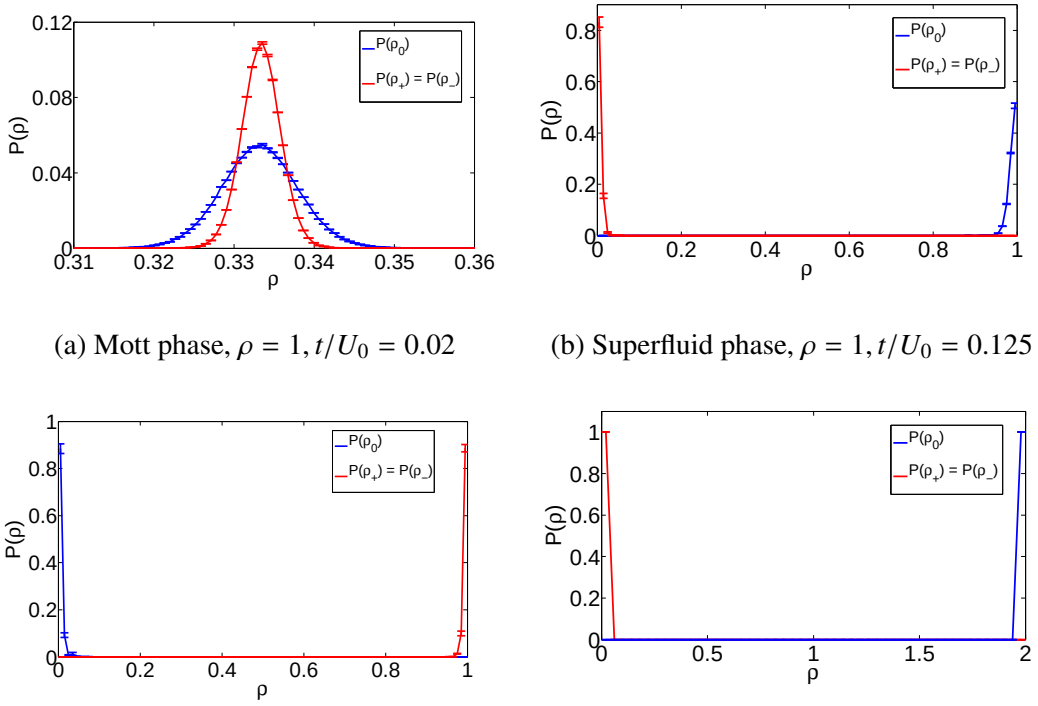

(a) Mott phase, $\rho = 1, t/U_0 = 0.02$

(b) Superfluid phase, $\rho = 1, t/U_0 = 0.125$

(c) Mott phase, $\rho = 2, t/U_0 = 0.02$

(d) Superfluid phase, $\rho = 2, t/U_0 = 0.125$

Figure 3.8: Density distributions of different spin species for Mott insulating and superfluid phases in the antiferromagnetic regime $U_2 = 0.1U_0$ in the canonical ensemble, with $\beta = 5, L = 10$ for all diagrams. See text for explanations.

3.3a.

In the $\rho = 1$ superfluid phase 3.8b, we effectively observe only $\sigma = 0$ particles. As explained above, states with one single spin species are favoured in superfluid phases. Double occupancies are frequent, and among the on-site Fock states with a single kind of spin particles, the state $|0, 2, 0\rangle$ has lowest spin energy. Hence we almost only observe $\sigma = 0$ particles.

For the $\rho = 2$ superfluid case 3.8d, the same explanation holds. As energy differences between different on-site spin states generally increase with increasing particle density, the distributions are even sharper.

In the $\rho = 2$ Mott phase 3.8c, there are almost exclusively $\sigma = \pm 1$ particles. This is simply due to the fact that the energetically cheapest on-site Fock state is $|n_{i+}, n_{i0}, n_{i-}\rangle = |1, 0, 1\rangle$, and particle hoppings and hence double occupancies are rare. However, we will see in the next section that for weak spin interactions U_2, a phase transition happens from the $|1, 0, 1\rangle$ to the $|0, 2, 0\rangle$ state inside of the second Mott lobe. In that case, the density probability distributions $P(\rho_0), P(\rho_\pm)$ would resemble

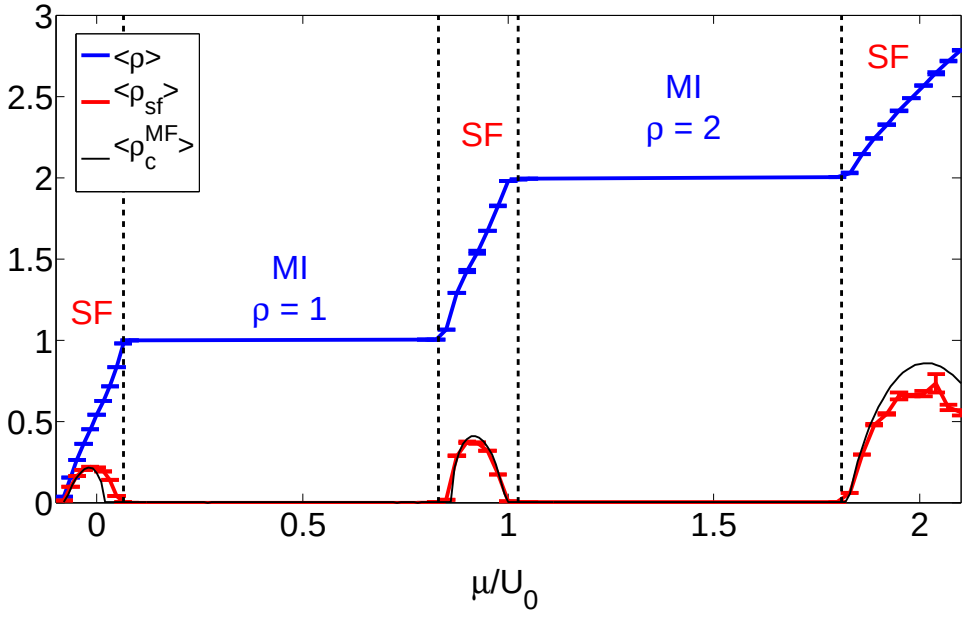

Figure 3.9: Total particle density $\langle\rho\rangle$ and superfluid density $\langle\rho_{sf}\rangle$ as a function of the chemical potential μ/U_0 for $t/U_0 = 0.02, L = 10, \beta = 5$. We can again observe Mott insulating phases with integer particle density $\langle\rho\rangle$, vanishing compressibility $\kappa = \frac{\partial\rho}{\partial\mu} = 0$ and zero superfluid density $\langle\rho_{sf}\rangle = 0$. All transitions are of second order, as predicted by mean-field methods. The fine black line indicates the mean-field condensate density $\langle\rho_c^{MF}\rangle$.

the ones of the $\rho = 2$ superfluid phase, figure 3.8d.

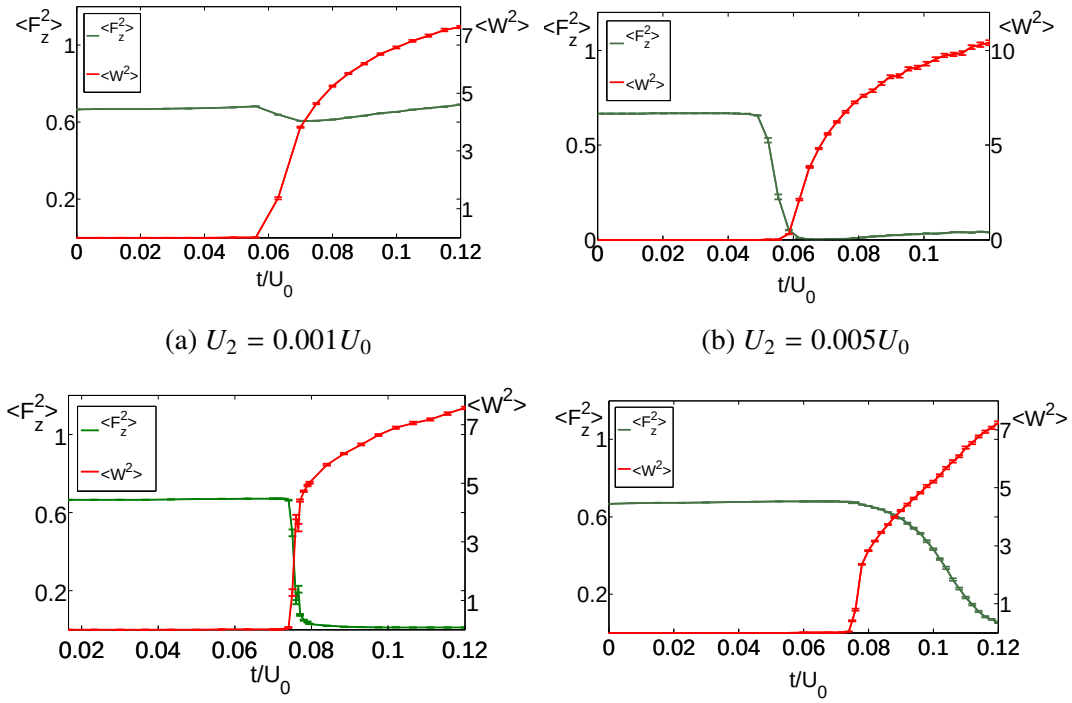

(a) $U_2 = 0.001U_0$ (b) $U_2 = 0.005U_0$

(c) $U_2 = 0.1U_0$ (d) $U_2 = 0.3U_0$

Figure 3.10: Phase transitions crossing the tip of the first Mott lobe in the canonical ensemble for different antiferromagnetic spin interaction strengths $U_2 > 0$. Shown is the average z-component of the local magnetic moment squared $\langle \hat{F}_z^2 \rangle$ and the winding number squared $\langle w^2 \rangle$ as the order parameter for the Mott to superfluid transition, both plotted versus $\frac{t}{U_0}$. System parameters where $L = 10, \beta = 5, \rho = 1$.

3.2.1 Phase transitions

In the antiferromagnetic case, the generic Mott to superfluid transition is of second order for strong interactions U_0, as we can see in figure 3.9, where we plotted the total particle density $\langle \rho \rangle$ and the superfluid density $\langle \rho_{sf} \rangle$ versus the chemical potential μ/U_0. However, compared to the ferromagnetic case in figure 3.4, transitions appear much steeper. Indeed, first order transitions occur for $U_0 \lesssim 30$, since the two on-site spin states $|n_{i+}, n_{i0}, n_{i-}\rangle = |1,0,1\rangle, |0,2,0\rangle$ approximately have the same energy, because the kinetic energy in the $|0,2,0\rangle$ state is lower, as hoppings contribute to the thermodynamic weight as $\sim \langle \rho_\sigma \rangle$. We observed the metastability of both states, but where not able to resolve a clear first order boundary for generic transitions, because to this end, temperatures have to be very low to avoid admixture of the energetically higher metastable state. In turn, low temperatures mean high computational resources since the extended configuration space grows with β.

Let us focus next on canonical phase transitions. In image 3.10, we see the square

of the z-projection of the local magnetic moment $\langle \hat{F}_z^2 \rangle$ and the winding number $\langle w^2 \rangle$ plotted versus t/U_0 for different antiferromagnetic spin interaction strengths U_2. For the smallest spin interaction $U_2 = 0.001U_0$ shown in figure 3.10a, the insulator to superfluid transition with the order parameter winding number squared $\langle w^2 \rangle$ appears to be of second order, and no phase transition in spin state can be observed for the chosen temperature.

However, if we increase spin interactions to be $U_2 = 0.005U_0$, as shown in figure 3.10b, a phase transition occurs with order parameter $\langle \hat{F}_z^2 \rangle$ directly before the Mott to superfluid transition. This corresponds to a transition from the degenerate single-site Fock states $|n_{i+}, n_{i0}, n_{i-}\rangle = |1, 0, 0\rangle$,$|0, 1, 0\rangle$,$|0, 0, 1\rangle$, which we observe with equal probability in the Mott limit, to the on-site state $|0, 1, 0\rangle$. Once again, in the superfluid phase, states with only one spin component are preferred. Of such states, double occupancies have lowest spin energy if both particles have spin $\sigma = 0$, hence there has to be a spin transition between Mott and superfluid limits.

If we further increase the spin interaction to $U_2 = 0.1U_0$ as depicted in figure 3.10c, both the insulator to superfluid and the spin transition appear very steep and at the same critical calue of t/U_0. The strong spin interaction highly suppresses double occupancies in the Mott insulating phase. At some point, interactions are weak enough that double occupancies may happen, but almost exclusively of $|0, 2, 0\rangle$ type. Hence all of a sudden, we only observe $\sigma = 0$ particles and so $\langle \hat{F}_z^2 \rangle$ drops to zero. As we are then in a state with a single spin species, particle hoppings contribute with a higher weight and therefore happen more often, which is the reason for the transition from the insulating to the superfluid state. In some sense, these two effects enhance each other, which is why both transitions appear to happen at the same critical value.

For very strong spin interactions like $U_2 = 0.3U_0$ as shown in figure 3.10d, the most probable double occupancies are of $|n_{i+}, n_{i0}, n_{i-}\rangle = |1, 0, 1\rangle$ type, since this state has the lowest magnetic moment. That means that at the Mott to superfluid transition, the system not yet prefers a state with only a single kind of spin particles as above. However, as we further increase t/U_0, it becomes more and more favorable to have all particles in a single hyperfine state, which is $\sigma = 0$.

The sudden transition around the tip of the Mott lobe for $U_2 \approx 0.1U_0$ made the finite-size scaling computations of the zero temperature phase boundaries quite difficult. However, using relatively high temperatures of $\beta = 1 \ldots 5$ weakens the spin transitions and increases particle number fluctuations so that finite size scaling is still applicable.

Next, we consider the canonical phase transition crossing the tip of the second Mott lobe for various spin interaction strengths U_2. In figure 3.11, we see the approximated

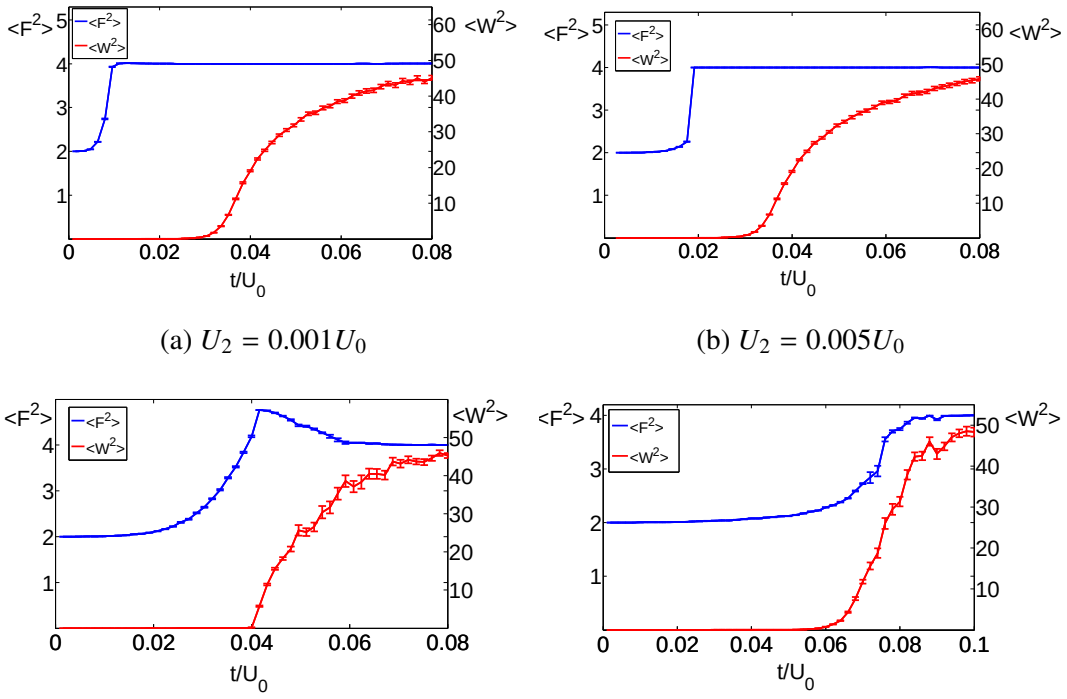

(a) $U_2 = 0.001U_0$ (b) $U_2 = 0.005U_0$

(c) $U_2 = 0.1U_0$ (d) $U_2 = 0.3U_0$

Figure 3.11: Phase transitions crossing the peak of the $\rho = 2$ Mott lobe in the canonical ensemble for different antiferromagnetic spin interactions $U_2 > 0$. The blue line shows the average local magnetic moment $\langle \vec{\hat{F}}^2 \rangle$, whereas the red line indicates the superfluid to Mott insulator transition order parameter winding number squared $\langle w^2 \rangle$, both as a function of $\frac{t}{U_0}$. System sizes where $L = 8, \beta = 16, \rho = 2$ in all four cases.

local magnetic moment $\langle \vec{\hat{F}}^2 \rangle = \frac{1}{L^2} \sum_i \langle \vec{\hat{F}}_i^2 \rangle$ and the average winding number squared $\langle w^2 \rangle$ as a function of t/U_0 in the canonical case $\rho = 2$. For $n_i = 2$, the state with the lowest spin energy on site i is given by $|n_{i+}, n_{i0}, n_{i-}\rangle = |1, 0, 1\rangle$ with the local magnetic moment $\langle \vec{\hat{F}}_i^2 \rangle = 2$, which is what we obtain for each antiferromagnetic spin interaction $U_2 > 0$ in the limit of zero temperature and strong interactions, $t/U_0 \to 0$.

However, if spin interactions are very small, as shown in figure 3.11a for the case $U_2 = 0.001U_0$, the system undergoes a phase transition from the $|1, 0, 1\rangle$ to the $|0, 2, 0\rangle$ state already deep in the insulating phase, since states with one single spin species are preferred because of particle hoppings, as explained above. Due to this transition, the local magnetic moment jumps discontinuously from $\langle \vec{\hat{F}}^2 \rangle = 2$ to $\langle \vec{\hat{F}}^2 \rangle = 4$, see figures 3.11a and 3.11b. It is a remarkable fact that this transition happens at a considerably different critical point in comparison to the Mott to superfluid transition for small spin interactions.

As expected, with increasing spin interaction strength U_2, the spin transition is

shifted towards stronger relative hopping t/U_0, since the difference in spin interaction energy between $|1,0,1\rangle$ and $|0,2,0\rangle$ is increased with increasing U_2. As can be seen in figure 3.11c for the case $U_2 = 0.1U_0$, the spin transition at some point happens around the same critical point as the insulator to superfluid transition. As the spin transition itself is notably smoothed out, the MI-SF transition remains of second order. However, it can be observed in figures 3.11c and 3.11d that stronger spin interactions considerably enlarge the second Mott lobe to higher values of t/U_0, due to the low pairing energy of $|1,0,1\rangle$ states.

The smoothing of the $\langle\vec{\hat{F}}^2\rangle$ transition may however be an effect of finite temperature, since in the critical regions of figures 3.11c and 3.11d, we observe phase coexistence of $|1,0,1\rangle$ and $|0,2,0\rangle$ states. This is a strong indication of an underlying first order transition, where both spin states are metastable and mixed up by finite β.

In turn, the metastability of $|1,0,1\rangle$ and $|0,2,0\rangle$ spin states up to the Mott to superfluid transition leads to the overshooting of $\langle\vec{\hat{F}}^2\rangle$, clearly visible at the critical point in figure 3.11c. Particle hoppings are frequent, which leads to higher occupancies, mainly of $|n_{i+}, n_{i0}, n_{i-}\rangle = |1,2,0\rangle$, $|0,2,1\rangle$ type, where $\langle\vec{\hat{F}}_i^2\rangle = 10$, hence the mean value $\langle\vec{\hat{F}}^2\rangle$ increases. In the limit of strong t/U_0, the system almost exclusively contains $\sigma = 0$ particles. Higher occupancies are thus always of $|0,3,0\rangle$ type, where $\langle\vec{\hat{F}}_i^2\rangle = 6$. At fixed density $\rho = 2$, such a triple occupancy always comes in pair with a single occupancy $|0,1,0\rangle$, where $\langle\vec{\hat{F}}_i^2\rangle = 2$. Hence in the superfluid limit, $\langle\vec{\hat{F}}^2\rangle = 4$ for all antiferromagnetic interactions $U_2 > 0$ in the low temperature limit.

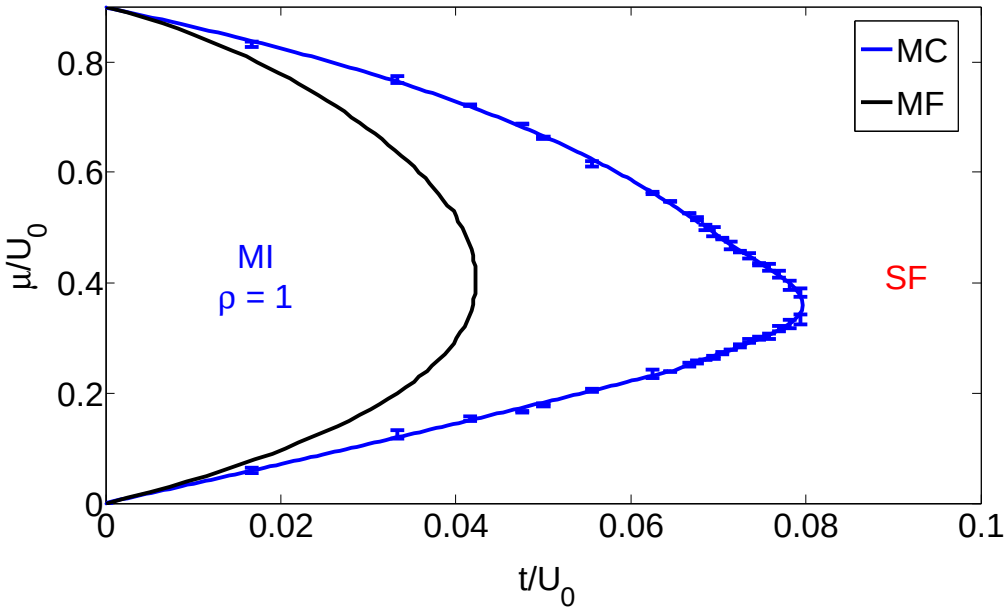

Figure 3.12: Ground state phase boundaries of the first Mott lobe for antiferromagnetic interactions $U_2 = 0.1U_0$. The blue line indicates the phase boundaries obtained by finite size scaling, whereas the black line represents the mean-field solution obtained in section 2.3.2.2. At the tip of the lobe, a first order transition from $\langle \hat{F}_z^2 \rangle = 2/3$ to $\langle \hat{F}_z^2 \rangle = 0$ occurs. For strong interactions, transitions are second order.

3.2.2 Phase diagram

Since we obtain the ground state phase diagram by a finite size scaling analysis 2.2.3 which is computationally very costly, we confine ourselves to the calculation of the first Mott lobe only. The result is depicted in figure 3.12, where the blue line indicates the phase boundary obtained by Monte Carlo. The black line shows the mean-field phase boundary obtained in section 2.3.2.2. Unsurprisingly, the two solutions match best for small hopping $t/U_0 \to 0$, where mean-field theory is exact.

For strong interactions, transitions are of second order, as can also be seen in figure 3.9. Around the tip of the lobe, transitions appear first order and a sharp transition from $\langle \hat{F}_z^2 \rangle = 2/3$ to $\langle \hat{F}_z^2 \rangle = 0$ occurs for low enough temperatures. However, if we take temperatures of about $\beta \approx 1$, the spin transitions are smoothed out and finite-size scaling remains possible.

CHAPTER 4

CONCLUSION AND OUTLOOK

4.1 Conclusion

In this work, we investigated the Bose-Hubbard model for atoms with total angular momentum $F = 1$ and unfixed magnetic quantum number $\sigma = m_F = -1 \ldots 1$. We gave a theoretical background on optical lattices and the emergence of the Bose-Hubbard Hamiltonian thereout, as well as on phase transitions and the method of finite-size scaling for transitions of second order.

A mean-field solution was performed for both the full spin-1 Bose-Hubbard model and what we call the *trilayer model*, which is given by the same Hamiltonian, except for the off-diagonal spin-flip terms. We computed the mean-field phase diagrams for both systems in ferromagnetic and antiferromagnetic regimes. Magnetic properties were examined for the full spin-1 system and previously obtained results (e.g. of [36, 37]) have been confirmed.

We gave a self-contained summary of the worm algorithm for the Bose-Hubbard model, and introduced the *layerswap* and *cutandpaste* update schemes, which were necessary to preserve ergodicity in the Monte-Carlo simulation of the trilayer system.

Our Monte-Carlo results include the one-particle Green's functions for Mott and superfluid phases and density distributions of all spin species. Phase transitions where investigated for finite-size systems both in the canonical and grand-canonical ensemble. Using finite-size scaling techniques, we obtained the first Mott lobe of the ground-state phase diagram for ferromagnetic and antiferromagnetic interactions.

During our Monte-Carlo studies, it became apparent that the conventional worm algorithm as it is used for the Bose-Hubbard model with scalar bosons is not capable

to sample the configuration space of the trilayer system in an ergodic way. The reason for this needs to be further investigated, but it seems that configurations that are close in energy should be connected by direct Monte-Carlo updates. Potentially, this might imply that the worm algorithm may generally be faced to similar problems in systems with first order boundaries, where the distinct metastable states are equal in energy, but may eventually be well separated in configuration space. If there is no direct update between these states and the probabilities of connecting Markov chains are small (i.e. essential intermediate states are improbable), the simulation will get stuck in one of the metastable states, dependent on the initial state and the sequence of random numbers used.

In order to bypass this problem for the trilayer system, we were forced to introduce the two new updates *layerswap* and *cutandpaste*, of which only the latter is able to fully restore ergodicity. Since these two updates are nonlocal, they are computationally very costly. Moreover, acceptance ratios of the *cutandpaste* update tend to be very low in superfluid phases, so our simulations were constrained to only small system sizes.

However, our Monte-Carlo studies show that spin transitions do not necessarily have to coincide with the Mott to superfluid transition in the trilayer model, as was already observed for the full spin-1 system in [22]. As the difference of critical values of both transitions is more pronounced in the trilayer system, it may help to get a clear understanding of the singlet to nematic transition in the full spin-1 Bose-Hubbard model, where a similar separation occurs.

4.2 Outlook: Worm algorithm with multiple worms

As we have seen, the negligance of the spin flip terms $\hat{b}^\dagger_{i+}\hat{b}^\dagger_{i-}\hat{b}_{i0}\hat{b}_{i0}$, $\hat{b}^\dagger_{i0}\hat{b}^\dagger_{i0}\hat{b}_{i+}\hat{b}_{i-}$ in the Hamiltonian (2.28) leads to large phenomenological differences between the full spin-1 Bose-Hubbard model (2.25) and the system that we have called the trilayer model. Since an experimental equivalence to this model does not exist, a further investigation does not seem to be very attractive. Only the layerswap update developed in section 2.4.5.3 might poteltially be useful for a worm algorithm [11, 12] simulation of the full spin-1 Bose-Hubbard model, since it can solve ergodicity problems occuring due to the $\mathbb{Z}_2$ of spin states in ferromagnetic phases.

In order to include the spin flip terms $\hat{b}^\dagger_{i+}\hat{b}^\dagger_{i-}\hat{b}_{i0}\hat{b}_{i0}$, $\hat{b}^\dagger_{i0}\hat{b}^\dagger_{i0}\hat{b}_{i+}\hat{b}_{i-}$ into the worm algorithmic Monte-Carlo simulation, it is indispensable to introduce a second worm propagating in the now further enlarged extended configuration space. The corresponding four-point Green's function of a configuration with two open worms A and

B in the system is then written as

$$\begin{aligned} &G\left(i_A\sigma_A, j_A\sigma'_A, \tau_A, \tau_{0,A}, i_B\sigma_B, j_B\sigma'_B, \tau_B, \tau_{0,B}\right) \\ &= \left\langle \hat{\mathcal{T}}_\tau \hat{b}_{i_A\sigma_A}\left(\tau_{0,A}\right) \hat{b}^\dagger_{j_A\sigma'_A}\left(\tau_A\right) \hat{b}_{i_B\sigma_B}\left(\tau_{0,B}\right) \hat{b}^\dagger_{j_B\sigma'_B}\left(\tau_B\right) \right\rangle \\ &= \mathrm{Tr}\left[\hat{\mathcal{T}}_\tau \hat{b}_{i_A\sigma_A}\left(\tau_{0,A}\right) \hat{b}^\dagger_{j_A\sigma'_A}\left(\tau_A\right) \hat{b}_{i_B\sigma_B}\left(\tau_{0,B}\right) \hat{b}^\dagger_{j_B\sigma'_B}\left(\tau_B\right) e^{-\beta\hat{H}} \right], \end{aligned} \tag{4.1}$$

and, in complete analogy to section 2.4.5, we define the extended partition function as the sum over all possible Green functions,

$$Z_e = \sum_{n=0}^{\infty} \sum_{|i_1\rangle,\ldots,|i_n\rangle} \sum_{(i\sigma)_A,(j\sigma)_A} \sum_{(i\sigma)_B,(j\sigma)_B} \int_0^\beta \mathrm{d}\tau_n \ldots \int_0^{\tau_2} \mathrm{d}\tau_1 W, \tag{4.2}$$

where the configuration weights W now have the form

$$\begin{aligned} W = &\langle i_1| \hat{H}_1 |i_2\rangle \cdot e^{-(\tau_2-\tau_1)E_{i_2}} \cdot \langle i_2| \hat{H}_1 |i_3\rangle \cdot e^{-(\tau_3-\tau_2)E_{i_3}} \cdot \\ &\ldots \cdot e^{-(\tau_k-\tau_{k-1})E_{i_k}} \langle i_k| \hat{b}^\dagger_{i_A\sigma_A} |i_{k+1}\rangle \cdot \ldots \cdot e^{-(\tau_l-\tau_{l-1})E_{i_l}} \langle i_l| \hat{b}_{j_A\sigma'_A} |i_{l+1}\rangle \cdot \\ &\ldots \cdot e^{-(\tau_m-\tau_{m-1})E_{i_m}} \langle i_m| \hat{b}^\dagger_{i_B\sigma_B} |i_{m+1}\rangle \cdot \ldots \cdot e^{-(\tau_p-\tau_{p-1})E_{i_p}} \left\langle i_p\right| \hat{b}_{j_B\sigma'_B} \left|i_{p+1}\right\rangle \cdot \\ &\ldots \cdot e^{-(\tau_n-\tau_{n-1})E_n} \langle i_n| \hat{H}_1 |i_1\rangle e^{-(\beta-\tau_n+\tau_1)E_{i_1}}. \end{aligned} \tag{4.3}$$

We recall that all interaction matrix elements as well as all worm operators have to be ordered in imaginary time. Again, we are free to move all four worm ends through configuration space, respecting detailed balance in each Monte-Carlo step. A particularly efficient choice of which worm ends are set to stay at rest and which ones are mobile has not been figured out yet.

Collecting again all diagonal terms in $\hat{H}_0$ leads to the same diagonal energies E_{i_k} we already had in the trilayer system. However, the sum of all off-diagonal terms we put into $\hat{H}_1$ is now extended to be

$$\hat{H}_1 = -\sum_{\langle i,j\rangle,\sigma} \left(\hat{b}^\dagger_{i,\sigma}\hat{b}_{j,\sigma} + \hat{b}^\dagger_{j,\sigma}\hat{b}_{i,\sigma} \right) + U_2 \sum_i \left(\hat{b}^\dagger_{i+}\hat{b}^\dagger_{i-}\hat{b}_{i0}\hat{b}_{i0} + \hat{b}^\dagger_{i0}\hat{b}^\dagger_{i0}\hat{b}_{i+}\hat{b}_{i-} \right). \tag{4.4}$$

Hence, in the partition function Z given in equation (2.169), there now appear matrix elements of $\hat{H}_1$ that correspond to spin-flip processes. It is precisely the sampling of these spin-flip matrix elements that is the reason why we need to have two worms simultaneously propagating through the extended configuration space.

Assuming that we have chosen the two worm ends $\hat{b}_{i_A\sigma_A}$, $\hat{b}_{i_B\sigma_B}$ as the two mobile ends of the worms, we now work out the update weight of the insertion of a spin flip as shown in figure 4.1.

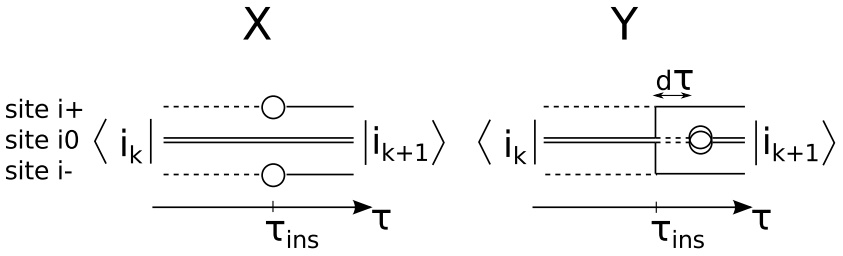

Figure 4.1: Graphical illustration of a spin flip process. The two worm heads $\hat{b}_{i_A\sigma_A}$, $\hat{b}_{i_B\sigma_B}$ have to meet at the same site $i_A = i_B$ at the same time $\tau_A = \tau_B = \tau_{\text{ins}}$. The spins have to be either both zero, $\sigma_A = \sigma_B = 0$, or, as depicted in the figure, $\sigma_A = +, \sigma_B = -$. Then, a spin flip can be inserted so that the worm head spin indices change like $(\sigma_A = +, \sigma_B = -) \leftrightarrow (\sigma_A = 0, \sigma_B = 0)$. The infinitesimal time step $d\tau$ is only included to fix the time ordering between the worm heads and the spin flip.

To insert a spin flip like $\hat{b}^\dagger_{i0}\hat{b}^\dagger_{i0}\hat{b}_{i+}\hat{b}_{i-}$, it is necessary that the two worm heads $\hat{b}_{i_A\sigma_A}$, $\hat{b}_{i_B\sigma_B}$ meet at the same site $i_A = i_B = i$ to the same time $\tau_A = \tau_B = \tau_{\text{ins}}$, and the two spins have to have the values $\sigma_A = +, \sigma_B = -$ or vice versa. The relevant factors of the corresponding weights of the configurations $W(X)$ and $W(Y)$ before and after the spin flip process depicted in figure 4.1 are given by

$$\begin{aligned} W(X) &= e^{-\tau_{\text{ins}}E_{i_k}} \left\langle i_k \left| \hat{b}_{i+}\hat{b}_{i-} \right| i_{k+1} \right\rangle e^{\tau_{\text{ins}}E_{i_{k+1}}}, \\ W(Y) &= e^{-\tau_{\text{ins}}E_{i_k}} \left\langle i_k \left| \hat{b}^\dagger_{i0}\hat{b}^\dagger_{i0}\hat{b}_{i+}\hat{b}_{i-} \right| \tilde{i}_k \right\rangle e^{\tau_{\text{ins}}E_{\tilde{i}_k} - (\tau_{\text{ins}}+d\tau)E_{\tilde{i}_k}} \left\langle \tilde{i}_k \left| \hat{b}_{i0}\hat{b}_{i0} \right| i_{k+1} \right\rangle e^{(\tau_{\text{ins}}+d\tau)E_{i_{k+1}}}. \end{aligned} \tag{4.5}$$

As we only included the infinitesimal time step $d\tau$ to fix the time ordering between worm heads and the spin flip, we can safely set it to zero so that the acceptance probability becomes

$$\begin{aligned} p_{X\to Y} &= min\left(1, \frac{W(Y)}{W(X)}\frac{A_{Y\to X}}{A_{X\to Y}}\right) \\ &= min\left(1, \frac{\left\langle i_k \left| \hat{b}^\dagger_{i0}\hat{b}^\dagger_{i0}\hat{b}_{i+}\hat{b}_{i-} \right| \tilde{i}_k \right\rangle \left\langle \tilde{i}_k \left| \hat{b}_{i0}\hat{b}_{i0} \right| i_{k+1} \right\rangle}{\left\langle i_k \left| \hat{b}_{i+}\hat{b}_{i-} \right| i_{k+1} \right\rangle} \frac{A_{Y\to X}}{A_{X\to Y}}\right), \end{aligned} \tag{4.6}$$

where $A_{X\to Y}$ denotes the proposal probability to go from configuration X to configuration Y. Calling n_{i0} the occupation number of spin $\sigma = 0$ particles on site i in the

state $|i_k\rangle$, this may be rewritten as

$$p_{X\to Y} = min\left(1, n_{i0}(n_{i0}-1)\frac{A_{Y\to X}}{A_{X\to Y}}\right). \tag{4.7}$$

As each spin flip is unique (there is always only a single possibility of how to flip), $A_{X\to Y}, A_{Y\to X}$ are truly the probabilities with which we propose the insertion $p_{\text{insertflip}}$ or deletion $p_{\text{deleteflip}}$ of a spin flip, respectively.

BIBLIOGRAPHY

[1] M. H. Anderson, J. R. Ensher, M. R. Matthews, C. E. Wieman, and E. A. Cornell, "Observation of Bose-Einstein Condensation in a Dilute Atomic Vapor," *Science*, vol. 269, no. 5221, pp. 198–201, 1995. [Online]. Available: http://www.sciencemag.org/content/269/5221/198.abstract

[2] K. B. Davis, M. O. Mewes, M. R. Andrews, N. J. van Druten, D. S. Durfee, D. M. Kurn, and W. Ketterle, "Bose-Einstein Condensation in a Gas of Sodium Atoms," *Phys. Rev. Lett.*, vol. 75, pp. 3969–3973, Nov 1995. [Online]. Available: http://link.aps.org/doi/10.1103/PhysRevLett.75.3969

[3] B. P. Anderson and M. A. Kasevich, "Macroscopic quantum interference from atomic tunnel arrays," *Science*, vol. 282, no. 5394, pp. 1686–1689, 1998. [Online]. Available: http://www.sciencemag.org/content/282/5394/1686.abstract

[4] D. Jaksch, C. Bruder, J. I. Cirac, C. W. Gardiner, and P. Zoller, "Cold bosonic atoms in optical lattices," *Phys. Rev. Lett.*, vol. 81, pp. 3108–3111, Oct 1998. [Online]. Available: http://link.aps.org/doi/10.1103/PhysRevLett.81.3108

[5] S. Sachdev, *Quantum Phase Transitions*. Cambridge University Press, 2001. [Online]. Available: http://books.google.de/books?id=Ih_E05N5TZQC

[6] M. Greiner, O. Mandel, T. Esslinger, T. Hänsch, and I. Bloch, "Quantum phase transition from a superfluid to a Mott insulator in a gas of ultracold atoms," *Nature*, vol. 415, no. 6867, pp. 39–44, 2002. [Online]. Available: http://www.nature.com/nature/journal/v415/n6867/full/415039a.html#close

[7] C. Chin, R. Grimm, P. Julienne, and E. Tiesinga, "Feshbach resonances in ultracold gases," *Rev. Mod. Phys.*, vol. 82, pp. 1225–1286, Apr 2010. [Online]. Available: http://link.aps.org/doi/10.1103/RevModPhys.82.1225

[8] M. P. A. Fisher, P. B. Weichman, G. Grinstein, and D. S. Fisher, "Boson localization and the superfluid-insulator transition," *Phys. Rev. B*, vol. 40, pp. 546–570, Jul 1989. [Online]. Available: http://link.aps.org/doi/10.1103/PhysRevB.40.546

[9] D. M. Stamper-Kurn, M. R. Andrews, A. P. Chikkatur, S. Inouye, H.-J. Miesner, J. Stenger, and W. Ketterle, "Optical Confinement of a Bose-Einstein Condensate," *Phys. Rev. Lett.*, vol. 80, pp. 2027–2030, Mar 1998. [Online]. Available: http://link.aps.org/doi/10.1103/PhysRevLett.80.2027

[10] T.-L. Ho, "Spinor Bose Condensates in Optical Traps," *Phys. Rev. Lett.*, vol. 81, pp. 742–745, Jul 1998. [Online]. Available: http://link.aps.org/doi/10.1103/PhysRevLett.81.742

[11] N. Prokofev, B. Svistunov, and I. Tupitsyn, "Exact, complete, and universal continuous-time worldline Monte Carlo approach to the statistics of discrete quantum systems," *Journal of Experimental and Theoretical Physics*, vol. 87, no. 2, pp. 310–321, 1998. [Online]. Available: http://dx.doi.org/10.1134/1.558661

[12] N. Prokof'ev, B. Svistunov, and I. Tupitsyn, "Worm algorithm in quantum Monte Carlo simulations," *Physics Letters A*, vol. 238, no. 45, pp. 253 – 257, 1998. [Online]. Available: http://www.sciencedirect.com/science/article/pii/S0375960197009572

[13] C. Trefzger, C. Menotti, B. Capogrosso-Sansone, and M. Lewenstein, "Ultracold dipolar gases in optical lattices," *Journal of Physics B: Atomic, Molecular and Optical Physics*, vol. 44, no. 19, p. 193001, 2011. [Online]. Available: http://stacks.iop.org/0953-4075/44/i=19/a=193001

[14] J. D. Jackson, *Classical electrodynamics*. Wiley, 1999.

[15] I. Bloch, J. Dalibard, and W. Zwerger, "Many-body physics with ultracold gases," *Rev. Mod. Phys.*, vol. 80, pp. 885–964, Jul 2008. [Online]. Available: http://link.aps.org/doi/10.1103/RevModPhys.80.885

[16] L. Pollet, "Ultracold atoms in an optical lattice: a numerical approach," Ph.D. dissertation, Universiteit Gent, Faculteit Wetenschappen, 2005. [Online]. Available: http://inwpent5.ugent.be/papers/thesislode.pdf

[17] C. K. Law, H. Pu, and N. P. Bigelow, "Quantum Spins Mixing in Spinor Bose-Einstein Condensates," *Phys. Rev. Lett.*, vol. 81, pp. 5257–5261, Dec 1998. [Online]. Available: http://link.aps.org/doi/10.1103/PhysRevLett.81.5257

[18] T. Ohmi and K. Machida, "Bose-Einstein Condensation with Internal Degrees of Freedom in Alkali Atom Gases," *Journal of the Physical Society of Japan*, vol. 67, no. 6, pp. 1822–1825, 1998. [Online]. Available: http://dx.doi.org/10.1143/JPSJ.67.1822

[19] A. Imambekov, M. Lukin, and E. Demler, "Spin-exchange interactions of spin-one bosons in optical lattices: Singlet, nematic, and dimerized phases," *Phys. Rev. A*, vol. 68, p. 063602, Dec 2003. [Online]. Available: http://link.aps.org/doi/10.1103/PhysRevA.68.063602

[20] M. Greiner, "Ultracold quantum gases in three-dimensional optical lattice potentials," Ph.D. dissertation, Ludwig-Maximilians-Universität München, 2003. [Online]. Available: http://greiner.physics.harvard.edu/PDF%20Files/PhD_greiner.pdf

[21] E. Demler and F. Zhou, "Spinor bosonic atoms in optical lattices: Symmetry breaking and fractionalization," *Phys. Rev. Lett.*, vol. 88, p. 163001, Apr 2002. [Online]. Available: http://link.aps.org/doi/10.1103/PhysRevLett.88.163001

[22] L. de Forges de Parny, F. Hébert, V. G. Rousseau, and G. G. Batrouni, "Interacting spin-1 bosons in a two-dimensional optical lattice," *Phys. Rev. B*, vol. 88, p. 104509, Sep 2013. [Online]. Available: http://link.aps.org/doi/10.1103/PhysRevB.88.104509

[23] P. Ehrenfest, "Phasenumwandlungen im ueblichen und erweiterten Sinn, classifiziert nach den entsprechenden Singularitaeten des thermodynamischen Potentiales," *Leiden Comm. Suppl.*, vol. 75b, 1933. [Online]. Available: http://www.dwc.knaw.nl/DL/publications/PU00016385.pdf

[24] M. Vojta, "Quantum phase transitions," *Reports on Progress in Physics*, vol. 66, no. 12, p. 2069, 2003. [Online]. Available: http://stacks.iop.org/0034-4885/66/i=12/a=R01

[25] K. Binder, "Theory of first-order phase transitions," *Reports on Progress in Physics*, vol. 50, no. 7, p. 783, 1987. [Online]. Available: http://stacks.iop.org/0034-4885/50/i=7/a=001

[26] T. Vojta, "Quantum phase transitions in electronic systems," *Annalen der Physik*, vol. 9, no. 6, pp. 403–440, 2000. [Online]. Available: http://dx.doi.org/10.1002/1521-3889(200006)9:6⟨403::AID-ANDP403⟩3.0.CO;2-R

[27] H. E. Stanley, *Introduction to phase transitions and critical phenomena*. Oxford University Press, UK, [2011].

[28] C. Pethick and H. Smith, *Bose-Einstein condensation in dilute gases*, 2nd ed. Cambridge [u.a.]: Cambridge Univ. Press, 2008.

[29] A. L. Fetter, J. D. Walecka, and Physics, *Quantum Theory of Many-Particle Systems (Dover Books on Physics)*. Dover Publications, Jun. 2003. [Online]. Available: http://www.amazon.com/exec/obidos/redirect?tag=citeulike07-20&path=ASIN/0486428273

[30] M. E. Fisher, M. N. Barber, and D. Jasnow, "Helicity modulus, superfluidity, and scaling in isotropic systems," *Phys. Rev. A*, vol. 8, pp. 1111–1124, Aug 1973. [Online]. Available: http://link.aps.org/doi/10.1103/PhysRevA.8.1111

[31] N. V. Prokof'ev and B. V. Svistunov, "Two definitions of superfluid density," *Phys. Rev. B*, vol. 61, pp. 11 282–11 284, May 2000. [Online]. Available: http://link.aps.org/doi/10.1103/PhysRevB.61.11282

[32] D. Landau and K. Binder, *A Guide to Monte Carlo Simulations in Statistical Physics*. Cambridge University Press, 2005. [Online]. Available: http://books.google.de/books?id=HbxQxS7tHiYC

[33] E. L. Pollock and D. M. Ceperley, "Path-integral computation of superfluid densities," *Phys. Rev. B*, vol. 36, pp. 8343–8352, Dec 1987. [Online]. Available: http://link.aps.org/doi/10.1103/PhysRevB.36.8343

[34] K. Sheshadri, H. R. Krishnamurthy, R. Pandit, and T. V. Ramakrishnan, "Superfluid and Insulating Phases in an Interacting-Boson Model: Mean-Field Theory and the RPA," *EPL (Europhysics Letters)*, vol. 22, no. 4, p. 257, 1993. [Online]. Available: http://stacks.iop.org/0295-5075/22/i=4/a=004

[35] D. van Oosten, P. van der Straten, and H. T. C. Stoof, "Quantum phases in an optical lattice," *Phys. Rev. A*, vol. 63, p. 053601, Apr 2001. [Online]. Available: http://link.aps.org/doi/10.1103/PhysRevA.63.053601

[36] K. V. Krutitsky and R. Graham, "Spin-1 bosons with coupled ground states in optical lattices," *Phys. Rev. A*, vol. 70, p. 063610, Dec 2004. [Online]. Available: http://link.aps.org/doi/10.1103/PhysRevA.70.063610

[37] R. V. Pai, K. Sheshadri, and R. Pandit, "Phases and transitions in the spin-1 Bose-Hubbard model: Systematics of a mean-field theory," *Phys. Rev. B*, vol. 77, p. 014503, Jan 2008. [Online]. Available: http://link.aps.org/doi/10.1103/PhysRevB.77.014503

[38] J. A. Nelder and R. Mead, "A simplex method for function minimization," *The Computer Journal*, vol. 7, no. 4, pp. 308–313, 1965. [Online]. Available: http://comjnl.oxfordjournals.org/content/7/4/308.abstract

[39] K. Huang, *Statistical mechanics*. New York: Wiley, 1987.

[40] S. Tsuchiya, S. Kurihara, and T. Kimura, "Superfluid - Mott insulator transition of spin-1 bosons in an optical lattice," *Phys. Rev. A*, vol. 70, p. 043628, Oct 2004. [Online]. Available: http://link.aps.org/doi/10.1103/PhysRevA.70.043628

[41] M. Snoek and F. Zhou, "Microscopic wave functions of spin-singlet and nematic Mott states of spin-one bosons in high-dimensional bipartite lattices," *Phys. Rev. B*, vol. 69, p. 094410, Mar 2004. [Online]. Available: http://link.aps.org/doi/10.1103/PhysRevB.69.094410

[42] H. Katsura and H. Tasaki, "Ground States of the Spin-1 Bose-Hubbard Model," *Phys. Rev. Lett.*, vol. 110, p. 130405, Mar 2013. [Online]. Available: http://link.aps.org/doi/10.1103/PhysRevLett.110.130405

[43] M. Łacki, S. Paganelli, V. Ahufinger, A. Sanpera, and J. Zakrzewski, "Disordered spinor Bose-Hubbard model," *Phys. Rev. A*, vol. 83, p. 013605, Jan 2011. [Online]. Available: http://link.aps.org/doi/10.1103/PhysRevA.83.013605

[44] C. Cohen-Tannoudji, B. Diu, and F. Laloë, *Quantum mechanics*, ser. Quantum Mechanics. Wiley, 1977. [Online]. Available: http://books.google.de/books?id=rr0PAQAAMAAJ

[45] T. Kimura, S. Tsuchiya, and S. Kurihara, "Possibility of a First-Order Superfluid Mott-Insulator Transition of Spinor Bosons in an Optical Lattice," *Phys. Rev. Lett.*, vol. 94, p. 110403, Mar 2005. [Online]. Available: http://link.aps.org/doi/10.1103/PhysRevLett.94.110403

[46] H. G. Katzgraber, "Introduction to Monte Carlo Methods," *ArXiv e-prints*, May 2009.

[47] W. Krauth, *Statistical Mechanics: Algorithms and Computations*, ser. Oxford Master Series in Physics. Oxford University Press, UK, 2006. [Online]. Available: http://books.google.fr/books?id=EnabPPmmS4sC

[48] L. Onsager, "Crystal Statistics. I. A Two-Dimensional Model with an Order-Disorder Transition," *Phys. Rev.*, vol. 65, pp. 117–149, Feb 1944. [Online]. Available: http://link.aps.org/doi/10.1103/PhysRev.65.117

[49] N. Metropolis, A. W. Rosenbluth, M. N. Rosenbluth, A. H. Teller, and E. Teller, "Equation of State Calculations by Fast Computing Machines," *The Journal of Chemical Physics*, vol. 21, no. 6, p. 10871092, 1953. [Online]. Available: http://scitation.aip.org/content/aip/journal/jcp/21/6/10.1063/1.1699114

[50] V. I. Manousiouthakis and M. W. Deem, "Strict detailed balance is unnecessary in Monte Carlo simulation," *The Journal of Chemical Physics*, vol. 110, no. 6, pp. 2753–2756, 1999. [Online]. Available: http://scitation.aip.org/content/aip/journal/jcp/110/6/10.1063/1.477973

[51] W. K. Hastings, "Monte Carlo sampling methods using Markov chains and their applications," *Biometrika*, vol. 57, no. 1, pp. 97–109, 1970. [Online]. Available: http://biomet.oxfordjournals.org/cgi/content/abstract/57/1/97

[52] R. H. Swendsen and J.-S. Wang, "Nonuniversal critical dynamics in Monte Carlo simulations," *Phys. Rev. Lett.*, vol. 58, pp. 86–88, Jan 1987. [Online]. Available: http://link.aps.org/doi/10.1103/PhysRevLett.58.86

[53] U. Wolff, "Collective Monte Carlo Updating for Spin Systems," *Phys. Rev. Lett.*, vol. 62, pp. 361–364, Jan 1989. [Online]. Available: http://link.aps.org/doi/10.1103/PhysRevLett.62.361

[54] L. Pollet, "Recent developments in quantum Monte Carlo simulations with applications for cold gases," *Reports on Progress in Physics*, vol. 75, no. 9, p. 094501, 2012. [Online]. Available: http://stacks.iop.org/0034-4885/75/i=9/a=094501

[55] L. Pollet, K. V. Houcke, and S. M. Rombouts, "Engineering local optimality in quantum Monte Carlo algorithms," *Journal of Computational Physics*, vol. 225, no. 2, pp. 2249 – 2266, 2007. [Online]. Available: http://www.sciencedirect.com/science/article/pii/S0021999107001295

[56] V. Ambegaokar and M. Troyer, "Estimating errors reliably in Monte Carlo simulations of the Ehrenfest model," *American Journal of Physics*, vol. 78, no. 2, pp. 150–157, 2010. [Online]. Available: http://scitation.aip.org/content/aapt/journal/ajp/78/2/10.1119/1.3247985

[57] N. Kawashima, J. E. Gubernatis, and H. G. Evertz, "Loop algorithms for quantum simulations of fermion models on lattices," *Phys. Rev. B*, vol. 50, pp. 136–149, Jul 1994. [Online]. Available: http://link.aps.org/doi/10.1103/PhysRevB.50.136

[58] K. Binder and E. Luijten, "Monte Carlo tests of renormalization-group predictions for critical phenomena in Ising models," *Physics Reports*, vol. 344, no. 46, pp. 179 – 253, 2001, renormalization group theory in the new millennium. [Online]. Available: http://www.sciencedirect.com/science/article/pii/S0370157300001277

[59] M. H. Quenouille, "NOTES ON BIAS IN ESTIMATION," *Biometrika*, vol. 43, no. 3-4, pp. 353–360, 1956. [Online]. Available: http://biomet.oxfordjournals.org/content/43/3-4/353.short

[60] B. Efron, "Bootstrap Methods: Another Look at the Jackknife," *Ann. Statist.*, vol. 7, no. 1, pp. 1–26, 01 1979. [Online]. Available: http://dx.doi.org/10.1214/aos/1176344552

[61] G. G. Batrouni, V. G. Rousseau, and R. T. Scalettar, "Magnetic and Superfluid Transitions in the One-Dimensional Spin-1 Boson Hubbard Model," *Phys. Rev. Lett.*, vol. 102, p. 140402, Apr 2009. [Online]. Available: http://link.aps.org/doi/10.1103/PhysRevLett.102.140402

Acknowledgments

First and foremost, I would like to thank Prof. Dr. Lode Pollet for the kind supervision of this thesis and for providing me with his miraculous code. You truly demonstrated patience!

In addition, I want to thank all the people who have embellished my life in the last months and years. These are in particular the long-standing university friends Stefan Sorg, Max Diefenbach and Stephan Pröller, as well as the not so long-standing friend Marius Fischer. Student days were so much more fun with you guys!

Of course, there are a lot more friends who were important to me in the last years. However, I'd like to keep this unpretentious here, so thanks to you all together :-)

Finally, my biggest thanks go to my parents for their unconditional support and love. I wouldn't have come so far without you!

EIGENSTÄNDIGKEITSERKLÄRUNG

Hiermit erkläre ich, die vorliegende Arbeit selbstständig verfasst zu haben und keine anderen als die in der Arbeit angegebenen Quellen und Hilfsmittel benutzt zu haben.

Constantin Grigo,

München, den 25. Oktober 2015